Reseach Group Biomedical Imaging Physics
Chair of Biomedical Physics
Department of Physics
School of Natural Sciences
Technical University of Munich

PhD Thesis

Setup Development for High-Resolution Quantitative Phase-Contrast Imaging at a Synchrotron Radiation Source

Mirko Philipp Riedel

January 2020 - September 2023

Supervisor: Prof. Dr. Julia Herzen

Advisor: Dr. Felix Beckmann

Helmholtz-Zentrum hereon

Technische Universität München
TUM School of Natural Sciences

Setup Development for High-Resolution Quantitative Phase-Contrast Imaging at a Synchrotron Radiation Source

Mirko Philipp Riedel

Vollständiger Abdruck der von der TUM School of Natural Sciences der Technischen Universität München zur Erlangung des akademischen Grades eines

Doktors der Naturwissenschaften (Dr. rer. nat.)

genehmigten Dissertation.

Vorsitz:	Prof. Dr. Martin Zacharias
Prüfer*innen der Dissertation:	1. Prof. Dr. Julia Herzen
	2. Prof. Dr. Martin Müller

Die Dissertation wurde am 27.09.2023 bei der Technischen Universität München eingereicht und durch die TUM School of Natural Sciences am 17.10.2023 angenommen.

Abstract

Phase-contrast X-ray imaging is widely used at synchrotron sources to improve contrast for low-attenuating samples. For retrieving the phase-shifting properties of a sample, multiple methods have been developed. The most commonly used method, propagation-based imaging, is easy to implement and able to provide fast measurements at high spatial resolution. However, as simplifying assumptions about the sample properties are necessary for the phase-retrieval, the obtained contrast is only of qualitative nature. These assumptions can be avoided if quantitative methods are used.

During the scope of this thesis, a new setup for quantitative phase-contrast imaging at the micro-tomography experiments at the beamlines P05 and P07, operated by the Helmholtz-Zentrum Hereon at PETRA III, DESY, was designed, characterized, and applied. The goal of the redesign was to replace the existing grating-based setup and improve the spatial resolution as well as reduce application complexity.

The design of the new setup combines phase-retrieval methods from Speckle-based imaging with novel 2D gratings as wavefront markers. The new gratings showed improved visibility at small length scales, compared to other wavefront markers used in previous works. The spatial resolution of the setup was determined to reach down to approx. 2 µm and is comparable to the resolution of propagation-based imaging at this experiment.

In order to allow for increased throughput, a post-processing chain was implemented for the DESY Maxwell cluster. The chain was designed in Python and includes corrections for wavefront marker position inaccuracies, the phase-retrieval using the Unified Modulated Pattern Analysis, corrections for phase ramps, and integration of the differential phase images to recover the full phase-shift. Due to the large amount of data generated for a measurement, the processing was optimized to some extent for computation performance.

The application of the setup for measuring samples was shown for both beamlines at energies up to 57 keV. The types of samples scanned in multiple beamtimes covered a broad range, from biomedical tissue samples to material science applications, where excellent contrast for light elements was achieved. During the scope of this work, the setup also transitioned from initial experiments to user application.

Kurzfassung

Röntgen Phasenkontrastbildgebung gehört an Synchrotron Strahlungsquellen zu den Standardmethoden um den Kontrast für schwach absorbierende Proben zu verbessern. Um den Phasenschub einer Probe zu rekonstuieren wurden im Laufe der Zeit eine Vielzahl an Methoden entwickelt. Die am häufigsten verwendete Methode ist die propagationsbasierte Bildgebung. Diese ist einfach zu implementieren, ermöglicht schnelle Messungen und liefert eine hohe räumliche Auflösung. Jedoch werden bei der Rekonstuktion der Phase vereinfachende Annahmen über die Eigenschaften der Probe getroffen, weshalb die Daten nur von qualitativer Natur sind. Durch die Verwendung von quantitativen Bildgebungsmethoden lassen sich diese Annahmen vermeiden.
Im Rahmen dieser Arbeit wurde ein neuer Messaufbau für quantitative Phasenkontrasbildgebung an den Mikrotomographie Experimente an den Beamlines P05 und P07 entwickelt. Die Beamlines werden durch das Helmholz-Zentrum Hereon an PETRA III, DESY betrieben. Der neue Aufbau wurde im Rahmen dieser Arbeit charakterisiert und angewendet. Durch die Neuentwicklung wurde ein vorheriger Aufbau ersetzt und dabei die räumliche Auflösung verbessert und die Anwendung vereinfacht.
Das Design des neuen Aufbaus kombiniert Phasenrekonstuktionsmethoden aus dem Bereich Speckle-based imaging mit neuen 2D Phasengittern als Wellenfront Marker. Diese neuen Gitter verbessern den Kontrast des Wellenfront Markers bei kleinen Perioden im Vergleich zu vorherigen Markern in der Literatur. Die räumliche Auflösung des Aufbaus erreicht bis zu 2 µm und ist damit vergleichbar zur propagationsbasierte Bildgebung an diesem Experiment. Um den Probendurchsatz am Experiment zu verbessern, wurde eine Auswertekette entwickelt und auf dem DESY Maxwell Computercluster in Python umgesezt. In dieser Kette enhalten ist eine Korrektur für Positionsungenauigkeiten des Wellenfornt Markers, die Phasenrekonstuktion welche die Unified Modulated Pattern Analysis nutzt, Korrekturen für Phasenrampen und die Phasenintegration der zweidimensionalen differentiellen Phasenbilder. Aufgrund der hohen Datenmenge für eine Messung, wurde die Auswertekette bis zu einem gewissen Grad auf Leistung optimiert.
Die Anwendung der Aufbaus wurde an beiden Beamlines für Strahlenergien bis zu 57 keV gezeigt. Dabei wurden in meheren Messzeiten eine Vielzahl an verschiedenen Probensystemen betrachtet, von biomedizinischen Proben hin zu materialwissenschaftlichen Proben. Im Rahmen dieser Arbeit wurde der Aufbau von einem anfänglichen internen Experiment in den Nutzerbetrieb überführt.

Publications and Scientific Presentations

Publications as First Author

A. Gustschin*, **M. Riedel***, K. Taphorn, C. Petrich, W. Gottwald, W. Noichl, M. Busse, S.E. Francis, F. Beckmann, J.U. Hammel, J. Moosmann, P. Thibault & J. Herzen. High-resolution and sensitivity bi-directional x-ray phase contrast imaging using 2D Talbot array illuminators. *Optica* **8**(12):10.1364/OPTICA.441004 (2021). *Shared first authorship

M. Riedel, K. Taphorn, A. Gustschin, M. Busse, J.U. Hammel, J. Moosmann, F. Beckmann, F. Fischer, P. Thibault & J. Herzen. Comparing x-ray phase-contrast imaging using a Talbot array illuminator to propagation-based imaging for non-homogeneous biomedical samples. *Scientific Reports* **13**(6996):10.1038/s41598-023-33788-7 (2023).

Publications as Co-Author

J. Scholz, C. Petrich, **M. Riedel**, L. Heck, L. Birnbacher, S. Gkoumas, T. Sellerer, K. Achterhold, & J. Herzen. Biomedical x-ray imaging with a GaAs photon-counting detector: A comparative study. *Applied Physics Letters Photonics* **5**(10):10.1063/5.0020262 (2020).

F. L. Schwarzenberg, P. Schuetz, J. U. Hammel, **M. Riedel**, J. Bartl, S. Bordbari, S.-C. Frank, B. Walken-fort, M. Busse, J. Herzen, C. Wuelfing, and S. Henne. Three-dimensional analyzes of vascular networkmorphology in a murine lymph node by x-ray phase-contrast tomography with a 2d talbot array. *Frontiers Immunology*:10.3389/fimmu.2022.947961 (2022).

Conference Proceedings

M. Riedel, A. Gustschin, L. Ushakov, Wolfgang Noichl, K. Taphorn, M. Busse, F. Beckmann, J.U. Hammel, J. Moosmann, P. Thibault, & J. Herzen. High-resolution quantitative

phase-contrast x-ray imaging for biomedical samples at PETRA III. *Proceedings of SPIE 11840, Developments in X-ray Tomography XIII* **118400W** (2021).

M. Riedel, J. U. Hammel, J. P. Moosmann, F. Beckmann, F. L. Schwarzenberg, P. Schuetz, S. Henne, C. Wülfing, M. Busse, & J. Herzen. Quantitative phase-contrast x-ray micro CT for visualization of mouse lymph nodes. *Proceedings of SPIE 12242, Developments in X-ray Tomography XIV* **1224213** (2022).

Conference Proceedings as Co-Author

F. Beckmann, F. Wilde, J. U. Hammel, J. P. Moosmann, I. Greving, L. Lottermoser, **M. Riedel**, M. Thiry. Brilliant light for materials science: industrial applications of synchrotron radiation based microtomography at the tomography instruments by GEMS at PETRA III. *Proceedings of SPIE 11840, Developments in X-ray Tomography XIII* **118400W** (2021).

Oral Presentations

High-resolution quantitative phase-contrast x-ray imaging for biomedical samples at PETRA III. *Online, SPIE Optics and Photonics 2021, San Diego, USA, August 2021.*

High-resolution quantitative phase-contrast X-ray tomography for biomedical samples. *Online, SRI 2021, Hamburg, Germany, March 2022.*

Quantitative phase-contrast x-ray micro CT for visualization of mouse lymph nodes. *SPIE Optics and Photonics 2022, San Diego, USA, August 2022.*

Quantitative phase-contrast micro computed tomography for biomedical samples. *CARAT-Workshop "Interdisciplinary Initiative for Pencil and Micro X-ray Beam Applications", Hamburg, Germany, September 2022.*

Contents

1 Introduction

1.1 Introduction

Consider a tissue biopsy sample. How do you know if there are malignant changes in it? The classic approach would be to perform a histologic examination. The process starts with fixing and embedding the tissue, most commonly into a block of paraffin. To look inside and visualize individual cells, the paraffin block is cut into thin slices and viewed with an optical light microscope. In addition to structural information, further information can be obtained by adding specific stains that highlight certain biological structures and provide information about tissue types.

Although this type of examination is performed every day in clinics, it has certain drawbacks. The process of cutting the sample and transferring it to a microscope slide can cause distortion and damage to the tissue [Pic+18]. The spatial resolution is high in two dimensions. However, it is limited along the section axis by the section thickness, which can be several micrometers. Due to time constraints, it is not common to examine all of the sections, but only a few exemplary ones. This means that important features may be overlooked, leading to something being misdiagnosed. To avoid this, the entire volume must be examined.

A suitable method must meet a number of criteria: It must be three-dimensional, have the same resolution level as conventional light microscopy, and provide good contrast for soft tissues. In addition, a short examination time and the ability to highlight specific structures are desired.

Combining the serial sections of classical 2D histology to a 3D volume is possible, but time consuming and often hindered by artifacts in the images. X-ray imaging and phase-contrast micro Computed Tomography (CT) on the other hand have been shown to meet several of the criteria for a suitable method quite well.

Conventional CT imaging uses the change in absorption behavior between different materials. While this is a simple and robust method and provides good contrast for highly

absorbing tissues, such as bone, the visualization of soft tissues is generally not good. By visualizing the phase-shifting properties of the sample, good x-ray contrast can be achieved for soft tissues [Fit00; Mom05]. The spatial resolution of today's micro CT experiments at synchrotron sources can reach down to a few micrometers [Wei+10], reaching the level of conventional histology. At the same time, third-generation synchrotron sources provide high brilliance, which promises fast scan times even at high spatial resolution.

In this work, the focus is on microtomography in the near-field regime. The reviews by Bravin et al. [BCS12] and Endrizzi [End18] discuss several of the existing methods that can be applied to measure and visualize the phase-shift. The techniques can be divided into two classes. Non-quantitative techniques, which make assumptions about the properties of the sample, are among the most commonly used. Because of the assumptions used, the resulting contrast is only qualitative. However, their popularity is due to their experimental simplicity and reliability. Propagation-Based Imaging (PBI), e.g. based on the transport of intensity equation [Sni+95] in combination with a homogeneous material assumption [Pag+02], offers a simple setup, high spatial resolution and robust results. Other common PBI methods assume a weakly absorbing object and use the contrast transfer function to determine the phase [Sal+09]. The disadvantage of having non-quantitative contrast in PBI can be overcome by using multiple measurements at multiple distances, so-called holotomography [Clo+99]. The strengths and capabilities of these methods have been demonstrated many times for micro- and nanotomography, e.g. for the visualization of lung morphology in Eckermann et al. [Eck+20]. Since obtaining structural information is often the primary goal of a measurement, the majority of scans are performed using PBI techniques.

A second class of techniques uses X-ray optical elements to achieve quantitative phase contrast. Unlike non-quantitative techniques, no assumptions are made about the sample. The techniques in this class of methods impose an intensity pattern on the illumination. A phase shift of a sample causes a lateral shift of this intensity pattern. The exact way in which these changes are recorded is different for each technique. Included in this class are grating interferometry techniques, Grating-Based Imaging (GBI) [Dav+02; Mom+03], edge-illumination and coded aperture techniques [Oli21] and more. Among the most recent additions to this class, Speckle-Based Imaging (SBI) techniques [BWS12; Bér+12b; MPS12] were introduced. As for PBI techniques, the performance of such quantitative methods has been demonstrated in various publications, such as Schulz et al. [Sch+10] or Zanette et al. [Zan+13b] showed for the example of GBI.

The exact choice of the most appropriate technique for a measurement depends on several factors. First, the scientific question about the sample may require a quantitative technique,

or it may be that qualitative, structural information is sufficient. Another trade-off that is usually required is between measurement time, sensitivity, and spatial resolution. PBI with a single material assumption offers fast measurements while using nearly the full native system resolution. At the same time, it has the disadvantage of non-quantitative contrast and comparatively low sensitivity [Zan+13a]. Most quantitative phase-contrast techniques may sacrifice spatial resolution and require elaborate setups and long measurement times, but usually show good sensitivity to even small changes in the sample. Finally, the number of methods available at a given setup is usually limited, since in most cases not all methods are implemented.
This leaves a gap that the work in this thesis tries to fill: a simple, quantitative phase-contrast setup that achieves a spatial resolution level of a few micrometers while maintaining good sensitivity and fast measurement time.

1.2 Setting

The results presented in this thesis focus on phase-contrast imaging at a synchrotron radiation source. The work was part of a collaboration between the Technical University of Munich and the Helmholtz-Zentrum Hereon. Using the micro CT setup at beamline P05, operated by the Helmholtz-Zentrum Hereon at PETRA III, DESY, as well as the computing and data handling infrastructure of DESY, a long-term proposal (LTP II-20190765) was established. Within this proposal a new setup for quantitative imaging was developed.
The goal was to replace the existing Grating-Based Imaging (GBI) setup. The old setup was limited in its spatial resolution to a level of about 5 µm. [Hip18] due to the gratings used. With the new setup, the goal was to bring the spatial resolution closer to the level of absorption imaging and Propagation-Based Imaging (PBI). Further simplification of the setup to allow easy installation and user operation was also aimed at.
After the initial successful development of the setup at P05, the development focused on further goals, on the one hand to increase the stability of the setup to the level of user operation, and on the other hand to adapt the setup for the use of higher beam energies at beamline P07. The former was addressed in a Block Allocation Group proposal (BAG-20211054), the latter in a regular proposal (I-20200511) and a long-term proposal (LTP II-20210022).

1.3 Outline

The structure of this thesis will be as follows: In chapter 2, the principles of X-ray imaging will be discussed. This will range from the properties of X-rays and how they are generated to the description of how they interact in a particle image and in a wave image. Detection is also briefly described, as are the principles of tomographic imaging. The chapter 3 describes the basics of phase contrast imaging and the phase retrieval methods used. A method for correcting drifts and improving phase-retrieved data, dynamic flat-field correction is described, and the spatial resolution of a scan is discussed.
The next chapter, 4, reports on the design of the setup constructed during this thesis. The basic setup at PETRA III is described, as well as the hardware extensions. The measurement process, from the scan protocol to the phase retrieval, is also outlined.
The measurements performed during this thesis are described in the chapter 5. First, the characterization of the relevant setup parameters is presented, followed by some exemplary studies on samples at both beamlines, P05 and P07.
Finally, the results and findings of this thesis are summarized in the chapter 6. There are also some prospects for possible future developments.

Principles of X-ray Imaging 2

The contents of this chapter are based on the books of Als-Nielsen and McMorrow [AM11], Willmott [Wil19], and Paganin [Pag+06]. This chapter will cover how X-rays are produced and what the key properties of the sources are, how X-rays interact with matter in an imaging setting, and how they are registered for imaging. The technique of tomographic imaging is described as well. As phase-contrast imaging is one of the key aspects of this work, it will be discussed in a separate chapter 3.

X-rays are electromagnetic radiation with an energy of 100 eV to about 500 keV or wavelengths from 10 nm to 2.5 pm, as can be seen in Fig. 2.0.1. As such, they are part of the electromagnetic spectrum, with frequencies higher than UV light and below gamma radiation. They were discovered in 1895 by Wilhelm Conrad Röntgen [Rön98] for which he was awarded the Nobel Prize in Physics in 1901 [ABa].

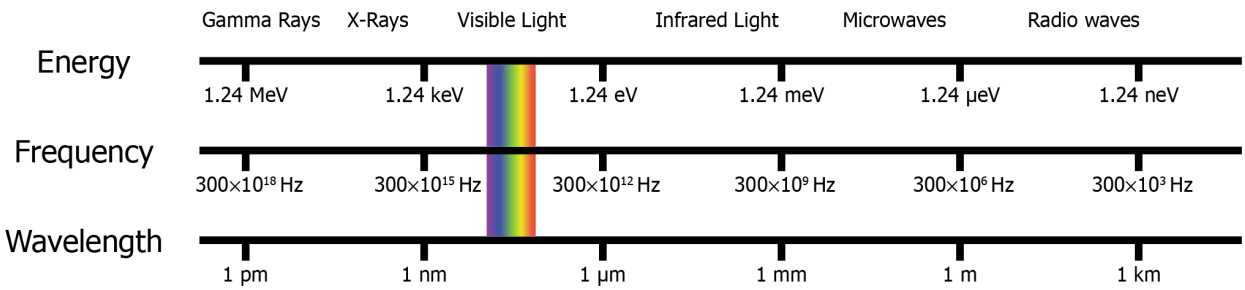

Figure 2.0.1: Position of X-ray radiation in the electromagnetic spectrum. The distances are not to scale. X-rays are high energetic radiation, with a wavelength shorter than visible and UV light.

2.1 Properties of X-ray Radiation and Sources

Since X-rays were discovered, more and more ways to produce them have been added. As each of the sources has different radiation properties, their use cases differ strongly, and it is necessary to design experiments accordingly. In the next sections, the different source types are briefly described, and some of the key properties and differences will be introduced and compared.

2.1.1 Laboratory and Medical Sources

In laboratory settings, tube sources are most dominant, with only a few exceptions of compact light sources. In a tube source, an electron beam is generated from a cathode and accelerated toward a target anode. Inside the target material, the electron beam is decelerated, emitting a continuous bremsstrahlung spectrum, with maximum photon energy corresponding to the maximum electron energy. In addition, so-called characteristic lines are emitted if bound electrons of the anode atoms are kicked out, and outer shell electrons fill the gaps.
Typical target materials include tungsten and molybdenum. Most developments in this type of source have concentrated on solving the heat problem, as only a few percentages of the electron beam energy are emitted as radiation. This is especially a problem if the electron beam size on the target is desired to be small. Water cooling, rotating anodes for better heat distribution, and even liquid metal anodes have improved the ability to reach a higher power.
Laboratory sources can typically achieve only comparably low brilliance and coherence at high power, as they have to do a trade-off between the extent of the source spot and the power of the electron beam. This is improved in liquid metal jet sources, but still, broad polychromatic spectra limit the ability to achieve high temporal coherence.

2.1.2 Synchrotron Sources

While tube sources are the backbone of medical imaging, many advanced imaging techniques have been developed at large-scale research facilities using synchrotron radiation. While at first, this radiation was an unwanted side effect of particle accelerators, today's synchrotron facilities are designed for utilizing it.

X-ray generation at a synchrotron source is based on the acceleration of charged particles in magnetic fields. The basic structure of a modern synchrotron facility starts with an accelerator structure, where the synchrotron accelerator is located. Particles, in most cases electrons, are accelerated by a cascade of accelerators up to several GeV and then stored in a storage ring, where an RF cavity only replenishes the energy lost by each turn. In order to produce X-rays, insertion devices are added to the storage ring.
Three different types of insertion devices have been developed for radiation generation. Their spectra and brilliance are compared in Fig. 2.1.1 **b)**. The oldest and most simple devices are bending magnets, as they are always needed for keeping the particle beam on a closed loop. The particle beam is deflected and a broad polychromatic spectrum with the lowest brilliance of all insertion devices is produced (cf. Fig. 2.1.1 **b)** black line). Further development led to so-called wigglers. They are an array of magnets with alternating field orientations, creating a sinusoidal path of the particle beam. Each curve acts like a bending magnet, and the total brilliance is summed up (cf. Fig. 2.1.1 **b)** green line). If the magnetic field strength and period are tuned to allow for coherent addition of the emission of each curve, the device is called an undulator. Its spectrum shows discrete peaks with high brilliance (cf. Fig. 2.1.1 **b)** blue line). By tuning the gap, the magnetic field strength can be changed, and the positions of the peaks are shifted.

Synchrotron light sources typically offer much higher brilliance than laboratory sources. High flux and small emittance are the contributing factors. A small beam divergence makes it possible to design experiments as beamlines. The beam from an insertion device is transferred to experimental endstations several tens of meters from the source. In-between, optics areas allow for filtration, collimation, or the use of monochromators.

2.1.3 Figures of Merit of X-ray Radiation

Although all the sources mentioned above produce X-rays, the emitted radiation of each source differs. It is helpful to introduce some figures of merit describing the radiation properties. For the scope of this work, two figures of merit are most relevant.

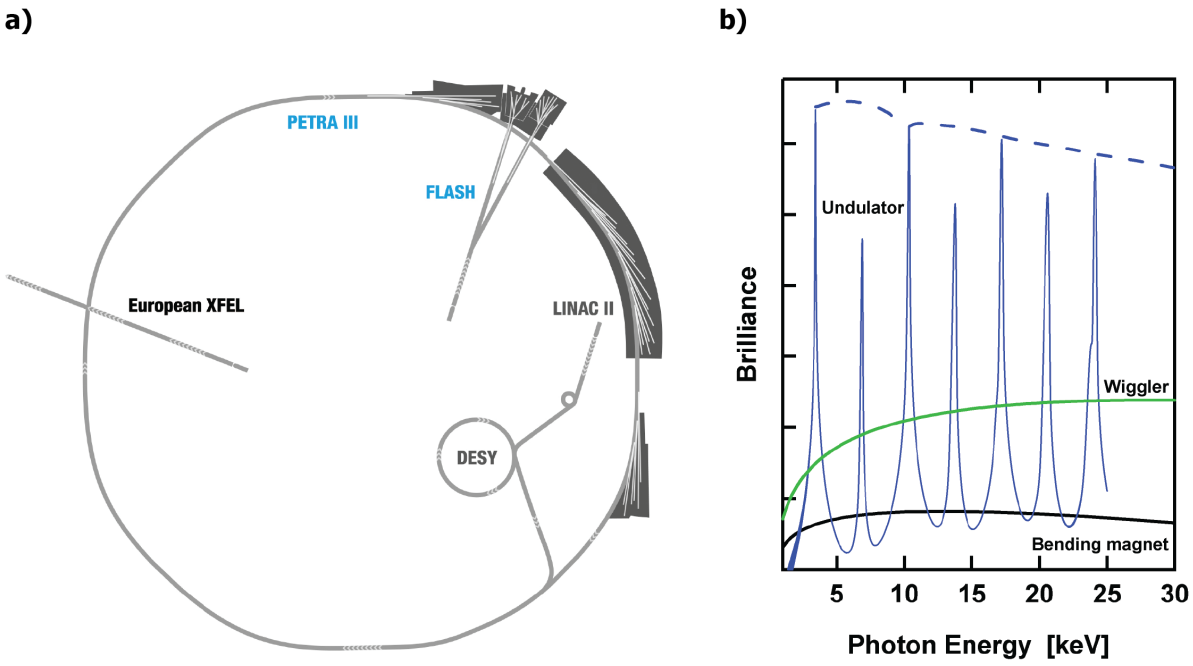

Figure 2.1.1: Layout of a synchrotron facility in **a)**. The DESY in Hamburg, Germany, operates the storage ring PETRA III. The actual synchrotron is DESY II in the middle. The beamlines are located in the three experimental halls on the right. In **b)** the brilliance of the different insertion devices are compared. A bending magnet (black line) has a continuous spectrum with the lowest brilliance. A wiggler (green lines) has a higher brilliance while still showing a continuous spectrum. An undulator (blue line) has sharp brilliant peaks at discrete energies, much higher than the other both two. Images from [DESc; DESa].

Brilliance

The brilliance of an X-ray source is used to compare the brightness of different sources under defined properties. It is defined as

$$\text{Brilliance} = \frac{\text{photons/second}}{(\text{mm}^2 \text{ source area})\,(\text{mrad})^2\,(0.1\%\text{ bandwidth})}. \tag{2.1.1}$$

The brilliance describes how the flux in a small bandwidth is distributed over space and angular range. Thus, it enables us to compare different sources better than only by looking at the total flux. High total flux, as well as small sources-spots and focused radiation, contribute to a high brilliance. The bandwidth, as well as the source geometry, also contribute to another figure of merit of an experiment, the coherence.

Coherence

While in theory, waves are often considered to be perfectly monochromatic waves from a point source, no realistic source will show such properties. The concept of coherence looks at the temporal and the spatial correlation of a wave field and, by introducing a coherence length, gives a scale after interference effects will no longer be observed. As phase-contrast imaging relies on waves interfering, it requires a high degree of coherence. One can differentiate between two aspects of coherence, longitudinal and transverse coherence.

Longitudinal Coherence The longitudinal coherence, also called temporal or spectral coherence, is related to the bandwidth of the radiation. The longitudinal coherence length is defined by

$$l_c^l = \frac{1}{2}\frac{\lambda^2}{\Delta\lambda}, \tag{2.1.2}$$

where λ is the wavelength of the radiation and $\Delta\lambda$ the bandwidth. The longitudinal coherence length gives a distance, after which two waves traveling in the same direction are out of phase.

As it is related to the bandwidth of a source, optical elements like monochromators are often used to increase this length. Also, larger wavelengths and, therefore, lower energies are favorable.

The principle of spectral coherence is illustrated in Fig. 2.1.2 **c)**. Two wavefronts with

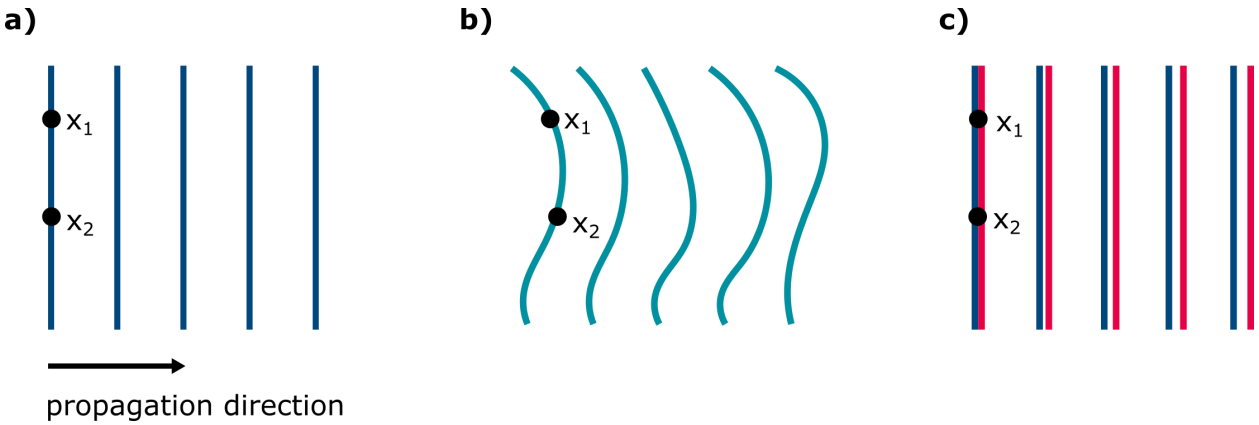

Figure 2.1.2: Illustration of both types of both types of coherence. A wavefront is propagating from left to right. In **a)** an perfectly even and perfectly monochromatic wavefront is shown. Both coherence lengths are infinite. In **b)** limited spatial coherence is illustrated. Interference between the points x_1 and x_2 is only observable for a limited distance. The spectral coherence length is still infinite. In **c)** the effect of limited spectral coherence is shown. With increasing distance, the wavefronts for different wavelengths drift apart, limiting their ability to interfere. The spatial coherence length is infinite.

different wavelengths are initially aligned. With increasing propagation distance, the wavefronts drift apart, limiting the distance after which interference between points x_1 and x_2 is observable.

Transverse Coherence Besides longitudinal coherence, transverse or spatial coherence is connected to the extent of the source spot. The transverse coherence length is given by

$$l_c^t = \frac{\lambda}{2}\frac{R}{D}, \tag{2.1.3}$$

where R is the distance from the source to the observation point, and D is the lateral extent of the source. It describes the effect of different propagation directions and gives the maximum spatial separation between two points where interference is still observable.
From Eq. 2.1.3, it can be seen that it is beneficial to have a small source size and to be far away from the source. Similar to longitudinal coherence length, smaller energies are an advantage for having a high transverse coherence.
The principle of spatial coherence is shown in Fig. 2.1.2 **b)**. Due to distortions of the uneven wavefront, the distance after which interference from the points x_1 and x_2 can be observed, is limited.

Coherence of Different Source Types Laboratory tube sources emit a polychromatic bremsstrahlung spectrum, which leads to a low longitudinal coherence, which only improves slightly if the characteristic lines are dominant. The transverse coherence is dependent on the size of the focal spot on the target. By using focusing electron optics, and unless liquid metal targets are used, limiting the power, small source spots and, therefore, high transverse coherence can be achieved. With the small source size and long distance from the source, the transverse coherence of synchrotron radiation is usually high. If a monochromator is used, also a high longitudinal coherence can be reached. This makes synchrotron radiation well suited for coherent imaging applications but also for near-field techniques such as GBI or SBI.

2.2 Interaction of X-rays with Matter

In an imaging setting, X-rays are used to depict the structure of an object. The interaction of the radiation with matter is used to gather information about the sample. The physics of these interactions can be described in a particle picture, via microscopic effects, or in a wave picture, via wave propagation.

2.2.1 Microscopic Interactions

In the particle picture, two main interaction effects can occur in the energy range typically used for imaging: the photoelectric effect and scattering. Additional effects, such as pair production if the incident photon energy is large enough, can be neglected for imaging.

Photoelectric Effect

With the photoelectric effect an incident X-ray photon is absorbed and its energy is transferred to a bound electron in the atomic shell. This leads to a release of the electron into the continuum if the binding energy is exceeded. The empty position in the shell is filled with an electron from an outer shell, that emits either a fluorescent photon or an Auger electron. The cross-section of the photoelectric effect is strongly depending on the atomic number Z and the photon energy E, but cannot be modeled analytically. For most cases in the field

of biomedical X-ray imaging, a semi-analytical approach exists:

$$\sigma_{ph} \approx C_p \frac{Z^{4-5}}{E^{3-4}}, \tag{2.2.1}$$

where C_p describes a constant [Whi77; HJ80]. This approach is valid for small atomic numbers, $Z<25$ and no absorption edges.
An absorption edge occurs when the energy of the photon becomes large enough to release electrons from inner atomic shells, especially the K-shell, creating an abrupt increase in the cross-section.

Incoherent and Coherent Scattering

Incoherent scattering, also known as Compton scattering describes the scattering of a photon on a bound electron. A photon collides with an electron of the outer shell and transferring energy and momentum onto the electron. The scattered photon is shifted in energy, depending on the scattering angle Θ_{ph} between the initial pathway and the scattered photon:

$$\Delta\lambda = \lambda_s - \lambda_0 = \lambda_c(1 - \cos\Theta_{ph}), \tag{2.2.2}$$

where λ_0 is the incoming photon wavelength, λ_s the scattered and $\lambda_c = \frac{h}{m_e c}$ the Compton wavelength. The electron moves with the obtained energy and momentum. The cross-section for scattering can be calculated with the Klein-Nishina formula [KN29].
Coherent, elastic scattering is described as Thomson or Rayleigh scattering. It is dominant over incoherent scattering at low energies. Wavelength and energy of the photon stay the same, but the direction of the scattered photon is changed.

2.2.2 Wave Picture

The second way to describe the interaction of X-rays with matter, is to treat them as electromagnetic wave $\Psi(\vec{x}, t)$ at location $\vec{x}$ and time-point t:

$$\Psi(\vec{x}, t) = \Psi_0 e^{i(\vec{k}\cdot\vec{x}-\omega t)}, \tag{2.2.3}$$

with the amplitude Ψ_0, the wavevector $\vec{k}$ with $|\vec{k}| = \frac{2\pi}{\lambda}$, and the angular frequency ω. Typical

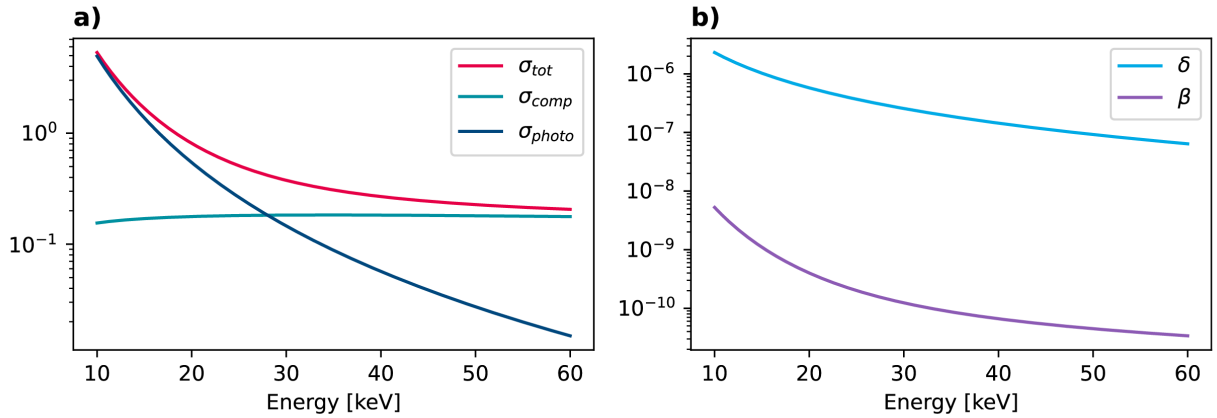

Figure 2.2.1: Energy dependent cross-sections and refractive index of liquid water. In **a)** the contributions of the photo and the Compton effect to the total cross section can be seen. For energies below approx. 28 keV, the photoelectric effect is dominant. In **b)** the refractive index decrement and the imaginary part of the refractive index are plotted. The refractive index decrement is several orders of magnitude larger, than the imaginary part.

wavelengths are in the region of Å (10^{-10} m). In order to describe the interaction of an X-ray wave with the material, a complex index of refraction can be introduced:

$$n_\omega(\vec{x}) = 1 - \delta_\omega(\vec{x}) + \mathrm{i}\,\beta_\omega(\vec{x}), \tag{2.2.4}$$

where δ describes the refractive index decrement of the real part, and β describes the imaginary part. As the real part of the refractive index is only slightly smaller than unity (numerically one), it is expressed by the refractive index decrement. The values for δ are ranging from 10^{-8} in air to 10^{-5} in solid materials. At the same time, β is typically much smaller.

If an X-ray wave propagates in direction z through a sample with a refractive index n, it can be described by the following equation and split into parts:

$$\Psi(z,t) = \Psi_0 \cdot e^{i(nkz-\omega t)} = \Psi_0 e^{i(kz-\omega t)} \cdot e^{-\beta kz} \cdot e^{-i\delta kz}. \tag{2.2.5}$$

The first part describes the free-space propagation of the wave. The second part describes the attenuation of the wave by the complex part of the refractive index. The third exponential function describes the phase-shift caused by δ. This process is illustrated in Fig. 2.2.2.

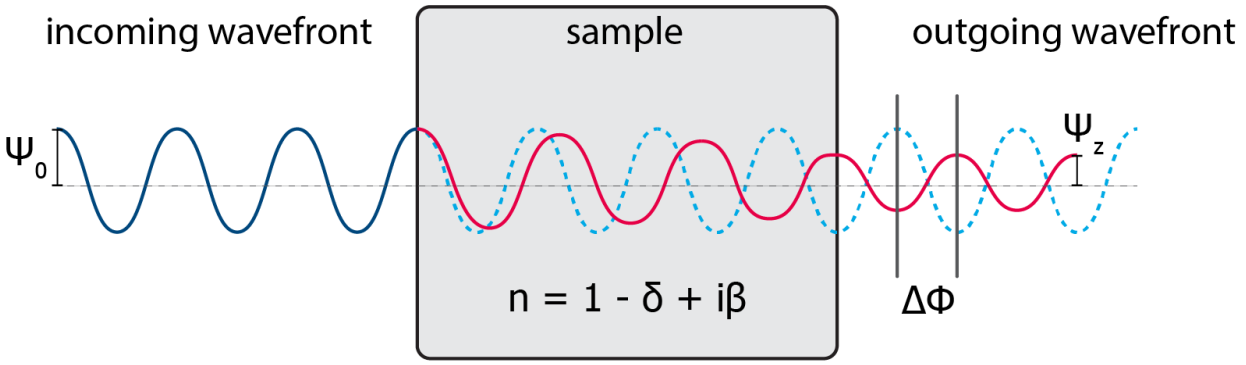

Figure 2.2.2: Interaction of an X-ray wave with matter. The incoming wave with amplitude Ψ_0, depicted as the solid blue line, passes a sample with a complex index of refraction n. After the object, depicted in solid red, the amplitude of the wave is reduced to Ψ_z, and the phase is shifted by $\Delta\Phi$, compared to the free space propagation in dashed blue.

Attenuation

The reduction in amplitude of an X-ray wave, that has passed an object, can be calculated by looking at the intensity, which is defined as $|\Psi|^2$:

$$I(z) = |\Psi_0 e^{i(kz-\omega t)} \cdot e^{-\beta kz} \cdot e^{-i\delta kz}|^2 = \Psi_0^2 e^{-2\beta kz}. \tag{2.2.6}$$

By describing the incoming intensity as $\Psi_0^2 = I_0$ and defining a linear attenuation coefficient as $\mu = 2\beta k$, one ends up with the so called Beer-Lambert law, describing the attenuation of monoenergetic X-rays in a homogeneous object of thickness z:

$$I(z) = I_0 \cdot e^{-\mu z}. \tag{2.2.7}$$

The linear attenuation coefficient can also be linked to the microscopic interactions by the total cross-section σ_{tot}:

$$\mu = \frac{\rho N_A}{A} \cdot \sigma_{tot}(E, Z), \tag{2.2.8}$$

at energy E, atomic number Z, atomic mass A, mass density ρ, and the Avogadro constant N_A. With this the energy and material dependence of the absorption can be described.

Phase-Shift

The third part of Eq. 2.2.5 describes a shift of the phase of an X-ray wave. For a homogeneous object, the shift in phase can be expressed by:

$$\Delta\Phi = \delta k z. \tag{2.2.9}$$

Furthermore, the phase-shifting properties can be related to the local electron density ρ_e, assuming the following relation:

$$\delta = \frac{2\pi r_0 \rho_e}{k^2}, \tag{2.2.10}$$

with the wave-vector of the radiation k, the classical electron radius r_0 [AM11].
The phase-shift of an X-ray wave by an object is equivalent to a deflection of the beam by the sample. For a small phase gradient the refraction angle α can be described by [Dav+95]:

$$\alpha \approx \frac{1}{k}\frac{\partial\Phi(x)}{\partial x} \tag{2.2.11}$$

2.3 Detection of X-rays

In order to be used for imaging, the intensity of an X-ray beam has to be measured. For modern digital detection systems, two basic principles are used.
The direct detection uses semiconductor materials. By converting the incident radiation to electron-hole-pairs, X-ray photons can be registered. This can be done as integrating detector, where the total amount of incoming radiation during the exposure time is measured, or as photon-counting detector, where the readout electronics are fast enough to register single photons and count them.
The second detection principle is the indirect detection. The X-ray photons are converted to visible light photons, using scintillator materials. This has the advantage of enabling the use of a broad range of detection electronics. Most medical applications use flat-panel detectors, where an array of photo-diodes behind the scintillator is used for detection. For high-resolution applications the scintillator can be bounded directly to a camera chip or a camera objective can be used.
The choice of scintillator material is dependent on the desired parameters for light yield, afterglow and material thickness, as they influence factors such as speed, quantum efficiency

and resolution of the detector considerably [YR97]. Typical scintillator materials for medical imaging include CsI and GadOx, for lens-coupled detectors $CdWO_4$ and LuAG.

2.4 Tomographic Imaging

First applications of X-ray imaging concentrated on the acquisition of projection images. With the introduction of digital detectors and the development of modern computers, further progress became possible. The task of fully obtaining 3D volumetric information was achieved with the introduction of computed tomography. Allan Cormack and Godfrey Houndsfield received the Nobel Prize for Physiology or Medicine in 1979 "for the development of computer assisted tomography" [ABc]. Since then, CT has become a widely applied method from medical imaging in clinics to materials research down to nanoscopic scales. The fundamental principles are similar for all applications and have been discussed by many authors. This section is mainly based on [Rad86; KS01; Buz11].
CT delivers a solution to the problem of how to reconstruct volumetric information about a sample, form a set of angular projections. A common approach to perform this reconstruction is Filtered Backprojection (FBP). For simplicity of the explanations, the following section will assume a parallel beam geometry. All functions in real space will be described using small letters, all functions in Fourier space will use capital letters.

2.4.1 Radon Transform

The unknown object is described by an object function $f(x, y)$. The Radon transform is the mathematical description of an angular projection of this function. For a projection angle θ it is defined as:

$$p_\theta(r) = \mathcal{R}_\theta(f(x,y)) = \int_0^d f(r,s)\mathrm{d}s = \iint_{-\infty}^{\infty} f(x,y)\delta(x\cos\theta - y\sin\theta - r)\mathrm{d}x\mathrm{d}y. \quad (2.4.1)$$

A direct inversion of the Radon transform would be computationally expensive and is not feasible for measured data. Therefore a detour over the Fourier Slice theorem is necessary.

2.4.2 Fourier Slice Theorem

The Fourier Slice theorem connects the Fourier transform of the projections of the Radon transform to two-dimensional Fourier transform of the object function. The latter is given as

$$F(u,v) = \mathcal{F}\left(f(x,y)\right) = \iint_{-\infty}^{\infty} f(x,y) e^{-2\pi i(xu+yv)} \mathrm{d}x\mathrm{d}y. \tag{2.4.2}$$

The Fourier transform of the projection p_θ is calculated as

$$P_\theta(u) = \mathcal{F}\left(p_\theta(r)\right) = \int_{-\infty}^{\infty} p_\theta(r) e^{-2\pi i r u} \mathrm{d}r. \tag{2.4.3}$$

The connection can be made by looking at the 2D Fourier transform of the object function along a line across the origin at an angle θ. Taking Eq. 2.4.3 and inserting the Radon transform Eq. 2.4.1:

$$P_\theta(\omega) = \int \left[\iint f(x,y)\delta(x\cos\theta - y\sin\theta - r)\mathrm{d}x\mathrm{d}y \right] e^{-2\pi i r\omega} \mathrm{d}r. \tag{2.4.4}$$

One can change the order of integration and evaluate the inner integral:

$$P_\theta(\omega) = \iint \left[\int f(x,y)\delta(x\cos\theta - y\sin\theta - r) e^{-2\pi i r\omega} \mathrm{d}r \right] \mathrm{d}x\mathrm{d}y \tag{2.4.5}$$

$$= \iint f(x,y) e^{-2\pi i\omega(x\cos\theta - y\sin\theta)} \mathrm{d}x\mathrm{d}y. \tag{2.4.6}$$

By setting $u = \omega\cos\theta$ and $v = -\omega\sin\theta$ one can identify the Fourier transform of the object function:

$$= \iint f(x,y) e^{-2\pi i\omega(xu+yv)} \mathrm{d}x\mathrm{d}y \Big|_{u=\omega\cos\theta, v=-\omega\sin\theta} \tag{2.4.7}$$

$$= \mathcal{F}_{2D}\left(f(x,y)\right)(u,v) \Big|_{u=\omega\cos\theta, v=-\omega\sin\theta} \tag{2.4.8}$$

$$= F(u = \omega\cos\theta, v = -\omega\sin\theta) \tag{2.4.9}$$

Two problems arise from directly trying to invert the radon transform using this approach. At first, data-points are radially distributed over a polar grid the Fourier space. This means an interpolation step becomes necessary. Second, the sampling becomes sparser with increasing

distance from the center, meaning lower sampling for higher spatial frequencies.

2.4.3 Filtered Backprojection (FBP)

The algorithm of FBP deals with the problem of regridding and uneven sampling, by performing this transformation analytically. The Fourier slice theorem gives the object function as inverse 2D Fourier transform:

$$f(x,y) = \frac{1}{2\pi} \iint_{-\infty}^{\infty} F(u,v) e^{2\pi i(xu+yv)} \mathrm{d}u\mathrm{d}v. \tag{2.4.10}$$

Changing to the polar coordinate system with $u = \omega\cos\theta$ and $v = -\omega\sin\theta$ and substituting the differentials $\mathrm{d}u\mathrm{d}v$ to $|\omega|\mathrm{d}\omega\mathrm{d}\theta$, considering the Jacobi determinant, gives:

$$f(x,y) = \frac{1}{2\pi} \int_{0}^{2\pi} \int_{-\infty}^{\infty} F(\omega\cos\theta, \omega\sin\theta) e^{2\pi i\omega(x\cos\theta - y\sin\theta)} |\omega| \mathrm{d}\omega\mathrm{d}\theta. \tag{2.4.11}$$

Applying the Fourier slice theorem and replacing the 2D Fourier transform $F(\omega\cos\theta, \omega\sin\theta)$ with the Fourier transform of a projection at an angle θ results in the following:

$$f(x,y) = \frac{1}{2\pi} \int_{0}^{2\pi} \int_{-\infty}^{\infty} P_\theta(\omega) e^{2\pi i\omega(x\cos\theta - y\sin\theta)} |\omega| \mathrm{d}\omega\mathrm{d}\theta. \tag{2.4.12}$$

The factor $|\omega|$ from the Jacobi determinant and the inner integral can be interpreted as filtering the projection in Fourier space with a high-pass filter, weighting high spatial frequencies more, to account for the sparser sampling. To account for noise in real applications, different variant of the frequency weighting have been introduced. The linear ramp filter $|\omega|$ is also known as Ram-Lak filter [RL71]. Other filters, as e.g. the Shepp-Logan filter or the Hamming filter are weighting high frequencies less, reducing noise in the reconstruction at the cost of a potential loss of spatial resolution.

2.4.4 Nyquist-Shannon Sampling Theorem

The minimum required number of projection angles to fully recover the volumetric information is given by the Nyquist-Shannon sampling theorem. Based on the number of pixels

covered by the sample in a row of the detector used, N_{pix}, the number of angular steps needs to fulfill:

$$N_{proj} \geq \frac{\pi}{2} N_{pix}. \tag{2.4.13}$$

If this condition is not fulfilled, the reconstruction will have a loss of spatial resolution and can display so-called undersampling artifacts.

Phase-Contrast Imaging and Image Analysis Methods

3

In this chapter, phase-contrast imaging is introduced, and the used phase-retrieval techniques are described, namely, Speckle-Based Imaging (SBI). Giving a short overview of the principle and then focusing on one specific algorithm Unified Modulated Pattern Analysis (UMPA). Furthermore, methods for processing and characterizing a phase-contrast scan are introduced.

3.1 Phase-Contrast Imaging

The most common imaging applications using X-rays focus on the attenuation of the radiation. This probes the imaginary part β of the sample's complex index of refraction. However, also changes in the real-valued refractive index decrement δ can be visualized and used for imaging.

3.1.1 Overview of Techniques

The idea to visualize the phase-shifting properties of a specimen was first applied to visual light microscopy, for which Fritz Zernike was awarded the Nobel Prize in physics in 1953 [ABb]. As the phase of a wavefront is not directly measurable, it has to be converted into an intensity modulation on the detector. For X-rays, many methods were developed over the course of the years. The first works by Bonse and Hart focused on crystal interferometers [BH65; Bec98]. Later, propagation-based phase contrast was added [Sni+95; Clo+96; Pag+02]. Grating interferometry methods were introduced by David et al. [Dav+02], Momose et al. [Mom+03] and Weitkamp et al. [Wei+05a], and extended by Pfeiffer et al. to low coherent sources [Pfe+06]. Other methods are analyzer-based imaging [IB95; Dav+95], coded aperture [OS07]. As the most recent addition, Speckle-Based Imaging (SBI) was added to the list of phase-contrast methods [BWS12; Bér+12b; MPS12]. This method will be covered in detail in Sec. 3.2.

The main advantage of using the phase as an imaging contrast mechanism is improved soft tissue contrast [Fit00]. Crystal interferometers are able to record the phase-shift directly. The other methods record either the first (analyzer-based imaging, GBI, SBI) or the second derivative (PBI).
The ability of a phase-contrast imaging method to distinguish even small phase shift differences is measured by the sensitivity. For Differential Phase-Contrast (DPC) methods, this can be defined as the standard deviation level in the background of a differential projection. The sensitivity depends on the phase-retrieval method as shown in e.g. [Zan+13a; Rui+16; Lan+14].
While for absorption contrast, quantitative imaging is well established [Don07], not all phase-retrieval methods cover this aspect. Differential methods are used to retrieve quantitative data [Her10; Zdo+20a], while some PBI methods are not able to do so.

3.1.2 Propagation-Based Imaging

The idea of PBI is to recover the phase-shifting properties of a sample from the intensity pattern behind the sample. Under the condition of coherent illumination, the outgoing wavefront will show interference effects.
At synchrotron beamlines, the illumination conditions are easy to fulfill, and due to the simple measurement, most experiments are able to perform a PBI scan. In order to recover both attenuation and phase-shift, two independent measurements are necessary. This can be achieved by measuring at two different propagation distances or at different photon energies. This is done for holotomography [Clo+99].
For recovering the phase-shift from a single measurement, assumptions about the sample have to be made. One option is to assume a pure phase object with no attenuating properties [Bro99]. A second option was introduced by Paganin et al. [Pag+02]. Based on the Transport of Intensity Equation (TIE) [Tea83], a monochromatic incoming wave and a homogeneous object, or alternative, a constant ratio of δ over μ in the object, is assumed. In addition, a near-field condition has to be fulfilled. With these assumptions, the thickness T of the object can be recovered from a single measurement $I(\mathbf{x}_\perp, z = R)$ at distance R:

$$T(\mathbf{x}_\perp) = \frac{1}{\mu} \ln\left(\mathcal{F}^{-1}\left\{\mu \frac{\mathcal{F}\left\{I(\mathbf{x}_\perp, z = R)/I_0\right\}}{R\delta|k_\perp|^2 + \mu}\right\}\right), \tag{3.1.1}$$

Where I_0 denotes the incident intensity and $k_\perp$ the Fourier coordinates. The assumption of a

homogeneous object works reasonably well for a large class of samples. Due to its simplicity, this method is among the standard methods offered at synchrotron experiments. Although this method is extremely popular and powerful, the assumption of a homogeneous object results in only qualitative phase information.

3.1.3 Grating-Based Imaging (GBI)

Grating-Based Imaging (GBI) or Talbot interferometry uses the Talbot self-imaging effect of periodic structures [Tal36]. At certain distances, called Talbot distances, and fractions of it, a self-image of the structure is reproduced. These distances are given by:

$$d_T = \eta \cdot \frac{2p^2}{\lambda}, \tag{3.1.2}$$

where p describes the grating period and λ the wavelength of the incoming radiation. The factor η is dependent on the type of grating:

$$\eta = \begin{cases} n \text{ for an absorbing grating} \\ \frac{n}{4} \text{ for a } \frac{\pi}{2} \text{ phase-shifting grating} \\ \frac{n}{16} \text{ for a } \pi \text{ phase-shifting grating,} \end{cases} \tag{3.1.3}$$

and uneven n.

In a Talbot interferometer, the Talbot effect is used by placing a grating in a coherent beam. This grating acts as a beam splitter and produces a so-called Talbot carpet. The typical periods of such a grating are in the range of microns. If now a sample is placed in the beam path, the Talbot carpet is distorted. In order to analyze these distortions, two cases can be differentiated.
In the first case, the spatial resolution of the detector is good enough to directly resolve the modulation of the carpet. This can be achieved at synchrotron sources.
In the second case, the detector resolution is larger than the period. In this case, a second grating, a so-called analyzer grating, can be introduced. This absorbing grating is mounted in front of the detector and matched in the period to the Talbot carpet.
The phase-shift of a sample is retrieved by stepping one of the gratings laterally perpendicular to the grating direction. With this, an intensity oscillation is recorded in each detector pixel.

By using a Fourier analysis approach, the attenuation and the phase-shift can be determined by comparing the stepping curve with and without the sample. GBI retrieves a differential phase-signal perpendicular to the grating structure. The total phase-shift can be obtained via line-wise integration, which can be combined with the tomographic reconstruction in a modified filter kernel.
The advantage of GBI for many experimental applications is that it can be transferred to laboratory sources via the introduction of a third grating, the so-called source grating. This configuration is often referred to as the Talbot-Lau interferometer. The combination of the interferometer with low-coherent sources makes this method promising for medical applications.

3.1.4 Multimodal Imaging and Dark-field Signal

Many experimental techniques and setups are able to measure several means of contrast simultaneously; so far, absorption and phase contrast have been introduced. This is called multimodal imaging. In addition to phase and attenuation information, a third imaging signal can be measured. The so-called dark-field signal is connected to small-angle scattering [MB92; Pfe+08]. It can be defined through the visibility of a pattern, which can either be defined through the intensity I in a region as:

$$v = \frac{I_{max} - I_{min}}{I_{max} + I_{min}}, \tag{3.1.4}$$

or through the ratio of standard deviation to mean:

$$v = \frac{\sigma(I)}{\bar{I}}. \tag{3.1.5}$$

The dark-field signal corresponds to a loss of visibility by small-angle scattering.

3.2 Speckle-Based Imaging (SBI)

SBI developed as a rather recent phase-contrast technique in the last ten years [BWS12; Bér+12b; MPS12]. The basic idea is to use a random wavefront modulator. This modulator has a variety of names in literature: wavefront marker, speckle pattern, and diffusor. By imprinting an intensity pattern on the illumination, which can be resolved by the detector,

the first SBI methods used direct pixel-wise windowed correlation analysis to track the changes a sample induces to the pattern.

3.2.1 Tracking Algorithms

With more tracking algorithms available, a rough classification into implicit and explicit tracking methods can be made. Implicit tracking methods [Pag+18; Pav+20b; Pav+20a] are related to PBI and based on the transport of intensity equation or the X-Ray Fokker-Planck equation [PM19]. They assume either a transparent sample [Pag+18; Pav+20b] or a homogeneous sample [Pav+20a] and are thus non quantitative.
Explicit tracking methods rely on correlation analysis or cost functions to retrieve the signals. The first implementations can be described as Single-shot X-ray Speckle-Tracking (XST). The displacement of the wavefront marker pattern by the phase is analyzed by cross-correlating a window around each pixel of the sample projection to the reference projection, to obtain a shift-vector. This shift vector is connected to the refraction angle by [Zdo18]:

$$\alpha_{x,y} = \frac{u_{x,y} \cdot p_{eff}}{d}, \tag{3.2.1}$$

where $u_{x,y}$ denotes the shift vector in x- or y-direction, p_{eff} the effective pixel size of the detector and d the propagation distance from the sample to the detector. The transmission signal is calculated as the ratio of the means of the intensity in each tracking window:

$$T = \frac{\bar{I}}{\bar{I}_0}. \tag{3.2.2}$$

The dark-field signal can be obtained by the ratio of the sample visibility to the reference visibility using Eq. 3.1.4:

$$D = \frac{v_{sample}}{v_{reference}} = \frac{\Delta I/\bar{I}}{\Delta I_0/\bar{I}_0} = \frac{1}{T}\frac{\Delta I}{\Delta I_0}. \tag{3.2.3}$$

The spatial resolution of this approach is limited to twice the size of the full width at half maximum (FWHM) of the analysis window. The window size itself has to be chosen larger than the speckle size.
Further development to achieve high spatial resolution resulted in X-ray Speckle Scanning (XSS), where the wavefront marker is stepped in small steps, smaller than the average speckle size, along a regular grid [BWS12]. Phase-retrieval is performed similarly to XST, where the

displacement is now given in units of wavefront marker steps.
The latest approaches focus on random wavefront marker positions. The phase-steps are now larger than the average speckle size and can be chosen arbitrarily, with the limitation, that they have to be repeatable. This loosens the requirements on the experimental hardware. For phase-retrieval, X-ray speckle vector tracking (XSVT) was the first proposed idea [BZ15]. Instead of using a window around a pixel for analysis, a vector along the image stack is created by taking the same pixel of each phase-step. This vector of the sample image is then correlated to the reference image vectors, to obtain the displacement. The approach can be extended to a mixed XST-XSVT approach by combining the window and the vector [BZ16; BZ17], allowing for tuning sensitivity and resolution.
The latest addition to explicit speckle-tracking with random wavefront marker positions was the Unified Modulated Pattern Analysis (UMPA) [Zdo+17; Zdo18; Zdo+20a]. The correlation analysis of the previous approaches is replaced by a model for the detected intensity as a function of the imaging signals:

$$I_j(\vec{x}) = T(\vec{x})\{\bar{I} + v(\vec{x})[I_{0j}(\vec{x} + \vec{u}) - \bar{I}]\}, \tag{3.2.4}$$

where $I_j(\vec{x})$ describes the intensity at position $\vec{x}$ for step j, $T(\vec{x})$ the transmission of the sample at that position, $\bar{I}$ the mean reference intensities, $v(\vec{x})$ the visibility, and I_{0j} the reference intensity at step j. The vector $\vec{u}$ describes a lateral shift of intensity, induced by the phase shift of the sample.
The phase-retrieval is computed by minimizing a cost function, defined by the squared difference of the modeled to the measured intensity in an analysis window. The sensitivity of this approach is dependent on the number of phase steps N and the window size w as follows:

$$\sigma = \frac{C}{w\sqrt{N}}, \tag{3.2.5}$$

where C is a setup dependent constant. The resolution is again limited to twice the FWHM of the analysis window, where UMPA uses a Hamming window function. This speckle-tracking technique was used in the course of this work.

3.2.2 Speckle Tracking Approximation

The basics of explicit speckle tracking can be derived from a wave propagation point of view. This section is mainly based on the paper of Morgan et al. [Mor+20] and will use its

notation. More details about the approximations used for the derivation can be found in the book of Paganin [Pag+06].
SBI is a near field imaging method, thus the governing equation for the wave-propagation is the Fresnel diffraction. The intensity by a monochromatic wavelength λ on a detector at distance z can be expressed as:

$$I_{ref}(\mathbf{x}, z) = \frac{1}{(\lambda z)^2} \left| \iint T(\mathbf{x}') \exp\left(i\pi \frac{|\mathbf{x} - \mathbf{x}'|^2}{\lambda z} \right) \mathrm{d}\mathbf{x}' \right|^2 . \tag{3.2.6}$$

If the illumination is not homogeneous, but described by a profile

$$p(\mathbf{x}, 0) = \sqrt{w}(\mathbf{x}) \exp[i\Phi(\mathbf{x})], \tag{3.2.7}$$

Eq. 3.2.6 changes to:

$$I(\mathbf{x}, z) = \frac{1}{(\lambda z)^2} \left| \iint T(\mathbf{x}') p(\mathbf{x}', 0) \exp\left(i\pi \frac{|\mathbf{x} - \mathbf{x}'|^2}{\lambda z} \right) \mathrm{d}\mathbf{x}' \right|^2 . \tag{3.2.8}$$

To be able to perform a speckle tracking, one needs a geometric transformation between a sample and a reference image. One approach to do so in outlined in [Zan+14]. There, the phase is approximated to the first order, the absorption to the zeroth order:

$$\Phi(\mathbf{x}') = \Phi(\mathbf{x}) + (\mathbf{x}' - \mathbf{x}) \cdot \nabla\Phi(\mathbf{x}) + \Phi_H(\mathbf{x}') \tag{3.2.9}$$

$$\sqrt{w}(\mathbf{x}') = \sqrt{w}(\mathbf{x}) + \sqrt{w}_H(\mathbf{x}'), \tag{3.2.10}$$

where the higher order terms are denoted as $\Phi_H(\mathbf{x}')$ and $\sqrt{w}_H(\mathbf{x}')$ and approx 0. This gives:

$$p(\mathbf{x}', 0) \approx \sqrt{w}(\mathbf{x}) \exp\left[i(\Phi(\mathbf{x}) + (\mathbf{x}' - \mathbf{x}) \cdot \nabla\Phi(\mathbf{x})) \right] \tag{3.2.11}$$

Inserting this in Eq. 3.2.8:

$$\begin{aligned} I(\mathbf{x}, z) &\approx \frac{w(\mathbf{x})}{(\lambda z)^2} \left| \iint T(\mathbf{x}') \exp\left[i(\mathbf{x}' - \mathbf{x}) \cdot \nabla\Phi(\mathbf{x}) \right] \times \exp\left(i\pi \frac{|\mathbf{x} - \mathbf{x}'|^2}{\lambda z} \right) \mathrm{d}\mathbf{x}' \right|^2 \\ &= \frac{w(\mathbf{x})}{(\lambda z)^2} \left| \iint T(\mathbf{x}') \exp\left[\frac{i\pi}{\lambda z} \left| \mathbf{x} - \mathbf{x}' - \frac{\lambda z}{2\pi} \nabla\Phi(\mathbf{x}) \right|^2 \right] \mathrm{d}\mathbf{x}' \right|^2 . \end{aligned} \tag{3.2.12}$$

Where the following was used:

$$\left|\mathbf{x}-\mathbf{x}'-\frac{\lambda z}{2\pi}\nabla\Phi(\mathbf{x})\right|^2 = |\mathbf{x}-\mathbf{x}'|^2 - 2\,|\mathbf{x}-\mathbf{x}'|\left|\frac{\lambda z}{2\pi}\nabla\Phi(\mathbf{x})\right| + \left|\frac{\lambda z}{2\pi}\nabla\Phi(\mathbf{x})\right|^2. \tag{3.2.13}$$

Due to approximating the phase by only the first order, the third part is dismissed.
The second part of Eq. 3.2.12 can be rewritten as:

$$= w(\mathbf{x})I_{ref}\left[\mathbf{x}-\frac{\lambda z}{2\pi}\nabla\Phi(\mathbf{x}), z\right] \tag{3.2.14}$$

Eq. 3.2.14 can be interpreted as a lateral displacement of intensity by the local gradient of the phase. This result is the basis of UMPA and other explicit speckle tracking algorithms. While the approximations used for this result, enable a direct solution for the tracking, neglecting higher orders can become problematic. Compared to other, more elaborate phase-retrieval techniques, such as e.g. near-field ptychography, the speckle tracking approximation only approximates the phase to the first order. Higher orders are not included in the model and can cause visible artifacts. For practical experiments, the second order is of special interest, as it causes the so-called edge-enhancement. Sharp edges are highlighted in the images by fringes around the edges. This effect is utilized in PBI, and also included in some implicit speckle-tracking methods, but when explicit tracking methods are used, the fringes are usually attributed to the transmission channel. As consequence, the retrieved sample transmission is not a pure attenuation signal, but a mixture of the absorptive properties of the sample and higher order phase-effects.

3.3 Dynamic Flat-Field Correction

Included in many SBI phase-retrieval algorithms (and many other techniques) is the assumption of a stable illumination. For practical experiments however, this condition is only satisfied to a limited extent.
Conventional images attenuation images are often obtained by a so-called flat-field correction. It can be described as:

$$n_j = \frac{p_j - \bar{d}}{\bar{f} - \bar{d}}, \tag{3.3.1}$$

where the projection p_j is corrected for a mean dark-current image $\bar{d}$ and divided by an averaged flat-field image $\bar{f}$. The average dark-current and flat-field images are used, to lower

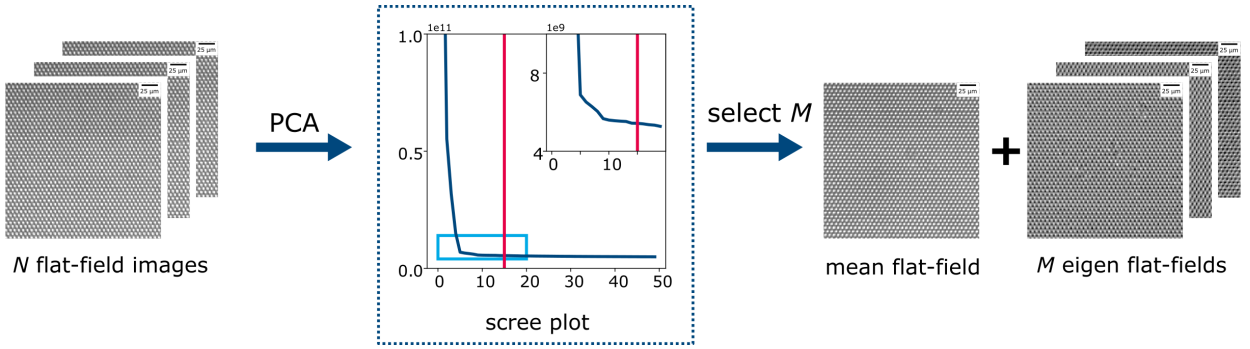

Figure 3.3.1: Principle of the eigen flat-field image generation. A PCA is calculated on the N flat-field images of a phase-step. By using a scree-plot the relevant M components are selected. This is done by sorting the eigenvalues and determining where a shoulder in the values can be identified. In this case, this happens after approx. 9 components. Most of the times a few more (15) were kept. The remaining components are discarded and the results include a mean flat-field and M eigen flat-field images.

the influence of noise. This works reasonably well for stable illumination conditions. If the illumination is not stable in intensity or position, better results can be obtained, by replacing the average flat-field image, with an individually determined one f_j for each projection.

$$n_j = \frac{p_j - \bar{d}}{f_j - \bar{d}}. \tag{3.3.2}$$

This can be especially useful for SBI, as this requires reference images to be captured at precisely the same wavefront marker position as the sample projections. Otherwise, the sensitivity of a differential projection will get deteriorated.
Simple approaches to determine an individual flat-field, try to correlate the sample projections with the reference projections by using a metric, e.g. the structural similarity index. While this can compensate for some inaccuracies, it requires a large number of references. To account for a certain degree of changes during the measurement, a dynamic flat-field correction can be used. For this, a Principal Component Analysis (PCA) is performed on the flat-field images of each grating position f_j [Van+15]. This yields several so-called eigen flat-field images u_k and their corresponding eigenvalues. By using a scree plot, the most relevant M components can be chosen and the remaining components discarded. This is illustrated in Fig. 3.3.1

In order to generate a best-fitting reference image at an unknown position of the wavefront marker, a new reference image f_n can be expressed by a weighted sum over the relevant

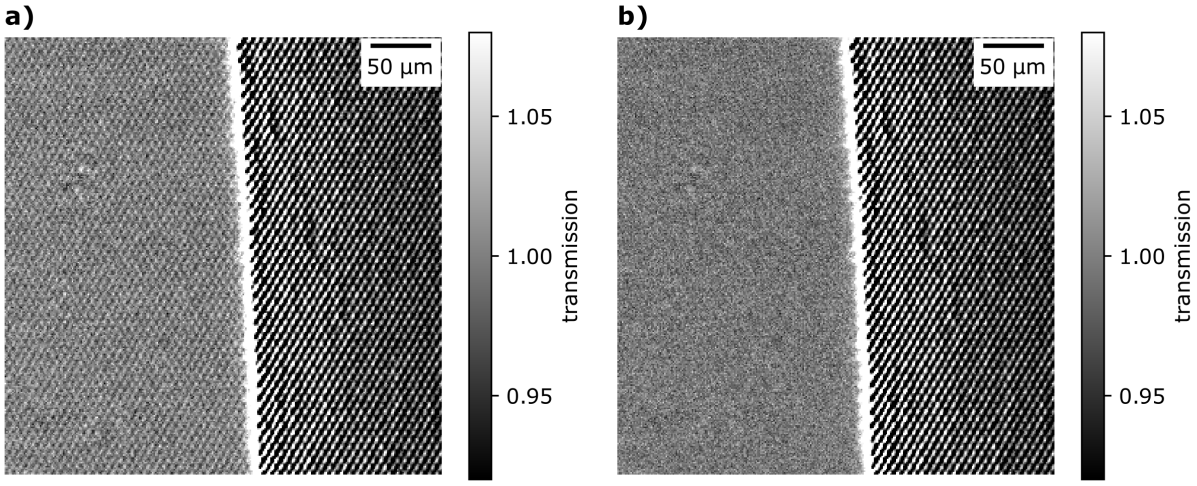

Figure 3.3.2: Comparison of the usage of a mean flat-field image in **a)** and a dynamically generated flat-field image in **b)**. The images show a section of the background on the left and a sample container on the right. With the dynamic correction, the grating pattern in the background vanishes, while it is still visible when using a mean flat-field image.

components:

$$f_n = \bar{f}_j + \sum_{k=1}^{M} w_k \cdot u_k. \tag{3.3.3}$$

The optimal weights can be calculated, by defining a cost function in a background region the projection p_{BG}. Using a least-squares minimization of the difference between the projection and the flat-field image, the set of weights is determined:

$$w_k = \arg\min_{w_k} \left(p_{BG} - f_{n,BG}\right)^2. \tag{3.3.4}$$

The resulting weights are then used to generate the reference image according to Eq. 3.3.3. The effect of this correction is shown in Fig. 3.3.2. For illustration, a single projection with the grating in the beam was flat-field corrected. The image shows the background on the left and the edge of a sample container on the right. In **a)** a mean flat-field was used. The grating pattern produces artifacts in the background, mainly due to position shifts. When a dynamically generated flat-field image is used in **b)**, the artifacts are no longer visible and the background is flat.

With this approach, drifts of the wavefront marker can be modeled to some extent, improving the sensitivity and reducing fixed pattern structures in the projections, ultimately reducing

ring artifacts in the reconstruction. The effects of the dynamic flat-field corrections are also compared in Sec. 5.1.2.

3.4 Spatial Resolution in Phase-Contrast Imaging

Apart from the sensitivity, the spatial resolution of a phase-contrast measurement is also of interest, as some phase-sensitive measurement techniques can deteriorate the resolution compared to an absorption scan.
The resolution of a setup is connected to the Optical Transfer Function (OTF) of the system [Buz11]. The OTF describes the effect of a system on different spatial frequencies. However, a direct measurement of the OTF is not possible. Therefore alternative ways to determine the spatial resolution have to be found.

3.4.1 Influences on the Spatial Resolution

For conventional absorption tomography, the influences on the spatial resolution are well known. Relevant parameters include the source spot size, the detector behavior, and if used, additional optical elements. For micro CT at a synchrotron facility, the source size is typically small enough, as the experiments are located far away from the insertion devices. More relevant are the detector properties. In the case of a lens-coupled detector, the thickness of the scintillator material, the properties of the lenses, and the properties of the camera are determining the resolution.
In addition to the detector, also the properties of the illumination can add blurring to an image. This is the case if a measurement is conducted using a sheared illumination. Weitkamp et al. [Wei+05b] described this for a grating interferometer using a beam-splitter grating. In the case of a π-shifting grating with a duty cycle of 0.5, most of the intensity is diffracted in the +/- 1st diffraction order. This can be used to determine the beam separation caused by the shear:

$$\Delta s = 2\frac{\lambda}{p_1} d_T = 4\frac{d}{d_T} p_1, \tag{3.4.1}$$

where λ describes the wavelength, p_1 the period of the used grating, d_T the Talbot distance and d the distance from grating to detector.
For non π-shifting gratings and other duty cycles, the contribution of different diffraction intensities changes [Bér+12a; MG78]. The amount of smearing is reduced if the contribution

from the 0th diffraction order increases.
This effect is not only limited to periodic structures, but anything causing a shearing in the illumination, e.g. showing refractive properties, will to some extent add a blurring to an image.

3.4.2 Measuring Spatial Resolution

As theoretical considerations are not easily feasible for SBI, measuring the achieved spatial resolution in a scan is necessary. This can be done on the projection level or on the reconstructed volume.
Especially for projections, phantom measurements are well established. By measuring a sharp edge (knife edge), a so-called Line Spread Function can be determined. Its Fourier transform represents a 1D slice of the 2D OTF. The spatial resolution can be defined at a cut-off spatial frequency, at which the OTF drops below a defined value.
Phantom measurements are complex in the case of tomographic imaging, especially if the spatial resolution of the phase-contrast is of interest. More convenient are methods, which try to determine the spatial resolution directly from the measured samples. Numerous ways to do so exist, however not all methods are compatible with processed data.

Edge Fitting

The straightforward approach is to look at sharp edges in an image and determine their blur. For this, a line is plotted orthogonal to the edge, and a Gaussian error-function (ERF) is fitted to the intensity profile:

$$a \cdot erf(\frac{x-\mu}{\sqrt{2}\sigma}) + b = a \cdot \frac{2}{\sqrt{\pi}} \int_0^{\frac{x-\mu}{\sqrt{2}\sigma}} e^{-\tau^2} d\tau + b. \tag{3.4.2}$$

As a resolution criterion, the FWHM of the associated Gaussian can be used, which corresponds to:

$$FWHM = 2\sqrt{2\ln 2}\sigma. \tag{3.4.3}$$

The advantage of this method lies in the sensitivity to processing, as it directly looks at features and not at the influence of noise. On the other side, it requires sharp edges to be present in the sample.

Fourier Ring Correlation

Fourier Ring Correlation (FRC) takes a different approach to determine the resolution [Van+82], [VS05]. The basic idea of this concept is, to correlate spatial frequencies in the Fourier domain. For features, this correlation is high, for noise, it is low. In combination with threshold criteria, the resolution is determined. In order to determine the FRC two independent measurements are required. This can also be achieved by subdividing the image into four subsets, by taking every second pixel horizontally and vertically. The subsets are Fourier transformed and rings around the zero frequency are correlated. In this work, the resolution is determined by identifying the intersection of a filtered FRC with a full-Bit and a half-Bit criterion, equivalent to each pixel containing an information content of 1 bit or 1/2 bit respectively. The advantage of this method lies in its independence of the sample. On the other hand, if correlated noise is introduced, the results are corrupted.
As phase-retrieval requires processing the raw detector images, the results of the FRC might only be seen as approximate for either small UMPA window sizes or small regularization strength of PBI. Similar problems arise when analyzing the Fourier power spectrum as described by Modregger et al. [Mod+07].

4 Experimental Setup

In this chapter the experimental setup used for this work is presented. Focusing on the basics on the micro CT endstations of the beamlines P05 and P07 operated by the Helmholtz-Zentrum Hereon at PETRA III, DESY. The additions to the setup for phase-contrast imaging are introduced, as well as the measurement protocols. In the end, the data processing workflow is described.

4.1 Basic Setup

For the experiments in this work, the beamlines P05 and P07 at the PETRA III storage ring at DESY in Hamburg, Germany were used. The beamlines are operated by the Helmholtz-Zentrum Hereon as part of the platform German Engineering Materials Science Center (GEMS). They are equipped with micro CT endstations, where the measurements were conducted.

4.1.1 Storage Ring PETRA III

The Deutsches Elektronen-Synchrotron DESY operates multiple user facilities for photon science experiments in the district of Bahrenfeld in Hamburg, Germany. One user facility is the PETRA III storage ring [DESb]. With its pre-accelerators LINAC II, PIA, and the synchrotron DESY II, PETRA III is the storage ring and light source. The technical parameters are listed in Tab. 4.1.1, a drawing of the structure can be found in Fig. 2.1.1 textbfa).

PETRA III currently hosts a total of 23 beamlines operated by multiple partners. Each beamline can have several experimental endstations, so more than 60 experiments are in operation. The Helmholtz-Zentrum Hereon operates experiments for X-ray diffraction and

PETRA III Machine Parameters	
Circumference	2.3 km
Electron Energy	6.0 GeV
Number of Bunches	40 (timing) 480-960 (multi bunch)
Beam Current	100 mA - 120 mA
Top-up Mode	Yes
Source Size Horizontal	34.6 µm
Source Size Vertical	6.3 µm
Divergence Horizontal	28.9 µrad
Divergence Vertical	1.6 µrad

Table 4.1.1: Machine parameters of PETRA III. Source size and divergence are given for low-beta sections [Bar+08].

X-ray imaging at multiple beamlines. At two of the imaging endstations, the measurements for this work were done.

4.1.2 Imaging Beamline P05

Most of the experiments were conducted at the Imaging Beamline (IBL) P05 [Gre+14; Wil+16; Hai+10]. A schematic drawing of the beamline is shown in Fig. 4.1.1. The beamline front-end is equipped with an 2 m U32 undulator source and can access energies between 5 and 50 keV. After front-end filters and slit systems, the beam exits the ring and is led into the optics area. There three monochromators are available: a channel-cut monochromator for energies up to around 20 keV, a Double Crystal Monochromator (DCM) in Bragg geometry, and a Double Mulitlayer Monochromator (DMM). As the DMM can introduce distortions to the beam and lower the coherence, it was found not suited for most of the measurements, even though it can offer a higher flux than the DCM. The DCM produces a monochromatic spectrum with a bandwidth of $\frac{\Delta E}{E} = 10^{-4}$. After additional slit systems, the beam is passed to the experimental endstations. In the first experimental hutch EH1, a nano CT setup is located. If this is not in use, an evacuated beam-pipe can be installed and the beam is transferred to the second experimental hutch EH2, where the micro CT setup is located. Additional parameters of the beamline are listed in Tab. 4.1.2.

Beamline Parameters P05	
Photon Source	Undulator U32
Energy Range	5 keV - 50 keV
Source Brilliance	10^{14} ph/s/0.1% bw
Max. Flux on Sample	$1.3{\cdot}10^{12}$ ph/s/mm^2 at 18 keV

Table 4.1.2: Beamline parameters of the Imaging Beamline P05 [Wil].

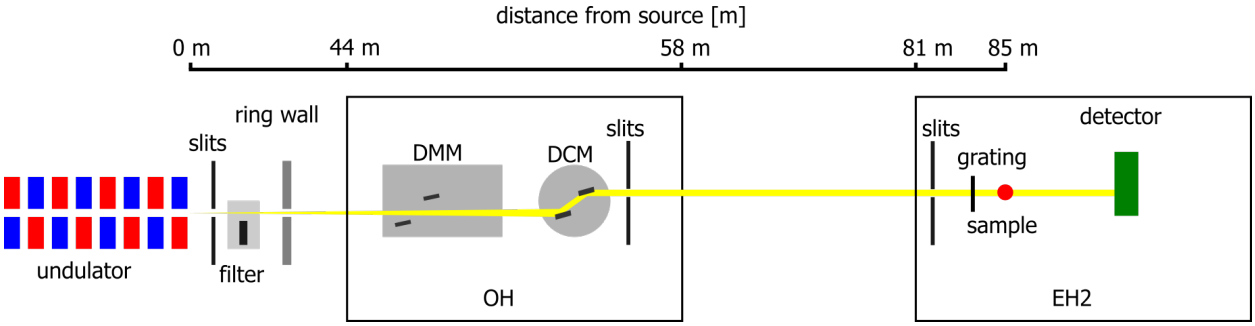

Figure 4.1.1: Layout of the P05 beamline. The undulator in the PETRA III storage ring is the radiation source. After an initial slit system, one can choose to include filters in the white beam, to lower the flux and the heat load on the monochromator. After passing the ring wall, the beam gets in the optics hutch (OH), where the monochromators are located. Typically the DCM is used for DPC measurements. Additional slit systems can collimate the beam. The beam is conducted through the first experimental hutch (EH1, not shown) and arrives in the second experimental hutch (EH2) where the microtomography experiment is located.

Beamline Parameters P07	
Photon Source	Undulator IVU21
Energy Range	50 keV - 200 keV
Source Brilliance	10^{18} ph/s/0.1% bw
Max. Flux on Sample	$5{\cdot}10^{12}$ ph/s/mm^2 at 100 keV

Table 4.1.3: Beamline parameters of the High Energy Material Science Beamline P07 [Sch].

4.1.3 High Energy Materials Science Beamline P07

For high-energy experiments, the High Energy Material Science (HEMS) beamline P07 was used. The parameters of the beamline are listed in Tab. 4.1.3. In contrast to P05, P07 is equipped with a 4 m IUV21 in-vacuum undulator, which can access energies from about 30 keV to more than 200 keV. As a monochromator, a bent Laue DCM is used. By bending the crystals, the bandwidth and flux can be increased if necessary. The micro CT endstation is located in the fourth experimental hutch EH4.

4.1.4 Microtomography Setup

Both beamlines, P05, and P07 have a similarly designed micro CT setup. The setup is constructed on a base granite structure (Hereon Technikum, Geesthacht, Germany and PI Micos, Karlsruhe, Germany), to decouple it from floor vibrations. On top of the base structure, two additional granites are installed. The first carries an air-bearing rotation stage from Aerotech Inc. (Pittsburgh, USA). Inside the rotation stage, two crossed piezo motors are located, on which the sample is mounted via sample-pins. The detector system is placed on a second granite structure and can be moved in beam direction, to allow selecting a propagation distance from sample to detector between 0 mm and 1300 mm. The detector itself is a lens-coupled system, manufactured by POG (Löbichau, Germany) with an interchangeable scintillator screen. The optical microscope behind the scintillator offers objectives with 5, 10, 20, or 40-fold magnification.
Typically used scintillator materials include LuAG and $CdWO_4$ in thicknesses between 30 µm and 300 µm. For this work, high-resolution measurements were taken using a 30 µm LuAG screen, while standard measurements used a 100 µm $CdWO_4$ for better light yield.
A variety of camera systems is available, depending on the aim of the measurement. This

includes camera systems for fast measurements, low noise measurements, and for large Field of View (FOV) measurements. For scans in this work, two camera systems were in use. To use the largest FOV possible, a camera system from Ximea was used, the CB500MG with a CMOSIS CMV50000 sensor, a physical pixel size of 4.6 µm and a sensor pixel size of 50 MP (7920 px. width and 6004 px. height). At five-fold magnification this camera can use the full width and height of the beam, resulting in a FOV of approx. 7 mm in width and up to 3 mm in height. For the characterization of the gratings, a CMOS camera developed in a collaboration with the KIT, based on a CMOSIS CMV 20000 sensor was installed. The effective pixel size was with the 10-fold magnification objective at 0.64 µm. This camera can also be used for tomographic scans.
Before starting a measurement at the setup, the components were aligned with each other. The camera and the microscope were focused on the scintillator, by placing a highly absorbing edge in the beam and calculating the modulation transfer function (MTF). The focus is varied until the best resolution at 10 % MTF is obtained. The Rotation of the camera to the tomographic axis was aligned, as well as the tilt of the axis.
The setup is able to scan a large variety of sample classes from biological to material science samples. Standard scans are either absorption scans or PBI phase-contrast scans. Additional sample environments can be installed on top of the rotation stage, including a furnace, a load-frame, and a hanging axis. In addition, an automatic sample changer robot arm exists, which can mount samples from a magazine.
The experimental control software is based on IDL. Motor communication is realized via Tango controls.

4.2 Differential Phase-Contrast Setup

To enable Differential Phase-Contrast (DPC) measurement, the setup can be adapted. During the course of this thesis, a new DPC setup was developed. The aim was to replace the GBI setup, constructed by Hipp [Hip18], and to increase the spatial resolution. Furthermore, a simplification of the setup, to enable easier user application was wished.
The design of the newly constructed setup is referring to Speckle-Based Imaging (SBI) setups, with changes in the used wavefront marker. Instead of random wavefront markers, such as sandpaper or steel wool, a 2D phase grating structure is used. This structure is a so-called Talbot Array Illuminator (TAI).

4.2.1 Talbot Array Illuminators

A Talbot Array Illuminator (TAI) is a type of phase-grating structure, which give under coherent illumination a binary intensity modulation through Fresnel diffraction [Sul97]. With the goal of optimizing the visibility of the pattern, a focusing effect of such gratings can be used.

We focused on gratings with a duty cycle of $DC = 1/3$ and phase-shifts of $\phi = \frac{2\pi}{3}$. This produces a 1:3 focusing in each direction at a fractional Talbot distance of $1/6\, d_T$. The grating lattice structure can be square or hexagonal.

The gratings for P05 were produced by the company 5microns, Ilmenau, Germany, via deep reactive ion etching (DRIE) on 200 µm thin silicon wafers. The processing steps include UV lithography, DRIE, removing the photoresist by O_2 plasma etching, and sawing the waver. The gratings have an active area of $1\,\text{cm} \times 1\,\text{cm}$ and the waver was cut to tiles of $1.5\,\text{cm} \times 1.5\,\text{cm}$. The etching depth is designed to match a phase-shift of $\phi = \frac{2\pi}{3}$ at a target energy. Available gratings are designed for 10, 15, 20, and 30 keV corresponding to etching depths of 8.5, 13, 17, and 26 µm, in periods of 5, 6.8, and 10 µm for a square lattice and 5, 7 and 10 µm for a hexagonal lattice. For high energy measurements, a second set of gratings was manufactured by Proton Mikrotechnik for 40, 50, 60, and 70 keV with periods of 10, 13, and 15 µm, again with square and hexagonal lattice structures.

The structure of the gratings is illustrated in Fig. 4.2.1. In **a)** a 3D model of the hexagonal lattice is shown. For manufacturing simplifications, the holes were not designed as hexagons, but as circles. In Fig. 4.2.1 **b)**, an scanning electron micrograph of the grating is shown. For quality and etching depth control, an additional wafer was etched and a hexagonal 7 µm grating was broken to scan the cross-section. The shown structure was dry etched for 42 cycles, reaching an etching depth of 8.6 µm. Due to the so-called RIE lag, smaller structures are etched slower. The number of etching cycles was matched to the 7 µm structures. This would imply that smaller periods are manufactured for slightly lower energies and larger periods for slightly higher energies. In practice, even at energy offsets of 5 keV, no significant loss of pattern visibility was observed.

The Talbot carpet was simulated in [Gus+21]. For the given configuration, this confirmed the expected binary modulation and focusing at a fractional Talbot distance of $1/6\, d_T$. A slice of the carpet is shown in Fig. 4.2.2 **d)**. The simulation also predicted an even stronger modulation slightly before and after $1/6\, d_T$. Further characterization of the TAIs can be found in Sec. 5.1.1.

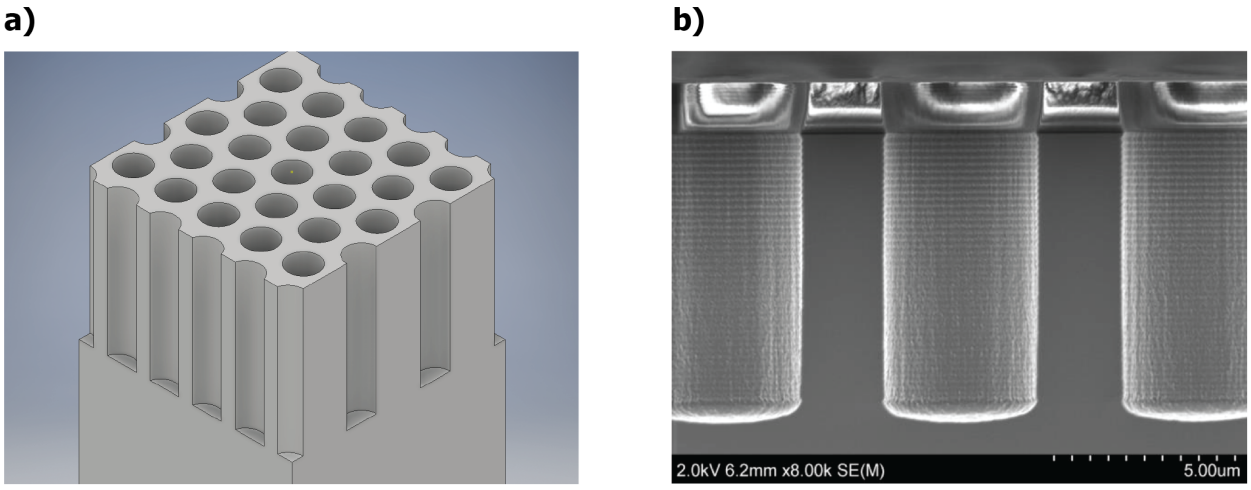

Figure 4.2.1: Structure of the used TAIs. In **a)** a 3D model of the hexagonal structures is shown. Instead of hexagonal holes, circular ones are used. In **b)** a scanning electron microscopy image of the cross-section is shown. The broken grating had a hexagonal structure with a period of 7 µm and was dry etched for 42 cycles.

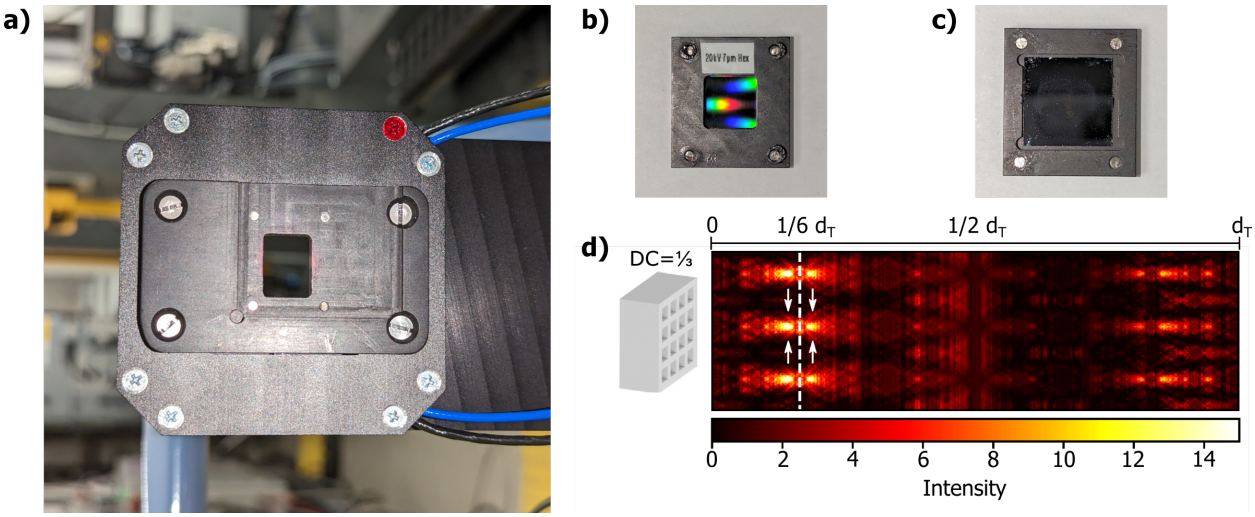

Figure 4.2.2: Mounting of the gratings on the piezo. In **a)** the mounting plate on the piezo is shown. The TAIs are glued into small frames using wax. The front view is shown in **b)** and the back view in **c)**. The frames are fixed via four magnets on the mounting plate. The frames have an aperture of 1x1 cm, corresponding to the active area of the TAIs. In **d)** a slice of the simulated Talbot carpet is shown. It predicts a binary modulation at a fractional Talbot distance and possibly even stronger modulations before and after this. Fig. **d)** was adapted from [Gus+21].

a) **b)**

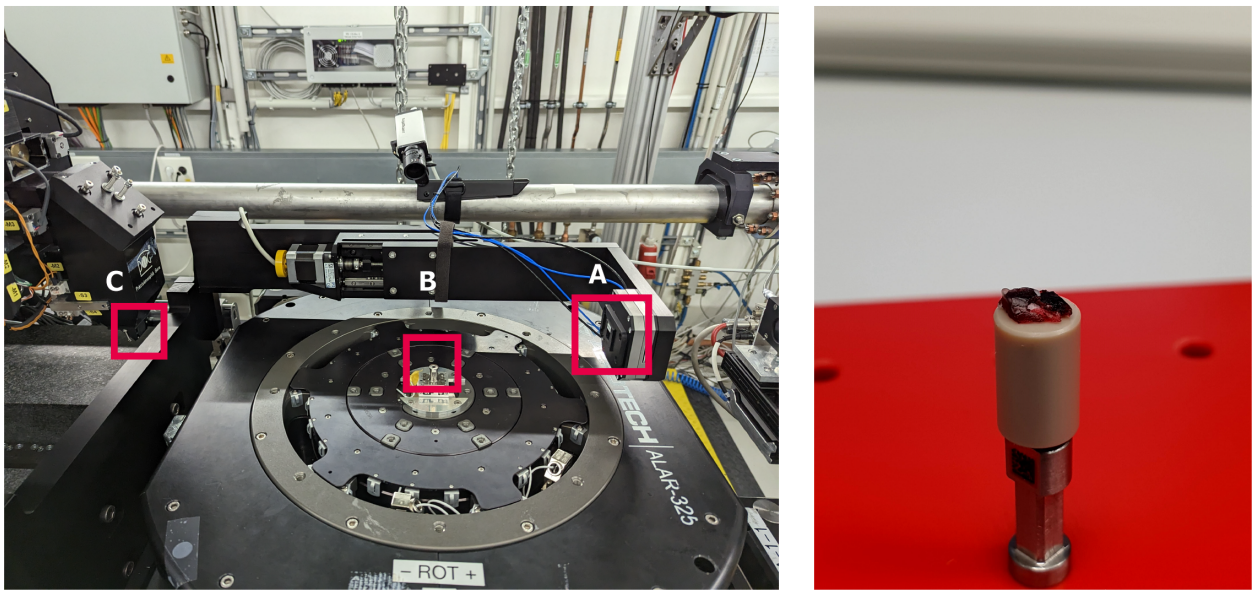

Figure 4.2.3: Photography of the DPC setup in **a)**. The beam enters the experiment from the right side of the image. The TAI is mounted on the piezo stepper in **A**. The sample is positioned on the rotation axis **B**, and the detector scintillator **C** is placed in a fractional Talbot distance of the TAI. In **b)**, a picture of a sample, mounted on a pin is shown. A robotic arm can be used to automatically insert the pin from a magazine into the rotation axis.

4.2.2 Setup Adaptions

For DPC measurements, the micro CT setup is modified. The additions to the setup are designed as a grating holder arm, which can be mounted onto the side of the front plate of the camera granite. The length of the arm can be modified by a linear stage, as well as long holes. At the end of the arm, a 2D piezo motor with an aperture, a PXY 201 CAP from piezosystemJena, is located. The usage of a piezo table with an aperture ensures minimal grating oscillation. The piezo has a capacitive position measurement system to ensure repeatability. The TAI gratings are glued into holder frames as shown in Fig. 4.2.2 **b)** and **c)**. The frames are mounted via magnets on the mounting plate on the piezo, depicted in Fig. 4.2.2 **a)**.

A photography of the setup is shown in Fig. 4.2.3 **a)**. The TAI is mounted on the piezo stepper in **A**. The sample can be inserted into the rotation axis at **B**, and the detector scintillator **C** is placed at the working distance. In contrast to prior designs, the mounting of the grating holder arm at the right side of the setup (seen from the beam direction), allows using the robotic sample changer, which can automatically transfer a sample pin from a magazine to the rotation axis.

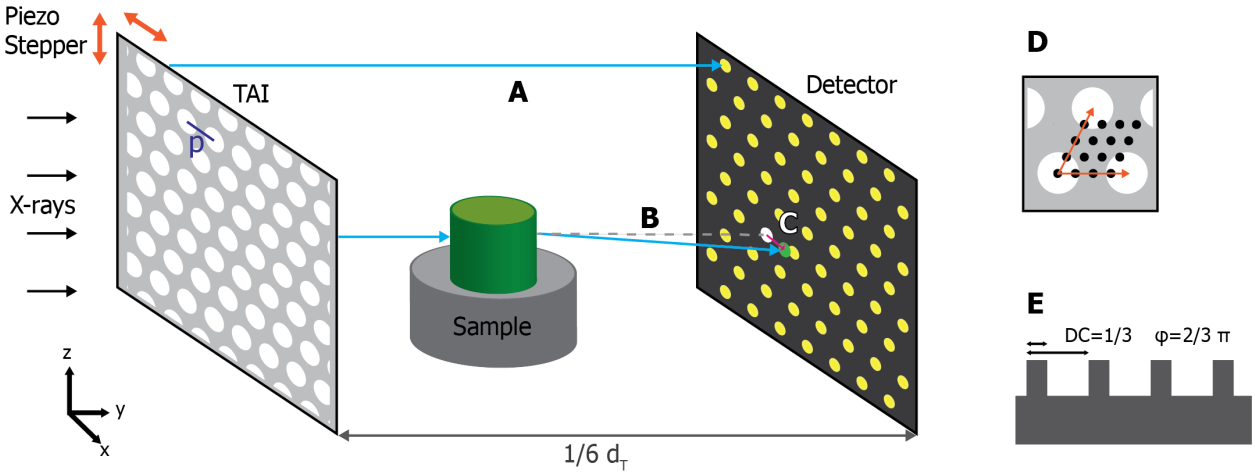

Figure 4.2.4: Schematic drawing of the TAI setup. The incoming X-rays pass the grating. The detector is placed in a fractional Talbot distance of $d = 1/6d_t$, with the sample on the rotation stage in between the grating and the detector. If no sample is in the beam, the TAI produces a spot pattern as shown in **A**. If a beamlet passes the sample, the pattern behind it will be distorted from its original place **B** to a shifted location **C**. For a TAI scan, multiple tomographic scans are recorded, while the grating is moved by the piezo stepper in between the scan. The stepping is performed along the grating axes, within a grating cell as shown in **D**. The used gratings are TAIs with a duty cycle of $DC = 1/3$ and a phase shift of $\phi = \frac{2\pi}{3}$.

In Fig. 4.2.3 **b)** a picture of a sample on a pin is shown. Paraffin-embedded samples, like the one in the picture, were directly mounted on the pin cap, using hot glue. For liquid-embedded samples, Eppendorf tubes or Kapton cylinders were used.

The working principle of the setup is shown in Fig. 4.2.4. The TAI is placed upstream of the sample on the piezo stepper. The detector is positioned in the operation distance of $1/6d_T$. If no sample is in the beam, the gratings produce a regular intensity modulation in the form of small spots, as shown in **A**. Even though the modulation pattern on the detector is created by diffraction effects, each grating spot can be treated as a beamlet for a simplified description. If now a sample modifies the phase, the beamlets get shifted laterally **C**, from its original path **B**. This shift is tracked during the phase-retrieval.

4.3 Scan Recording, Data Processing, and Phase Retrieval

For a measurement with the phase-contrast setup, the grating holder arm is mounted to the camera front plate, and a TAI suited for the energy is chosen. The distance from the grating

to the camera scintillator is set to the fractional Talbot distance of the grating.

4.3.1 Scan Recording

Scans using the TAI setup are usually recorded using continuous rotation (fly) scans. For a complete scan, multiple individual scans are taken, while the grating is stationary during each scan. In between the scans, the grating is stepped to the next position, and the process is repeated. The procedure of the scan macro is outlined in Fig. 4.3.1.The number of phase steps is chosen as a squared number to scan the unit cell of a grating homogeneously, as illustrated in Fig. 4.2.4 **D**. So-called step-scans, where the rotation is stopped during image acquisition, were tested, but apart from slightly fewer ring artifacts, no advantage was visible. As the scan time of a step scan is increased compared to fly scans, due to a larger motor position overhead, fly scans were chosen as the standard.

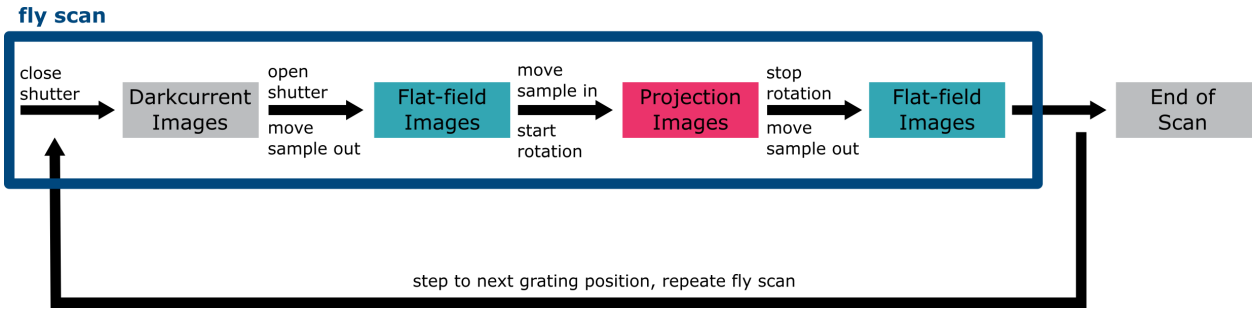

Figure 4.3.1: Schematics of the procedure of the scan macro. Each DPC scan consists of multiple fly scan. During a scan, the wavefront marker is kept stationary. At the beginning of each scan, darkcurrent images are obtained. Flat-field image are recorded before and after the sample projections. If a single fly scan is finished, the grating is moved to the next position and a new fly scan is started.

While for most scans a total of 16 phase steps was used, fast scans can be done using only 9 steps, and higher sensitivity can be reached by using 25 steps or more. The influence of the number of phase steps on the sensitivity is described by Eq. 3.2.5. The number of phase-steps has also an impact on the phase-retrieval computation time.
The number of projection angles is determined by the sample size and the detector width. For practical reasons, to lower the scan time, a slight degree of undersampling is accepted. The exposure time is dependent on the energy, flux on the detector, and detector microscope zoom and typically in a range between 80 ms to 200 ms per projection.
As setup and wavefront marker stability is crucial for the phase-retrieval, the scan macros

were modified. Previously, the whole sample stage was moved to acquire flat-field projections. However, this showed to cause slight tilts in the setup, which are detectable with the gratings. As consequence, the sample is moved for DPC scans, using the piezo inside the rotation axis. This means significantly less mass is moved, and the tilt is avoided. However, problems can occur if the sample dimensions are exceeding the travel range of the piezo and the sample cannot be moved out of the FOV completely.
The usable FOV is slightly smaller than the detector, as the processing requires empty areas at the sides of the sample in the size of a few tens of pixels to perform the dynamic flat-field correction. If a larger FOV is needed, it is possible to scan a sample off-axis. For this, the rotation axis shifted to the sides, and the scan uses a full 360° rotation with an even number of angular projections. This almost doubles the FOV. The dynamic flat-field correction then only works on one side.

4.3.2 Data Processing and Phase-Retrieval

The typical file size of a raw scan is in the range of 2 - 4 TB. Due to the scanning scheme, where the phase-steps are recorded as individual tomographic scans, post-processing has to be started after the scan is finished. The processing workflow is shown in Fig. 4.3.3.
Data processing starts with processing the flat-field images. Each image is corrected for the camera dark current and weighted with the beam current. As the next step, the eigen flat-field images are calculated for each phase step as described in Sec. 3.3. The eigen flats are blurred, using a Gaussian blur to lower noise, and saved on the file system.
The phase-retrieval is computed independently for each angular projection. At an angular step, all phase-steps are loaded and corrected for dark current and beam current. A predefined area at the sides of the image, preferably both sides, where no sample is in the beam is used to determine an adapted flat-field image using a weighted sum of the eigen flat-field images. The individual weights are determined using a least-square minimization.
Phase-retrieval is computed, using UMPA as a Python package. For improved performance, the group around Pierre Thibault implemented UMPA in C++ and provided the implementation [De +22]. Parameters that can be defined for the retrieval include the window size and whether the dark-field signal should be included in the model or not. More details about UMPA can be found in Sec. 3.2. The calculated channels are shown in Fig. 4.3.2.
In the following, the abbreviations in brackets note the name of the channels used in the processing. The stack of phase-steps and corresponding flat-field images are averaged over all steps and divided, to perform a standard flat-field correction and acquire the attenuation

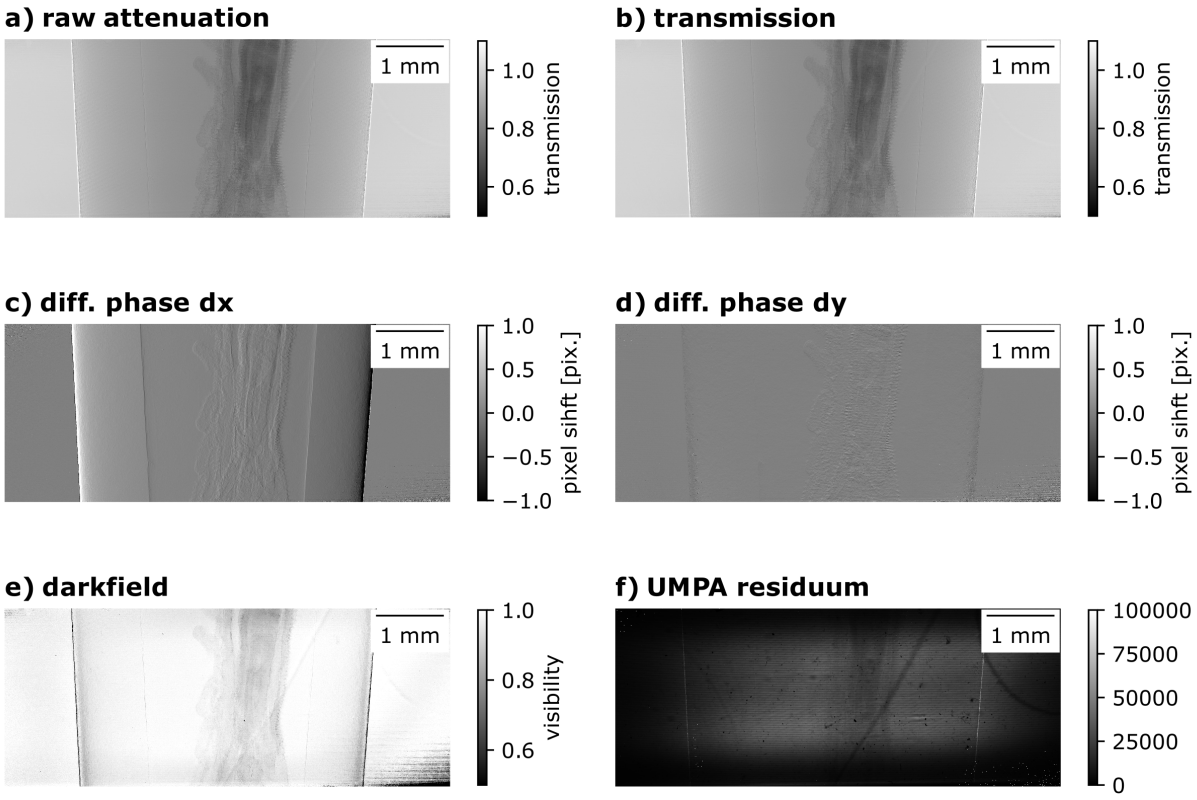

Figure 4.3.2: Resulting channels from the UMPA phase-retrieval. In **a)**, the raw attenuation image is shown, calculated as mean over all phase-steps of a projection. **b)**, shows the UMPA transmission channel. In **c)** and **d)** the differential phase in x- and y-direction is shown. In **d)** the darkfield signal and in **f)** the UMPA residuum are depicted.

signal (att). UMPA calculates the differential phase signals in x- and y-direction (dx and dy), the sample transmission (T), optionally the dark-field signal (df), and the cost function residuum (f). All channels are saved as TIFF files. In addition, all parameters during the processing are saved into a log file.

If the sample was scanned off-axis, opposing angles are stitched together. The overlap is used to determine and correct phase ramps on the differential phase in the x-direction. In order to do so, the phase in the overlap is subtracted. Using the empty area next to the sample, and the subtracted overlap, a linear fit is performed and the ramp is subtracted. The images are then stitched, using linear weights at the border.
The differential phase images are corrected for outliers, by using a threshold in the UMPA residuum to identify affected pixels a mask is generated for each projection. The masked

pixels are interpolated from the surrounding pixels. As a second step, an area with no sample on both sides of the image is used to fit a phase ramp and this is subtracted from the phase images.
In order to avoid artifacts from the Fourier transform, the images are mirrored before integration. Compared to simple mirroring, anti-symmetric mirroring of the differential phase images as described by Bon et. al. [BMW12] reduced artifacts further. The differential phase images are integrated using a Fourier integration approach [Kot+07]:

$$\Phi(x,y) = \mathcal{F}^{-1}\left(\frac{\mathcal{F}\left(d_x\Phi + id_y\Phi\right)(k,l)}{2\pi i(k+il)}\right). \tag{4.3.1}$$

After integration, the images are cut to the original size and multiplied by a factor to consider the measurement parameters. This includes the energy, the effective pixel size, and the distance from the sample to the detector and gives the quantitative phase shift. After this step, the phase-retrieval is completed, and the scan is ready for tomographic reconstruction.

4.3.3 Tomographic Reconstruction

For tomographic reconstruction, the processed projections of the desired channel are loaded into the memory. Available channels for reconstruction are:

- att: the attenuation image, corresponding to a PBI projection
- Int_q: the integrated phase signal
- T: the UMPA transmission channel
- dx: the UMPA differential phase in x-direction
- df: optional, the UMPA dark-field signal

After loading into the memory, the projections are filtered for ring artifacts. Two ring filters on the projection level can be applied. The first filter starts by averaging all projections. This blurs the sample but leaves the ring causing structures. Next, the averaged projection is blurred using a median filter and divided by the unblurred projection. By this, a weighting mask is calculated and applied to all individual projections. The second ring filter is based on a band rejection filter. As the TAIs tend to cause remaining grating structures in the

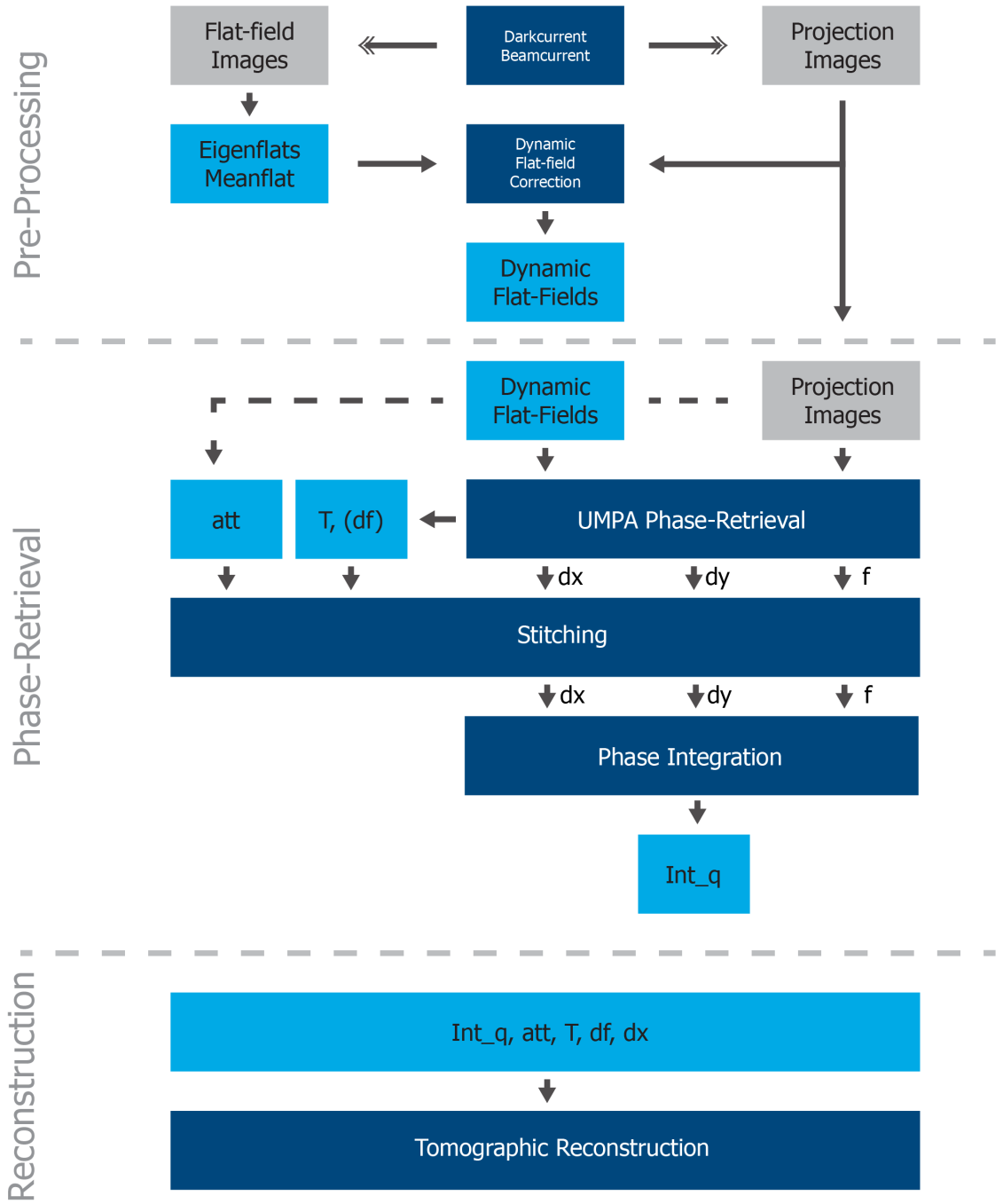

Figure 4.3.3: Schematic workflow of the data processing. The abbreviations correspond to the ones used in the processing scripts. Raw images are marked in gray, intermediate images in light blue, and processing methods in dark blue. At first, the flat-field images are pre-processed and eigen flat-field images are calculated. These are used to perform a dynamic flat-field correction for each projection image. The UMPA phase-retrieval uses the projections and dynamic flat-field images. In addition, an unprocessed flat corrected image is calculated as the average over all phase-steps. If the scan was recorded off-axis, opposing projections are stitched. During phase integration, outliers are interpolated and the total phase-shift is reconstructed via 2D Fourier integration. Tomographic reconstruction includes ring-filtering and filtered backprojection.

retrieved projections, the Fourier transform of an averaged projection is calculated. The grating frequencies are suppressed by applying a minimum filter to the Fourier transform. Again a weighting mask is acquired by dividing the filtered image by the unfiltered one. The mask is applied to the Fourier transform of each projection. For performance reasons, the last step is implemented as a real-valued Fourier transform.
The ring-filtered images are then reconstructed using a cone beam reconstruction with the given setup geometry. For comparability, the reconstructed phase is converted into units of electron density, assuming the following relation:

$$\rho_e = \frac{k^2}{2\pi r_0} \cdot \delta, \tag{4.3.2}$$

with the wavevector of the beam energy k, and the classical electron radius r_0. The reconstructed slices are saved as float32 TIFF files and can be used for further analysis.

4.3.4 Implementation on the DESY Maxwell cluster

During the scope of this work, the previously described processing workflow was implemented on the DESY Maxwell cluster. The complete workflow is designed in Python 3, and available as a virtual mamba (variant of the conda package manager in C++ [Qc23]) environment. For performance reasons, large parts of the processing are designed using multiple compute nodes and multiprocessing.
The cluster is managed via a SLURM scheduler. The steps of pre-processing and phase-retrieval are based on CPU implementations. After the eigen flat-field image generation, each angular projection can be processed individually. For this, multiple nodes are allocated and work independently from each other. To avoid multiple nodes working on the same projection, a status file is used to flag a projection as already being worked on. As the Maxwell cluster is organized in multiple partitions, cancellation of individual workers without prior notification can happen to some of them. However, these partitions offer a large number of nodes, which can be used if not otherwise occupied. In order to catch sudden cancellations, multiple searches for missing projections are carried out, when the status file signals all projections as being processed.
After phase-retrieval and integration, the tomographic reconstruction needs to be computed. For this the software X-Aid from Mitos(Garching, Germany) is used. As this step is computed on GPUs and requires data from all angular steps, multi-node processing is not useful any longer, and the node allocations are released. The tomographic reconstruction is com-

puted on a single GPU node, with large memory.
More details on how to use the implementation can be found in the Appendix.

Phase-Contrast Imaging Using TAIs at PETRA III

5

In the first part of this chapter, the previously described setup is characterized. Relevant parameters are the TAI visibility, the phase sensitivity, and the spatial resolution. The effects of the processing steps on those parameters are analyzed.
In the second part of the chapter, some exemplary measurements of the setup are shown. Four different series of samples are presented, where different aspects of the setup are highlighted. The measurements of this thesis were distributed over multiple beamtimes. Most of the development at P05 was part of the long term proposal LTP II-20190765. For the high energy scans at P07, beamtime was granted for the proposal I-20200511. The mouse lymph nodes were scanned as part of the proposal I-20190799.

5.1 Setup Characterization

The previously existing GBI setup at the beamline P05 [Hip18] was replaced by one described in chapter 4. As the new setup is based on SBI setups, several characteristics were in the focus of optimization. The first focus was set on the wavefront marker. The visibility of the used TAIs was analyzed. In the next step, the relevant figures of merit of a phase-contrast imaging setup, including the setup's capability to resolve small differences in refraction angles, as well as its capability to resolve small spatial details were investigated. The first of these parameters is described by the sensitivity of the setup, and the second by the spatial resolution.
Parts of this characterization, especially regarding the TAIs were published in Gustschin et al. [Gus+21], others, regarding sensitivity and resolution, in Riedel et al. [Rie+21].

Talbot Carpet Parameters					
TAI	Design Energy	Beam Energy	Exposure Time	Distance Step	Maximum Distance
10 µm hexagonal	20 keV	20 keV	70 ms	10 mm	1300 mm
10 µm square	20 keV	20 keV	70 ms	10 mm	1250 mm
7 µm hexagonal	20 keV	20 keV	70 ms	10 mm	1000 mm
10 µm hexagonal	30 keV	30 keV	100 ms	10 mm	1000 mm
10 µm square	30 keV	30 keV	100 ms	20 mm	1000 mm
7 µm hexagonal	30 keV	30 keV	100 ms	5 mm	1200 mm
10 µm hexagonal	20 keV	30 keV	100 ms	50 mm	1200 mm

Table 5.1.1: Parameters of the Talbot carpet scans.

5.1.1 Grating Characterization

Talbot Carpet Scans For SBI techniques, a wavefront marker with a high visibility and a small structure size is necessary. In the newly designed setup, the sandpaper used in previous descriptions of SBI setups was replaced by TAIs.
This replacement comes with geometric restrictions, as the TAIs have their maximum expected visibility at a fractional Talbot distance of $1/6\,d_T$. However, as manufacturing can cause slight deviations in the period, the propagation-dependent visibility was measured to determine the optimal working distance. The measurement was conducted by increasing the distance from the TAI to the camera step-wise and recording the pattern at each position. Each TAI was mounted in a holder frame and the camera was placed at a starting distance of 40 mm from the TAI. The distance was increased step-wise and a total of four images were taken at each position. At a beam energy of 20 keV, three TAIs designed for this energy were measured. At 30 keV, a total of four TAIs were measured. Three designed for this energy, and as fourth, the 10 µm hexagonal TAI, designed for 20 keV. To ensure mechanical stability the air cushion of the camera axis was turned off at each image. The detailed parameters of each carpet scan are listed in Tab. 5.1.1.

The images were corrected for the camera dark-current and a 150 px × 150 px central area of each image was evaluated. For calculating the visibility, the standard deviation definition of visibility was used as in Eq. 3.1.5.

TAI Visibilities					
TAI	Design Energy	Beam Energy	Calculated Distance	Measured Distance	Peak Visibility
10 µm hexagonal	20 keV	20 keV	538 mm	540 mm	0.39
10 µm square	20 keV	20 keV	538 mm	590 mm	0.41
7 µm hexagonal	20 keV	20 keV	264 mm	290 mm	0.23
10 µm hexagonal	30 keV	30 keV	807 mm	850 mm	0.34
10 µm square	30 keV	30 keV	807 mm	740 mm	0.27
7 µm hexagonal	30 keV	30 keV	395 mm	415 mm	0.13
10 µm hexagonal	20 keV	30 keV	807 mm	890 mm	0.19

Table 5.1.2: Visibilities and working distances of the TAIs from Fig. 5.1.1 **a)** and **b)**.

The results are shown in Fig. 5.1.1. In **a)** visibilities at a beam energy of 20 keV are plotted. The vertical line in dark blue shows the calculated fractional Talbot distance of $1/6\,d_T$ for a period of 7 µm at $1/6\,d_T = 263.5$ mm, the cyan lines for a period of 10 µm at $1/6\,d_T = 537.7$ mm. In Fig. 5.1.1 **b)** the measurements at a beam energy of 30 keV are shown, again with the calculated distance for 7 µm at $1/6\,d_T = 395$ mm in light gray, and for 10 µm at $1/6\,d_T = 807$ mm in dark gray. The measured distances at peak visibilities are listed in Tab. 5.1.2.

Discussion From the plots can also be seen, that slight deviations from the optimal distance have only small effects on the pattern visibility. This implies also relaxed requirements for the setup alignment, as the distance from the grating to the detector can be chosen within a few centimeters of accuracy.

Furthermore, the scan of the 10 µm hexagonal TAI designed for 20 keV at a beam energy of 30 keV gives indications on the performance of the TAI at polychromatic sources and the requirements on longitudinal coherence. Compared to its design energy, the visibility is lower, and at an increased distance, even compared to the TAI designed for the energy. But given the low slope of the curve, sufficient visibility can be expected still, even when the incident energy spectrum covers a few keV.

In Fig. 5.1.1 **c)** the visibility map for a mean reference image of the first phase step for the scan of the sample in liquid shown in Sec. 5.2.4 is shown. For each pixel, the visibility in a 150 px × 150 px region around it was determined. The scan used a 10 µm hexagonal TAI designed for 30 keV at a beam energy of 30 keV. The visibility is not homogeneously, and

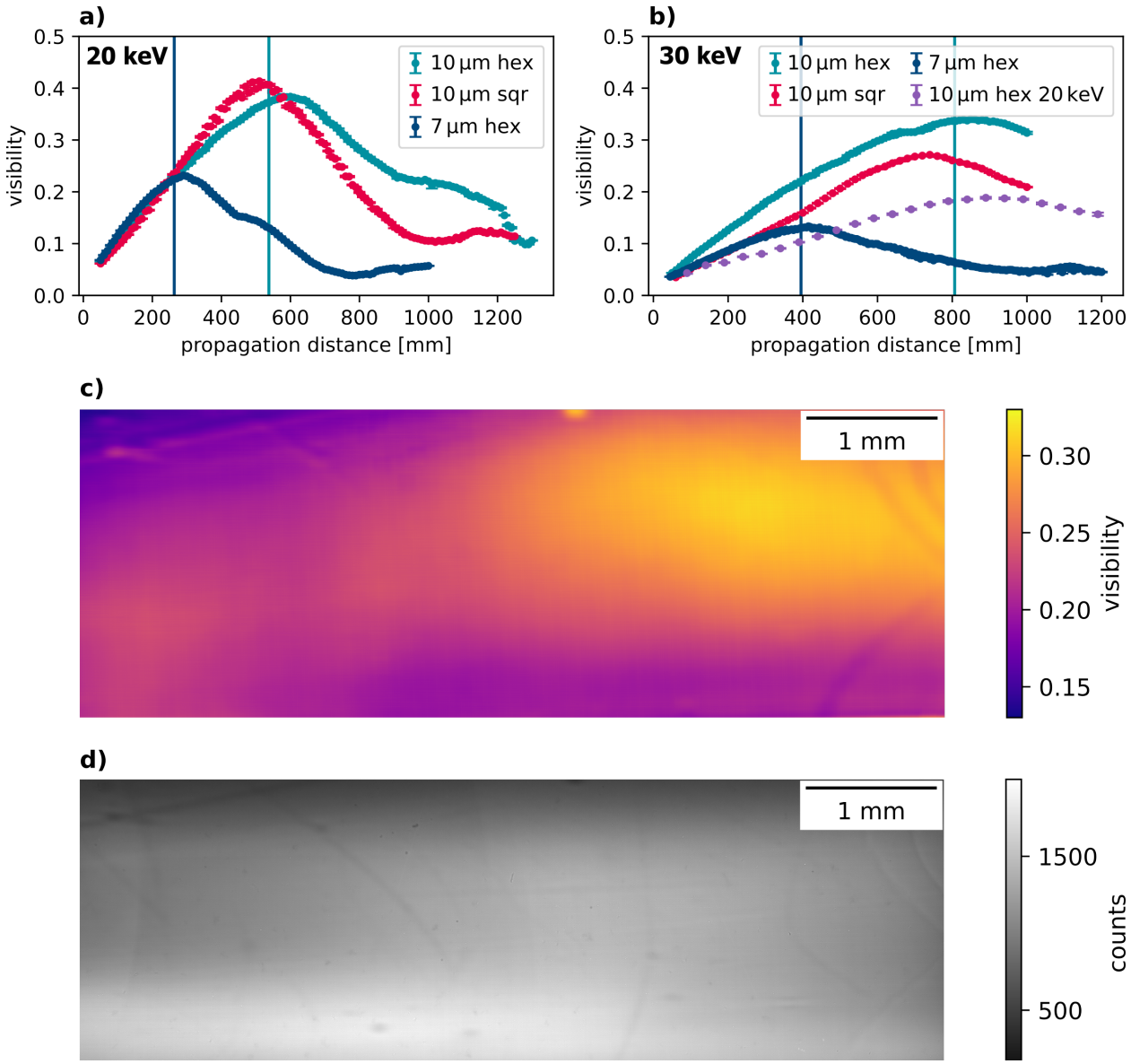

Figure 5.1.1: Visibility measurements of different TAIs used at the setup. In **a)** the propagation distance dependent visibility of the center of the image, using a standard deviation definition of visibility (c.f. Eq. 3.1.5) is plotted for three TAIs measured at an energy of 20 keV. In **b)** the same is plotted for 30 keV, where the purple points show a TAI designed for 20 keV and scanned at 30 keV. The dark blue vertical lines marks the calculated fractional Talbot distance for a period of 7 µm, the cyan lines for a period of 10 µm. In **c)** the visibility map for a tomographic scan using the 10 µm hexagonal TAI at 33 keV is shown. The map was calculated for a mean reference image from one of the scans presented in Sec. 5.2.4. In **d)** the beam profile for the map in **c)** is shown.

only slightly correlated to the intensity distribution of the beam profile shown in Fig.5.1.1 **d)**.
The measured visibility is also compared to sandpaper in Gustschin et al. [Gus+21]. While the absolute value of the measured visibility is similar, the different TAIs have the advantage of a smaller length scale on which the visibility occurs, the period. The visibility of sandpaper is more inhomogeneously distributed, while the TAIs obtain the visibility within one period. This allows for a more predictable stepping behavior and therefore, for using fewer wavefront marker positions.

Scan Setup The choice of which TAI is best suited for a tomographic scan, depends on several parameters: the beam energy, the used camera and effective pixel size, and the sample. The TAIs offer two degrees of freedom, the etching depth and the period length. As the hexagonal TAIs have a more dense structure and comparable visibility to the square lattice, they were used in most scans.
The etching depth of the TAI should be adapted to the beam energy. For high-energy scans, this aspect becomes less important, as the overall visibility declines with increasing energy. Small TAI periods are in general favorable, as they are less prone to artifacts in the images, but also reached lower peak visibilities, compared to larger periods. In Fig. 5.1.1 the peak visibility of the 7 µm TAI reaches at a beam energy of 20 keV similar values like the 10 µm TAIs at the same distance. At a beam energy of 30 keV, the visibility of the 7 µm TAI is lower than for larger structures.
For a beam energy of 20 keV, the shorter period of 7 µm was successfully used with all tested camera systems. For higher energies, the 10 µm period TAIs were used, although a direct comparison to a 7 µm TAI might be interesting. If strongly absorbing samples should be scanned, the larger visibilities of the 10 µm structures can be necessary for a successful phase-retrieval in the sample.
Even tough the TAIs have their peak visibility around the fractional Talbot distance, a deviation of this distance still produces a pattern with significant visibility. This allows for tuning the sensitivity, in most cases to lower values and less edge-enhancement, by selecting a shorter operation distance.

5.1.2 Angular Sensitivity

Definition of Sensitivity The sensitivity of a DPC setup can be defined as the noise in the background of a differential projection:

$$\sigma_{x/y} = STD(u_{x/y,BG}) \cdot \frac{p_{eff}}{d_{prop}}, \tag{5.1.1}$$

where p_{eff} describes the effective pixel size and d_{prop} the propagation distance from the sample to the detector. The sensitivity characterizes the ability of the setup to distinguish small differences in the refractive index decrement. For single-distance PBI no direct definition of sensitivity can be made, as the resulting contrast is only of qualitative nature. An indirect and non quantitative comparison of different phase-retrieval techniques can be made by comparing the resulting reconstructions and the feature visibility.

Optimizing the Sensitivity There are a number of influencing parameters to the sensitivity of a SBI and therefore for a TAI measurement. They are described in Eq. 3.2.5.
In this equation, the setup dependency is summarized in a constant. This setup constant is influenced by the beam properties. As the source size and divergence are different in the horizontal and vertical direction, described in Tab. 4.1.1, the sensitivity is also direction-dependent. In the vertical direction, the smaller dimensions of the source improve the sensitivity. The maximum sensitivity of the setup is also influenced by the stability of the beam, of the setup, and of the wavefront marker position.
During the development of the setup, several measures were taken to improve the mechanical stability. The largest effect was observed, when the motor, which is used to drive the sample out of the beam for the flat-field acquisition, was changed from moving the whole rotation stage, to the piezo on top of the rotation stage. The weight moved by the motors was drastically lowered by this change and previously observed pattern displacements and tilts were avoided.
The beam stability itself cannot be influenced at the beamline, but is rather dependent on electron orbit stability and the operation of the storage ring. Instabilities can occur during top-up, as the orbit can vary during the injection, and if the filling mode uses fewer bunches, the so-called timing mode. If the beam-current changes, the heat load on the monochromators can cause drifts of the beam position. During normal top-up operation, these beam current is filled up, if the current dropped 1%.

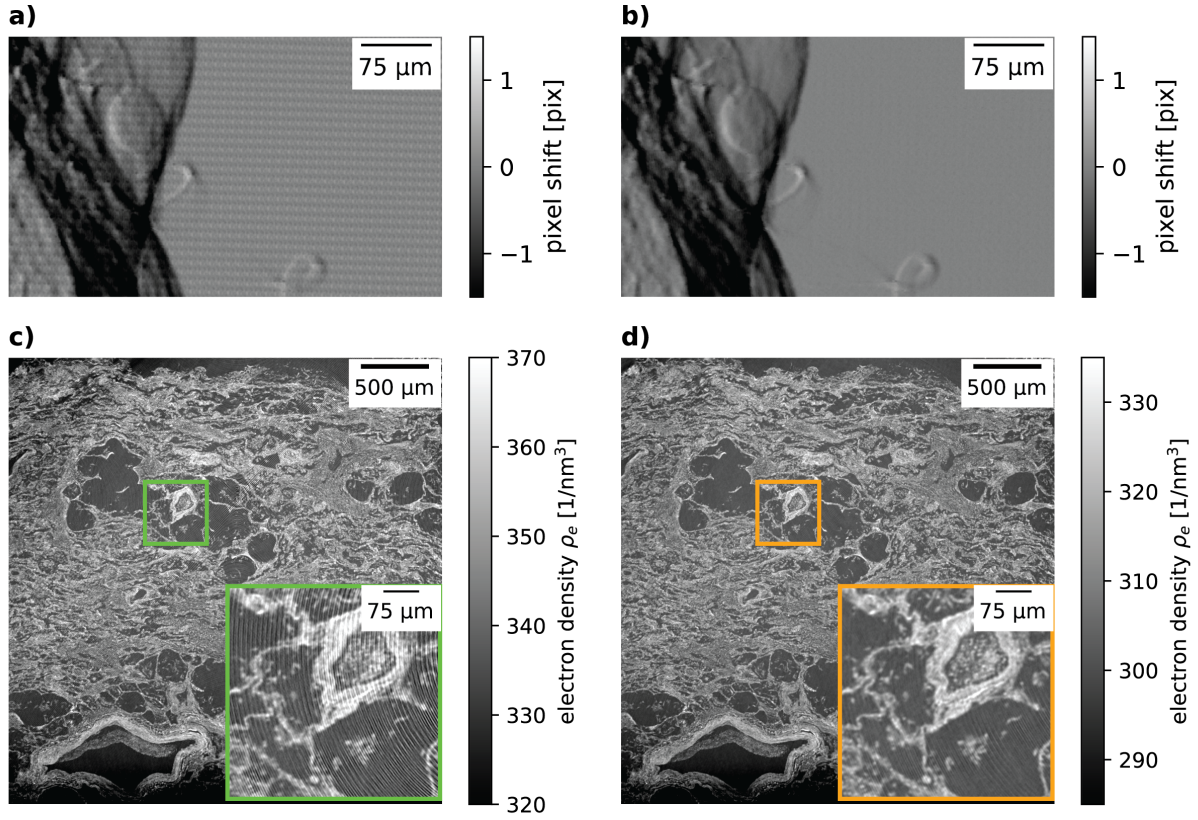

Figure 5.1.2: Effect of the dynamic flat-field correction. In **a)** a differential projection in the x-direction processed using mean reference images is shown. The sensitivity is 500 nrad. In **b)** the same projection is processed using a dynamic reference image. The sensitivity is now 268 nrad. In **c)** a scan of human lung tissue, where mean reference images were used is reconstructed. Compared to the dynamic reference images in **d)**, an offset in the electron density and more ring artifacts are visible.

During post-processing, some drifts are compensated to some extent with the dynamic flat-field correction. In Fig. 5.1.2 **a)** and **b)** phase retrieved projections using a mean reference image and dynamic references are compared at an UMPA window size of $w = 3$ and 16 phase-steps. The dynamic reference improves the sensitivity from 500 nrad to 268 nrad and removes the fixed pattern structure, by compensating for drifts of the TAI pattern. This has also effects on the reconstruction in **c)** and **d)** where a strong reduction of ring artifacts and an offset in reconstructed electron density is visible.

During measurement, the sensitivity can be tuned by the number of phase-steps recorded, while during phase-retrieval the UMPA window size can be tuned. The latter allows trading spatial resolution for improved sensitivity. In Fig. 5.1.3 **a)** the dependence on the phase-

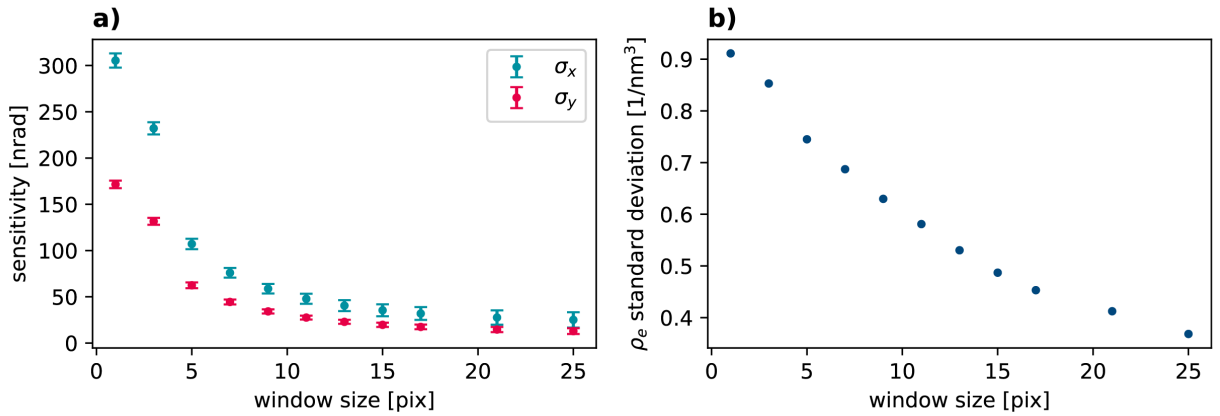

Figure 5.1.3: Analysis of the UMPA window size dependent sensitivity and electron density resolution. In **a)** the human lung tissue scan (cf. Sec. 5.2.2) was processed with increasing UMPA window sizes. The mean sensitivity in the x- and y-directions are plotted.

retrieval window size of a scan in x- and y-direction is analyzed. For this, the mean sensitivity during a scan is plotted, while the error bars mark the standard deviation. The expected $1/w$ behavior from Eq. 3.2.5 can be seen, as well as the differences from the source geometry. In Fig. 5.1.3 **b)** the scan was reconstructed and the noise in the homogeneous embedding material was measured in order to analyze electron density resolution. This also improves, with improved sensitivity.

Comparison to other Setups Comparing the achieved sensitivity to literature, the spatial resolution of each setup has to be taken into account. For a SBI setup at a synchrotron using UMPA, Zdora et al. report a sensitivity of $\sigma_x = (95 \pm 1)\,\mathrm{nrad}$ and $\sigma_y = (82 \pm 1)\,\mathrm{nrad}$ for a spatial resolution better than 8 µm [Zdo+20a]. This is comparable to the values achieved in this work, considering the 2-4 times better spatial resolution.
In laboratory-based setups, the used detector systems differ most of the time from the lens-coupled detector systems at synchrotron beamlines. Direct bonded or flat-panel detectors offer better light optical efficiency at a reduced spatial resolution, which is necessary as laboratory sources generate lower X-ray fluxes. For a setup using SBI and UMPA, sensitivities of $\sigma_x = (1.33 \pm 0.24)\,\mu\mathrm{rad}$ and $\sigma_7 = (1.30 \pm 0.17)\,\mu\mathrm{rad}$ have been reported with an effective pixel size of 3.25 µm and an upper limit of the spatial resolution at 14 µm [Zdo+20b]. Other techniques, GBI, using much larger effective pixel sizes of 100 µm can reach down to $\sigma = 38\,\mathrm{nrad}$.

Scan Parameters						
Sample	Photon Energy	Angular Steps	Exposure Time	Propagation Distance	Grating Period	Phase Steps
Human Kidney	20 keV	5000	200 ms	180 mm	7 µm	16

Table 5.1.3: Scan parameters of the kidney sample. The scan was recorded using the 10x magnification objective of the camera, resulting in an effective pixel size of 457 nm. The sample was placed 2500 pixels off axis. In addition, a 30 µm LuAG scintillator was used to improve the resolution of the detector.

5.1.3 Spatial Resolution

Spatial Resolution Measurement The spatial resolution of a phase-retrieved scan depends on a variety of parameters, as discussed in Sec. 3.4. In order to get an estimate of the maximum capabilities of the setup, a measurement of a human kidney sample was optimized to reach a high spatial resolution. For this, the 10 fold magnification objective of the detector was used, resulting in an effective pixel size of 457 nm. As this also results in a smaller FOV, the sample was mounted with a 2500 px shifted center of rotation for an off-axis scan. The camera scintillator was changed to a thin 30 µm LuAG screen and the exposure time was set to 200 ms. Additional parameters are listed in Tab. 5.1.3. For the phase-retrieval of the scan an UMPA window of w =3 px was used and opposing projections were stitched before integration.

The resolution of the projection images is analyzed in Fig. 5.1.4. In **a)** and **b)** the integrated phase and the UMPA transmission are shown. The resolution of the indicated square area was determined using FRC in **c)** and **d)**. The integrated phase image shows a full-bit resolution of 2.40 µm and a half-bit resolution of 2.13 µm, the transmission image of 2.96 µm at full-bit, and 2.39 µm at half-bit. Compared to the spatial resolution limit of the setup, which can get down to 1 µm, the resolution in a DPC projection is similar.
The scan was reconstructed and analyzed for its edge sharpness and FRC in Fig. 5.1.5. In **a)** central part of a slice of the kidney is shown. This part was analyzed using FRC in **b)**, resulting in a full-bit resolution of 2.32 µm and a half-bit resolution of 2.07 µm. The edge indicated by the red line in **a)** was fitted using an error function in **c)**. This gives a FWHM of the associated Gaussian of FWHM=3.30 µm. This corresponds well with the resolution in projection and the setup limits.

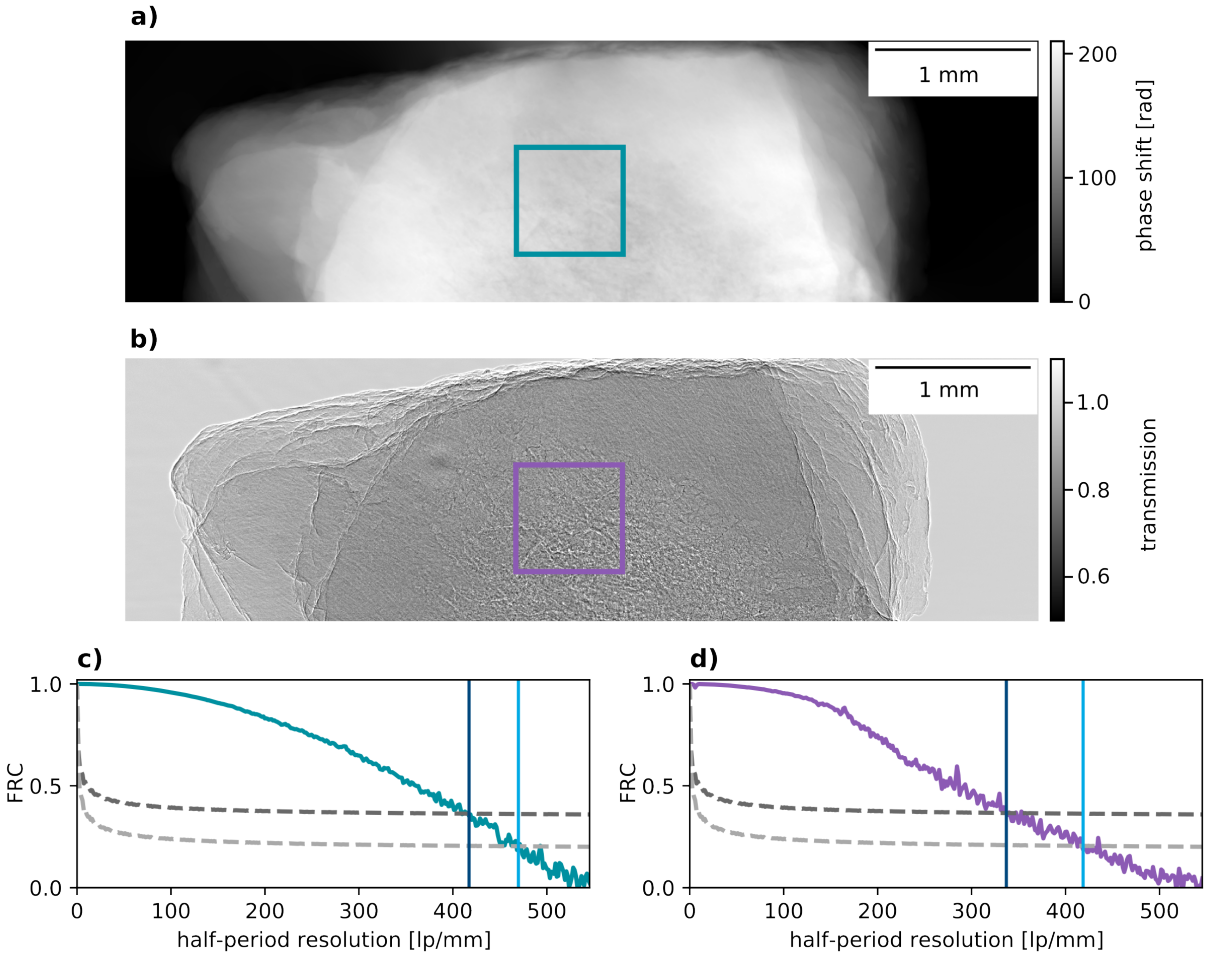

Figure 5.1.4: Analysis of the spatial resolution in projection. In **a)** a projection of the integrated phase of the high-resolution kidney scan is shown, in **b)** the UMPA transmission. The colored boxes mark the area used for FRC analysis in **c)** and **d)**. The integrated phase FRC results in a full-bit resolution of 2.40 µm and a half-bit resolution of 2.13 µm. The transmission signal yields 2.96 µm at a full-bit, and 2.39 µm at a half-bit criterion.

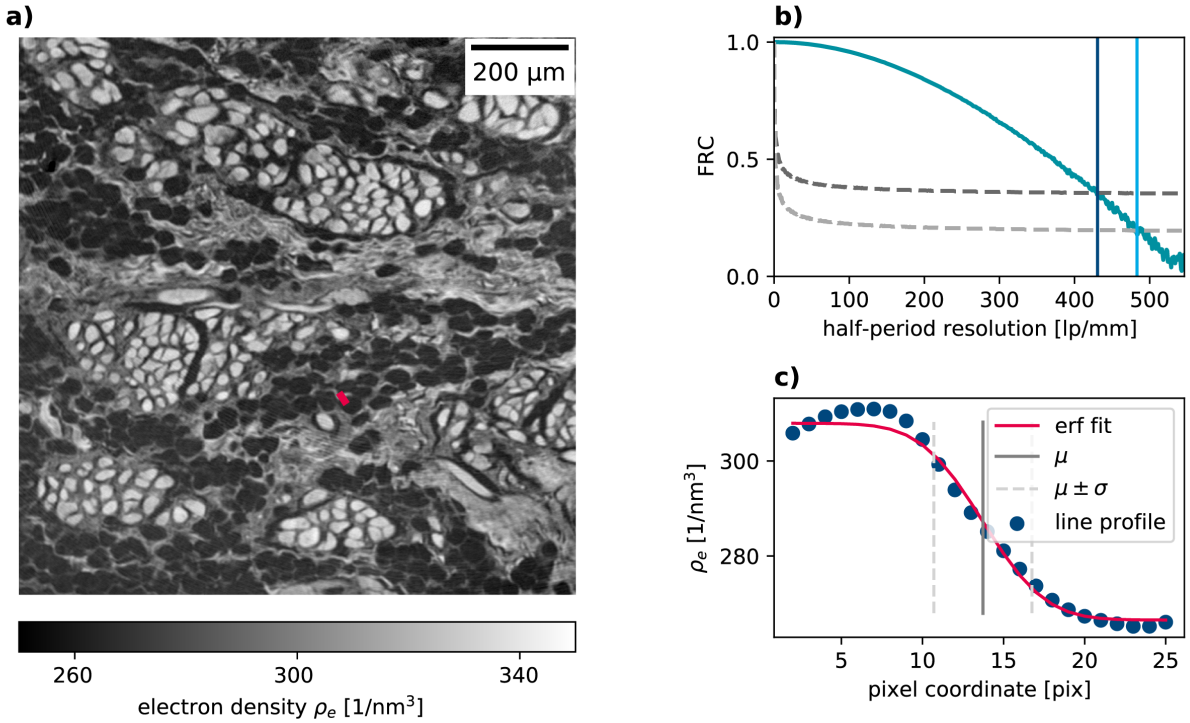

Figure 5.1.5: High-resolution scan of human kidney tissue. The scan parameters are listed in Tab. 5.1.3 Phase-retrieval was computed, using an UMPA window size of 3 pixels. In **a)** an section of a slice is shown. In **b)** the FRC is analyzed, resulting in a full-bit resolution of 2.32 µm and a half-bit resolution of 2.07 µm. In **c)** the line profile of the line indicated in red in **a)** is analyzed. A Gaussian error function is fitted to the edge, and the FWHM is taken as the resolution criterion. The indicated line shows a FWHM of $2\sqrt{2\log(2)}\sigma$=3.30 µm.

Further Optimization Possibilities Additional influences on the spatial resolution might be connected to the beam energy, the TAI period, and the setup geometry. Even further optimization of the resolution would require systematic investigations of the influence of the camera setting as well. By tuning the camera aperture to lower openings, additional gains might be possible. Furthermore, an optical filter for visible light could be installed behind the scintillator to compensate for chromatic effects in the microscope. As all this reduces the total amount of light, which reaches the camera, the measurement time would be increased even further. Therefore this is only feasible to a limited extent.

5.1.4 Quantitative Measurements

The advantage of the TAI setup over the more common PBI phase-retrieval, is its direct measurement of the phase-shift, without any assumption about the sample properties. This enables quantitative phase-contrast scans, which then have a variety of advantages for further analysis. However, even if the method itself does not require prior knowledge of the sample, the scan settings and simplifications in the UMPA model can still lead to errors in the measured values. Therefore, a test of the quantitative accuracy was carried out.
For testing the quantitative phase-contrast aspect of the setup, an existing material phantom was used. The phantom was made of five polymer rods of known compositions and densities. It included PMMA, Nylon-6, and Nylon-6,6, as well as PTFE and PCTFE. The material rods were supplied from Goodfellow GmbH (Hamburg, Germany). The compositions and densities were taken from the material datasheets. The expected refractive index decrements were calculated using the data sets by Henke et al. [HGD93] and converted to electron density values.
In the following, two scans of the phantom are compared. The first uses a longer propagation distance from the sample to the detector of 300 mm, while the second uses a shorter distance of 150 mm. This allows for comparing the effects of different phase sensitivities, as well as the influence of edge-enhancement.

Long Propagation Distance Measurement

The parameters of the scan with a longer propagation distance are listed in Tab. 5.1.4. The projections were phase-retrieved using an UMPA window size of $w = 3\,\mathrm{px}$. As the spatial

Scan Parameters						
Sample	Photon Energy	Angular Steps	Exposure Time	Propagation Distance	Grating Period	Phase Steps
Material Phantom	20 keV	2001	100 ms	300 mm	10 µm	16

Table 5.1.4: Scan parameters of the material phantom at a long propagation distance. An exemplary slice is shown in Fig. 5.1.6 **a)**.

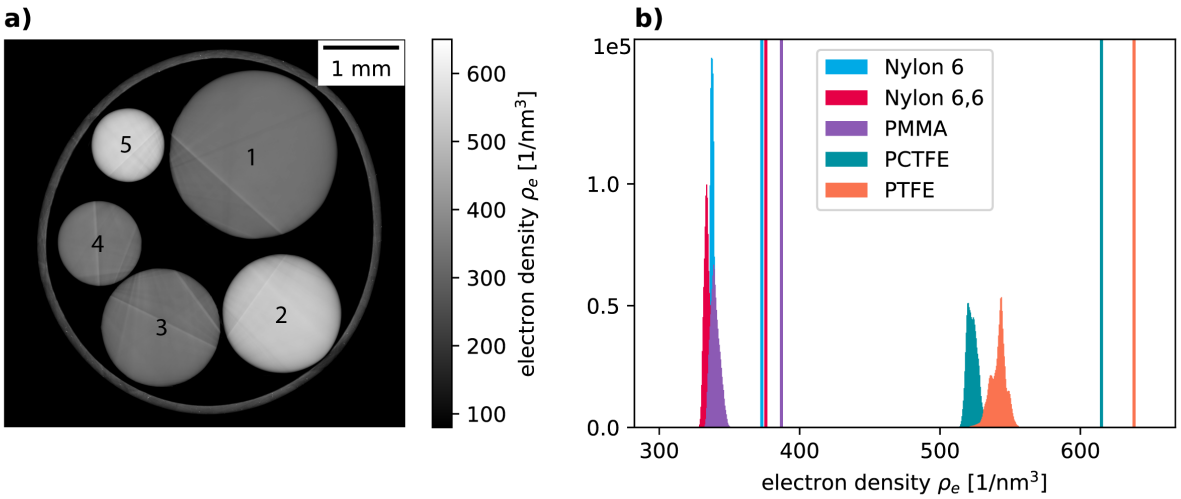

Figure 5.1.6: Scan of the material phantom with a long propagation distance. In **a)** an exemplary slice is shown. The materials are in the following order: 1-Nylon 6, 2-PCTFE, 3-Nylon 6,6, 4-PMMA, 5-PTFE. For the histogram analysis in **b)** a region of 100 px × 100 px × 100 px was taken out of every material. The vertical lines show the literature values for each material. The scan parameters are listed in Tab. 5.1.4.

resolution was not of interest, a two-pixel binning was applied and the scan was reconstructed using a Shepp-Logan filter.

The mean sensitivity of the differential projections was at σ_x=196 nrad and σ_y=123 nrad. A reconstructed slice of the scan is shown in Fig. 5.1.6 **a)**, where the materials of each rod are indicated. For each material, a region of 100 px × 100 px × 100 px was used to determine the histogram. These results are shown in **b)**. The mean values for each phantom are listed in Tab. 5.1.6.

Scan Parameters						
Sample	Photon Energy	Angular Steps	Exposure Time	Propagation Distance	Grating Period	Phase Steps
Material Phantom	20 keV	2001	100 ms	150 mm	6.8 µm	16

Table 5.1.5: Scan parameters of the material phantom at a short propagation distance. An exemplary slice is shown in Fig. 5.1.7 **a)**.

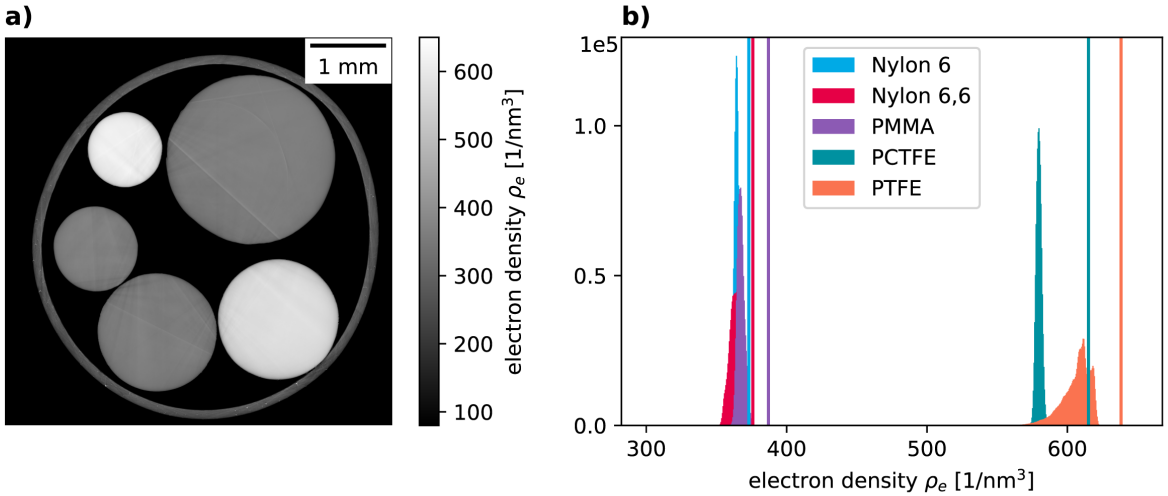

Figure 5.1.7: Scan of the material phantom with a short propagation distance. In **a)** an exemplary slice is shown. For the histogram analysis in **b)** a region of 100 px × 100 px × 100 px was taken out of every material. The vertical lines show the literature values for each material. The scan parameters are listed in Tab. 5.1.5.

Short Propagation Distance Measurement

The parameters of the scan with a shorter propagation distance are listed in Tab. 5.1.5. For post-processing, the same parameters as for the long propagation distance were used.

The mean sensitivity of the differential projections was at σ_x=906 nrad and σ_y=284 nrad. The sample was evaluated with the same settings as for the longer propagation distance, and the results are shown in Fig. 5.1.7 and listed in Tab. 5.1.6.

Quantitative Comparison					
Material	Expected Electron Density	Long Distance Scan	Error	Short Distance Scan	Error
Units	$1/\mathrm{nm}^3$	$1/\mathrm{nm}^3$	%	$1/\mathrm{nm}^3$	%
Nylon 6	373.1	(337.6 ± 1.1)	9.5	(364.0 ± 1.7)	2.4
Nylon 6,6	376.0	(334.1 ± 2.1)	11.1	(363.5 ± 4.0)	3.3
PMMA	387.0	(339.8 ± 3.2)	12.2	(367.4 ± 2.5)	5.0
PCTFE	615.0	(523.2 ± 3.9)	14.9	(579.7 ± 1.9)	5.7
PTFE	638.2	(541.6 ± 5.5)	9.5	(606.3 ± 10.1)	5.0

Table 5.1.6: Quantitative comparison of the electron density values of both scans to the expected values. For each material the mean and the standard deviation of a Region of Interest (ROI) of $100\,\mathrm{px} \times 100\,\mathrm{px} \times 100\,\mathrm{px}$ was used. The errors give the deviation from the expected values.

Quantitative Values

For comparing the measured electron density to the one expected from the material composition, the mean and the standard deviation of the $100\,\mathrm{px} \times 100\,\mathrm{px} \times 100\,\mathrm{px}$ region of each material were evaluated.

Influence of the Propagation Distance Compared to PBI with a homogeneous material assumption, the setup is able to quantitatively reconstruct the electron density of the materials in the phantom. However, both scans show a large difference in the reconstructed electron density values. The scan with the longer propagation distance underestimates the electron density values with errors of 9.6 to 14.9 %, significantly larger than the scan with a shorter propagation distance, which shows errors from 2.4 to 5.7 %. Both measurements underestimate the electron density compared to the expected values.

The large difference in reconstructed electron density values between the propagation distances can mainly be attributed to stronger edge-enhancement effects at a longer propagation distance. As UMPA only includes first-order phase effects, edge-enhancement cannot be modeled. This leads to errors at the edges of e.g. the polymer rods, where the differential phase is not tracked properly. As consequence, the phase-shift at the edges is underestimated, which affects the whole sample after integration. This effect has also been studied in the Master's thesis of Lev Ushakov [Ush21].
The types of Nylon cannot be separated in both scans, even though the standard deviation

in each material is lower than the difference in electron density, with an exception of Nylon 6,6 in the short-distance scan. This might be influenced by several factors, which apply to all used polymer rods. For one, the used materials have been scanned many times. While in the evaluated volume no cracks were visible, other areas of the sample showed signs of degradation. Therefore, the theoretical values might not be applicable anymore, as e.g. swelling of the material can change the density. The second effect to consider is the air humidity. Polymers can absorb water, dependent on their material composition. This changes the electron density of the material and can as consequence lead to deviations from the expected values. Both effects will pose an unknown error to the measurements.

Implications for Future Scans From these measurements, a few general rules for planning future scans were derived. The phase-shift of a sample is underestimated during a scan. The exact degree of the error is dependent on the amount of edge-enhancement in the sample. This can be influenced by the setup geometry and photon energy. Shorter propagation distance, as well as higher photon energies, are advantageous. However, both properties have a negative influence on the setup sensitivity.

5.2 Applications of the Setup

While the previous sections described the characterization of the setup design and its properties, this section will focus on scans measured with this setup. During the scope of this thesis, the setup was applied to a broad range of samples on multiple beamtimes. Some exemplary scans are shown in the following. Each of the highlighted measurements will focus on a specific question or task.
The first application of the setup on a stained mouse kidney covers the limitations of PBI and potential advantages of quantitative methods. The next measurement series on human COVID-19 samples were used to study sample preparation and the spatial resolution of the method. The scan of a sandstone sample at the beamline P07 was the first implementation for high-energy scans with this setup. And the fourth application of the setup to mouse lymph nodes marks the transition of the setup to a user experiment.

5.2.1 Stained Mouse Kidney

In order to study the capabilities of the setup when scanning stained tissue and to explore the advantages over PBI a bismuth-stained mouse kidney was measured. Parts of this results have been presented and published in Riedel et al. [Rie+21] with a focus on the general image quality, and published in Riedel et al. [Rie+23] with a foucus on the comparison to PBI.

Sample Preparation For the mouse kidney sample, the animal housing and organ removal was carried out at the Klinikum rechts der Isar, Technical University of Munich, Munich, Germany following the European Union guidelines 2010/63 and with approval from an internal animal protection committee of the Center for Preclinical Research of Klinikum rechts der Isar, Munich, Germany (internal reference number 4-005-09). After removal, the sample was fixated in a formaldehyde solution and stained with a bismuth-oxo-cluster [And+12]. After a dehydration series, the stained sample was embedded in paraffin wax and mounted for scanning.

Scanning and Data Processing The sample was scanned with the parameters listed in Tab. 5.2.1. The DPC image using the TAI setup, was processed using an UMPA window size of 3 px. In order to compare the same scan to PBI the average of all phase steps was

Scan Parameters						
Sample	Photon Energy	Angular Steps	Exposure Time	Propagation Distance	Grating Period	Phase Steps
Bismuth-stained mouse kidney	20 keV	2001	80 ms	160 mm	10 µm	16

Table 5.2.1: Scan parameters of the bismuth-stained mouse kidney.

taken per projection. With this, the TAI pattern is smoothed, and the illumination is homogeneous. By doing the same for the reference images, one can calculate a flat-field corrected image. These projections were subsequently phase-retrieved using a regularized phase-retrieval bases on the transport of intensity equation, assuming a homogeneous material. The regularization strength was determined by visual impression, at a level where no more edge enhancement was visible.

Scan Analysis An overview of the details of the quantitative TAI scan is shown in Fig. 5.2.1. The image was slightly sharpened, using an unsharp masking filter, to improve visual appearance. In the overview in **a)** different regions of a kidney can be identified. On the left verge, the renal cortex (COR) can be identified. With a slightly lower electron density and a visible structural difference, the outer shell of the outer medulla (OSOM) is in the center of the image. On the right side, a part of the papilla (PP) can be seen. The colored boxes are shown in **b)** and **c)**, showing details of blood vessels, down to the glomeruli structures in the cortex. In **c)** the transition from cortex to OSOM is indicated by blue arrows.

In Fig. 5.2.2 both phase-retrieval methods are shown in direct comparison. The PBI phase-retrieval shows strong artifacts towards the edges of the sample, as well as in the areas where stain aggregated. Zooming in, the structures in the PBI image are more inhomogeneous and blurred, compared to the quantitative scan using the TAI.
In Fig. 5.2.3 the images of Fig. 5.2.2 are analyzed for their histogram. The histograms were calculated with 200 bins in the shown windows and were fitted, using the sum of three Gaussian peaks. The green curve shows the histogram, and the red dashed line the fit. The individual Gaussian peaks are plotted below the line. The peaks can be attributed to different regions inside the kidney, where the gray peak corresponds to the embedding wax,

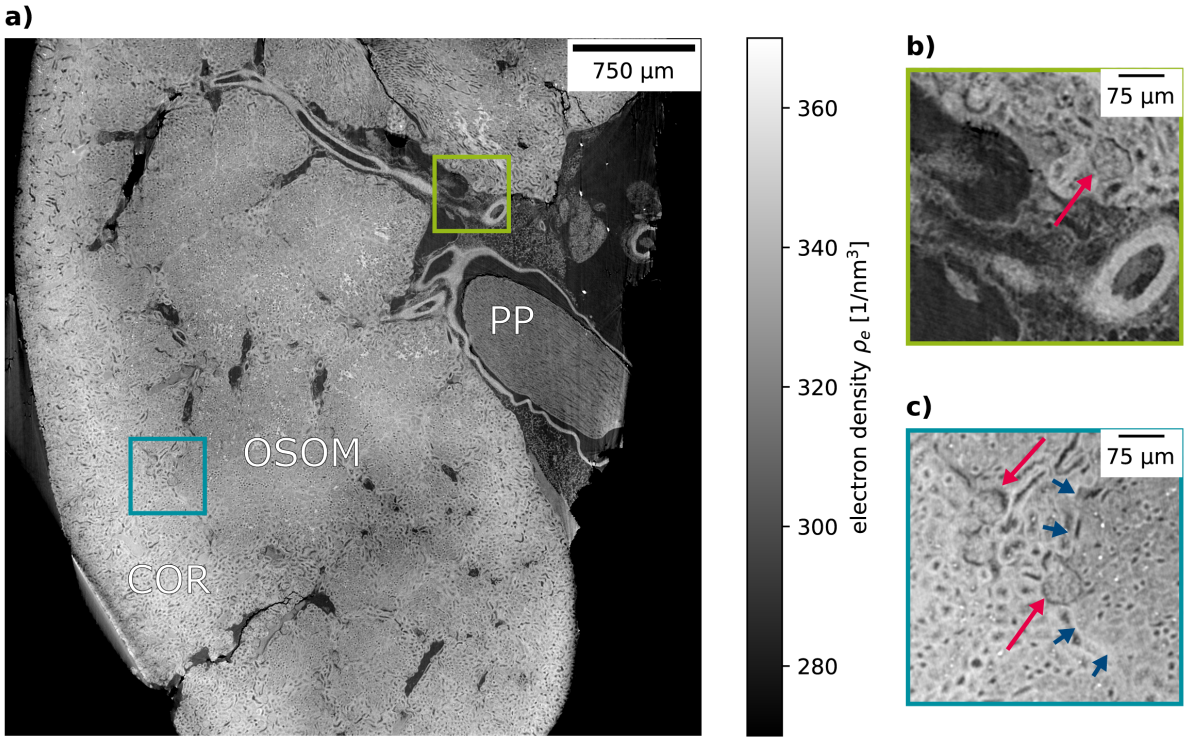

Figure 5.2.1: Overview of the Bi stained mouse kidney in **a)** scanned using the TAIs. For improved visual appearance, the scan was sharpened slightly. The different regions of the kidney can be identified. At the border of the sample, the Cortex (**COR**) with the glomeruli, in the middle the outer shell of the outer medulla (**OSOM**), and on the right a part of the papilla (**PP**). The zoom-ins in **b)** and **c)** show the details, down to the level individual glomeruli, as indicated by the red arrows. The blue arrows in **c)** highlight the transition from the Cortex to the Outer Shell of the Outer Medulla, where a structural change, as well as a slight change in electron density is visible. The scan was phase retrieved using an UMPA window of 3 pixel × 3 pixel. Figure modified from [Rie+21].

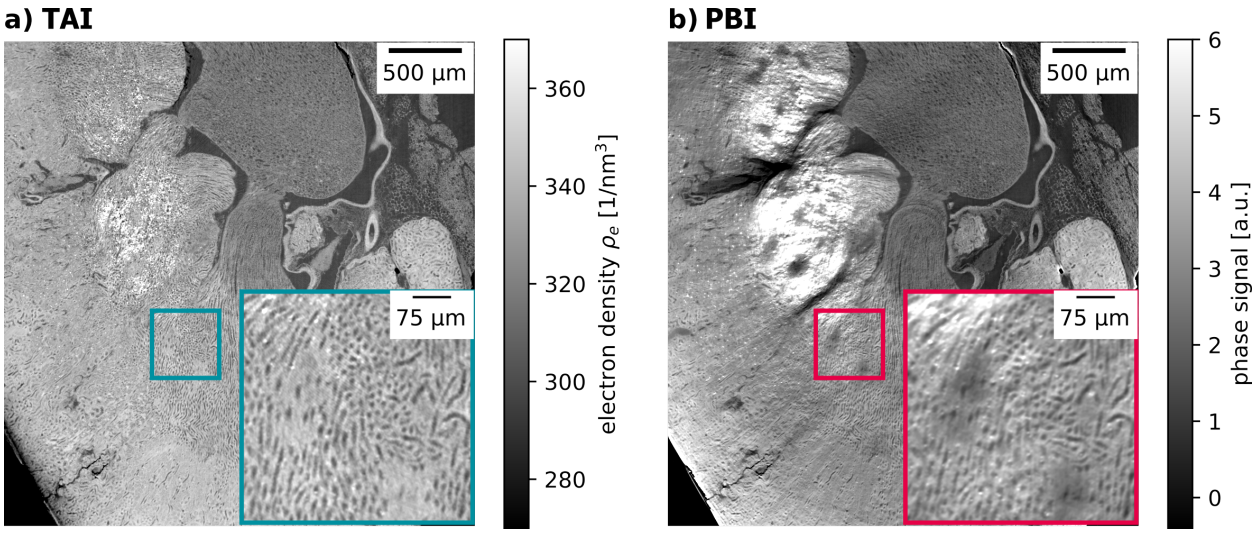

Figure 5.2.2: Comparison of the TAI based scan to PBI scan of the Bi stained mouse kidney. Zoom-ins show a part of the outer medulla. The PBI phase-retrieval in plot **b)** shows strong artifacts where the stain aggregated in the center, as well as towards the edges of the sample. In contrast, the phase-retrieval from the TAI data in **a)** shows only a slight increase in electron density in the affected areas, but no artifacts. The difference between the techniques can also be sees in the zoom-ins, where the TAI scan provides a much more homogeneous image than the PBI scan. Figure modified from [Rie+23].

the light green to the medulla part, and the darker green peak to the cortex region.

Discussion In this comparison, the effects of the assumption of a single material and its limitations become visible. Due to the staining properties, the absorption is not homogeneously increased. This poses no problem for a quantitative imaging method using the TAI but causes artifacts in single-distance PBI as the assumption of a single material is not fulfilled. Problems with these artifacts might arise when further data analysis with segmentation tries to identify the materials.

The analysis of the histogram highlights these findings. Comparing the TAI image, to the PBI image, the peaks of the medulla and the cortex are different. In the PBI image, the cortex is far wider and reaching to values outside the histogram, due to the artifacts at the areas with high stain deposition, as well as due to general gradients. The overall fit of the PBI histogram using a sum of three Gaussians, works not as well, as for the TAI scan.

As the choice of a PBI regularization strength has an influence on the amount of blurring, the correct choice of parameter is not uniquely defined. If only structural information is of interest, a certain degree of under-regularization, and therefore edge-enhancement, can be accepted. On the other hand, this means a loss of contrast from the phase information. The

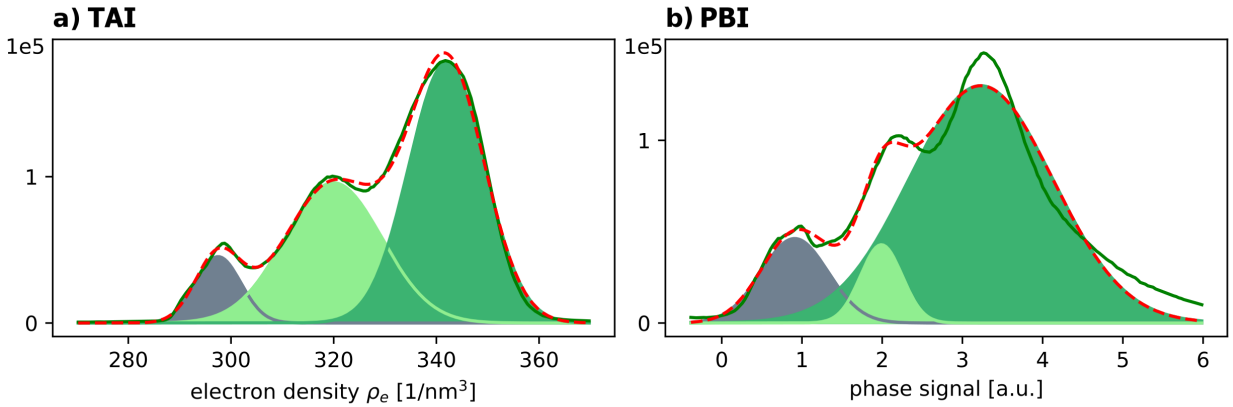

Figure 5.2.3: Comparison of the histograms of the scans in Fig. 5.2.2, the TAI scan in **a)** and the PBI scan in **b)**. The green line shows the histogram calculated with 200 bins in the shown window. The red dashed line corresponds to a fit of the histogram using the sum of three Gaussian peaks, which are shown underneath. The peaks correspond to different materials in the scan, from left to right, the gray peak corresponds to the embedding wax, the light green to the medulla, and the darker green to the cortex. Figure modified from [Rie+23].

here presented images are phase-retrieved to keep the full contrast from the phase.

5.2.2 Human COVID Samples

For an ongoing project of scanning samples from fatal COVID-19 cases, we collaborate with the institute of forensic medicine of the Ludwig-Maximilians Universität, Munich, Germany. The samples are taken as an exhibit of a pathological investigation after COVID-19 fatalities. The here presented results are divided into two parts. The first part will concentrate on general results and the achieved image quality, without further analysis of technical or pathological details. The second part will focus on one sample in particular and uses this sample to analyze the technical properties of the setup and the phase-retrieval process. The analysis of the phase-retrieval methods was published in Riedel et al. [Rie+23].

Sample Preparation The human COVID-19 samples were taken as an exhibit of a forensics investigation after a COVID-19 fatality by the institute of forensic medicine of the Ludwig-Maximilians Universität, Munich, Germany. The Ethics Committee of the Ludwig-Maximilians Universität, medical faculty, stated that due to the forensic nature of the sample taken and examined on behalf of public prosecutors or investigating authorities, no obligation to seek advice form the Ethics Committee was given in case of scientifically publishing anonymized results (internal reference number 22-0572 KB). Due to the nature of the taking of the samples, not patient consent was necessary.
From each patient, samples from five organs were taken: kidney, liver, lung, heart, and brain. For some patients, staining the samples was tested. From each organ, a piece was stained, using a modified Eosin stain [Bus+18] and another piece using a modified Haematein stain [Mül+18], increasing the absorption of the cell cytoplasm and the cell nuclei. For each sample, an unstained counterpart was prepared as well. The samples were embedded in paraffin wax. In the following two exemplary samples are shown, kidney tissue and heart tissue.

Scan Parameters

Sample	Photon Energy	Angular Steps	Exposure Time	Propagation Distance	Grating Period	Phase Steps
Human COVID Kidney Eosin	20 keV	2001	100 ms	120 mm	10 µm	16
Human COVID Heart Eosin	20 keV	2001	100 ms	120 mm	10 µm	16

Table 5.2.2: Scan parameters of the stained COVID samples.

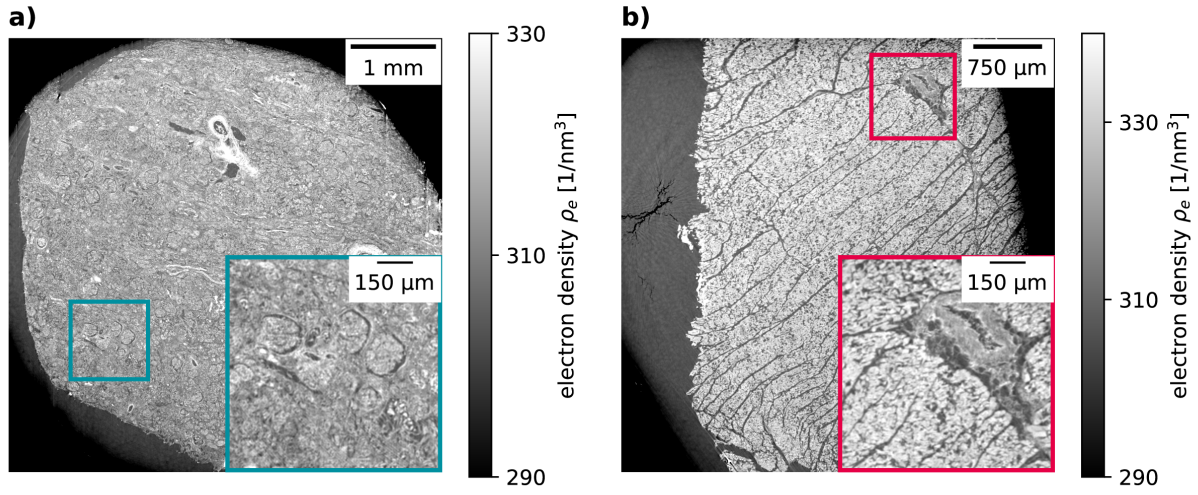

Figure 5.2.4: Scan of tissue samples for COVID-19 fatalities. The samples were stained with Eosin and embedded in paraffin. In **a)**, the human kidney tissue sample is shown. The zoom-in shows some glomeruli. In **b)**, heart muscle tissue is shown, with details of a blood vessel.

Scanning and Data Processing The datasets for this project were recorded in multiple beamtimes. As the setup parameters are not exactly the same each time, e.g. as the beam-stability changes, the scans were optimized for quickly visualizing the sample structure. The scan parameters are listed in Tab. 5.2.2. Noteworthy is the low number of angular steps, which were reduced in order to reduce the scan time.
After scanning, phase-retrieval was carried out using an UMPA window size of $w = 3\,\text{px}$ and reconstructed using FBP and a Shepp-Logan filter.

Scan Analysis Exemplary slices of the scans are shown in Fig. 5.2.4. In **a)** the kidney tissue is shown. A zoom-in reveals details of the glomeruli. In **b)** the heart tissue is depicted. The muscular cells, as well as blood vessels, can be identified.
Further analysis of the scan is still pending, as the project is ongoing.

Comparison to PBI

In addition to the two scans shown above, one sample was investigated further. For a piece of unstained lung tissue, the scan was phase-retrieved using multiple UMPA window sizes and compared to PBI phase-retrieval with multiple settings.

Scan Parameters						
Sample	Photon Energy	Angular Steps	Exposure Time	Propagation Distance	Grating Period	Phase Steps
Human COVID Lung	20 keV	4001	110 ms	180 mm	10 µm	16

Table 5.2.3: Scan parameters of the unstained lung tissue.

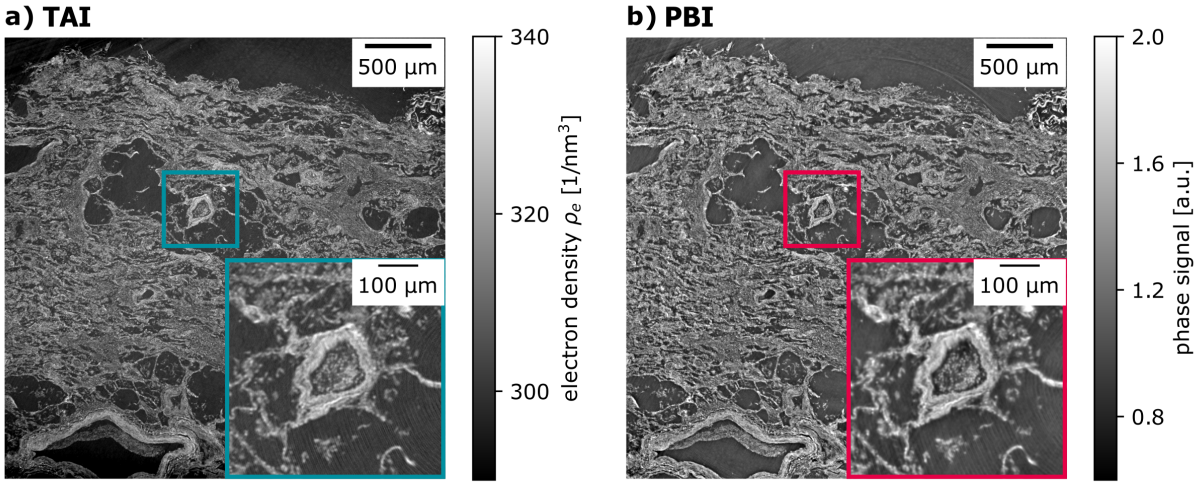

Figure 5.2.5: Comparison of the human lung tissue scan, phase retrieved using the TAI with UMPA in **a)** and a regularized PBI phase-retrieval in **b)**. For the UMPA phase-retrieval, a window of 3 pixels × 3 pixels was used. The PBI images were calculated by averaging over all phase steps, thus removing the grating pattern. The zoom-ins show details in a blood vessel. Figure modified from [Rie+23].

Data Processing The parameters of the scan are listed in Tab. 5.2.3. Phase-retrieval with UMPA was calculated for window sizes from 1 to 17. PBI phase-retrieval was calculated for regularization parameters of 0.5, and from 1 to 3 in steps of 0.2.

A reconstructed slice with both methods is shown in Fig. 5.2.5. In **a)**, an overview of the lung sample is shown, using a 3 px × 3 px UMPA window. In the zoom-in, details of blood vessels, with clotted blood in them, can be seen. The same slice, phase retrieved with a regularization parameter of 2.4, is shown in **b)**. The regularization strength was determined by comparing different parameters at which point edge-enhancement was successfully removed, and where blurring was not yet dominant. The parameter of 2.4 marks a compromise between sufficient regularization strength and not yet dominant blurring.
A 7 px × 7 px section of the vessel, was used to determine the Contrast-to-Noise Ratio (CNR)

to the embedding material. For the TAI scan, this was at $\mathrm{CNR}_{TAI} = 18.7$, and for the PBI scan at $\mathrm{CNR}_{PBI} = 23.1$.

Resolution Analysis Both retrieval methods were analyzed for the spatial resolution in the scan. Two methods for determining the resolution were used, edge sharpness and FRC. The results are shown in Fig. 5.2.6. In **a)** the edge sharpness dependent on the UMPA window size is plotted. This analysis used five sharp edges in the sample. In **b)**, the same edges are evaluated in the PBI phase-retrieved image, for different regularization strengths. The gray lines in **a)** and **b)** mark the parameters used for Fig. 5.2.5. In **c)** and **d)**, the images from Fig. 5.2.5 are evaluated using FRC.
The edge sharpness for the UMPA phase-retrieved scan shows for windows larger than $w = 3\,\mathrm{px}$ a dependency of the resolution on the UMPA window size as expected. For a window size of $w = 1\,\mathrm{px}$, the sharpness remains on the same level as for $w = 3\,\mathrm{px}$. This indicates that other factors than the phase-retrieval are limiting the resolution, e.g. the detector sharpness. For the PBI phase-retrieval, the edge sharpness depends on the regularization strength. With increasing regularization, increased blurring can be seen. However, measuring the edge sharpness has only limited applicability to under-regularized images, as edge-enhancement is sharpening edges and as consequence, the resolution is overestimated. For sufficient regularization strength, the edge-enhancement is removed, and thus the sharpness can be measured.
For the parameters used in Fig. 5.2.5 an edge sharpness resolution of $4.01 \pm 0.69\,\mu\mathrm{m}$ for the TAI scan with an UMPA window of $w = 3\,\mathrm{px}$ and $4.65 \pm 0.60\,\mu\mathrm{m}$ for the PBI scan with a regularization of 2.4. Both phase-retrieval methods are showing very similar results.
Using the FRC, the TAI scan was at $4.75\,\mu\mathrm{m}$ at a full-bit resolution criterion and $4.35\,\mu\mathrm{m}$ half-bit respectively. The PBI scan was at $4.70\,\mu\mathrm{m}$ full-bit and $4.15\,\mu\mathrm{m}$ half-bit resolution.

Discussion A direct comparison of the TAI scan to PBI shows similar results for both phase-retrieval methods. The visual appearance is comparable, with a similar level of detail. The measurable resolution is with both used methods close to each other.
The focus of the previously shown comparison was using the same dataset for both methods. It has to be noted, that this marks not an optimized PBI scan. If measurement parameters, such as propagation distance and energy are optimized, and the TAI is removed from the illumination, the results for PBI might improve. However, if it is taken into account, that the detector was not optimized for achieving the full possible resolution, the results are close

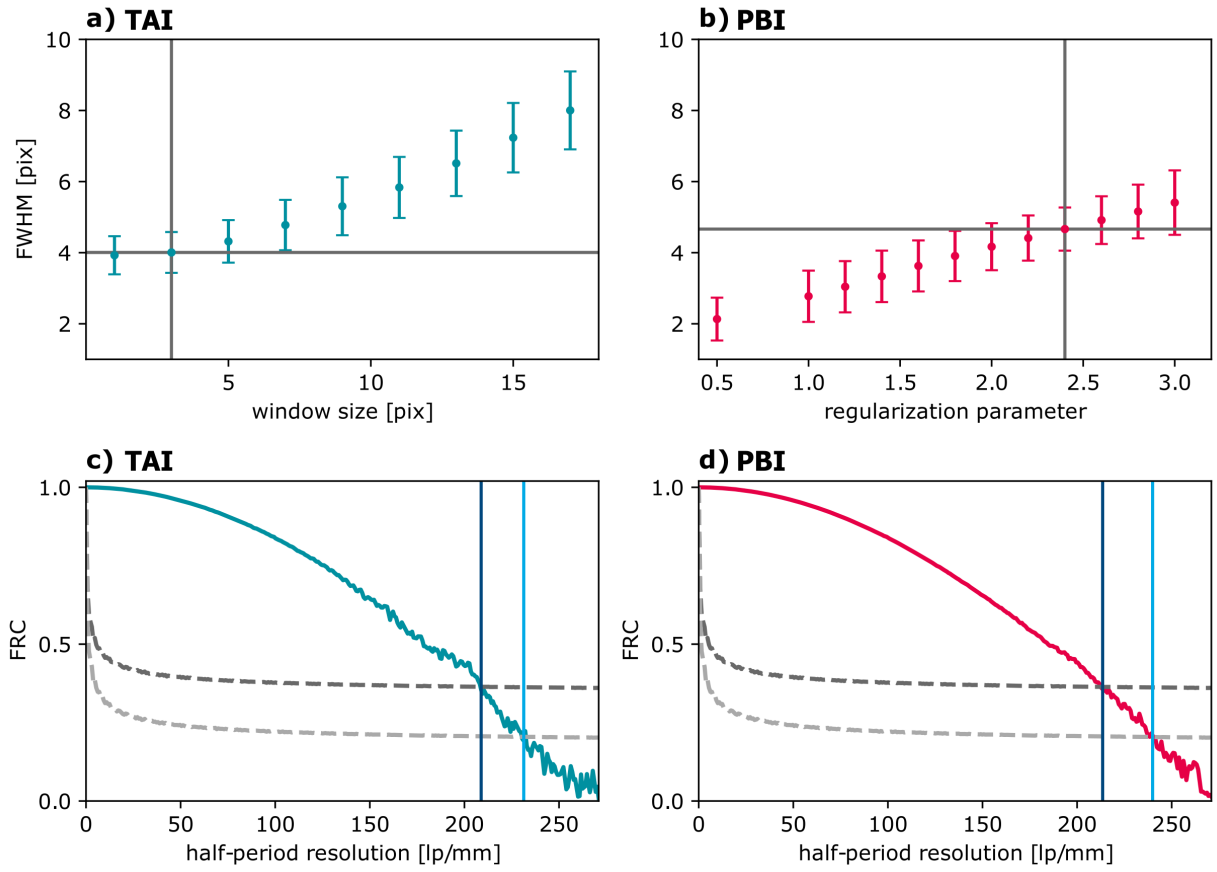

Figure 5.2.6: Analysis of the resolution of the lung tissue scan. In **a)** and **b)** the edge sharpness of edges in the images are analyzed. On the left in **a)** for different UMPA windows, on the right in **b)** for different PBI regularization parameters. The parameters used for the images in Fig. 5.2.5 are indicated. Both phase-retrieval methods show similar edge sharpness. In **c)** and **d)** the resolution of Fig. 5.2.5 is evaluated using FRC. The dark gray line shows the full-bit resolution criterion, the light gray the half-bit criterion. The intersection of the FRC is indicated by the vertical lines. The FRC is yielding similar results for both phase-retrieval methods. Figures **a)** and **b)** modified from [Rie+23].

to the limits of the setup. Additionally, with 4001 angular projections, the scan is undersampled for a detector with a width of 7920 px. To utilize the full resolution for the full FOV, around 12500 angular projections would be necessary, which would increase the scan time drastically to a not practical level. Taking both into account, the results for PBI are not expected to change drastically.

5.2.3 High Energy Scans of Sandstone

In addition to the experiments at the beamline P05, the setup was transferred to the HEMS beamline P07. The basic principle of the setup is similar, with some adaptions to the components. The following section will first describe these modifications and afterwards, present an exemplary application of high-energy DPC.

Adaptions to the Setup

For high beam energies, adapted gratings with increased etching depths were necessary. Due to manufacturing reasons, where high aspect ratios of the gratings were complicated, the shortest period was limited to 10 µm.
The increase in energy and period results in an increase in the Talbot distance of the grating. For a 10 µm period at a beam energy of 60 keV, the fractional Talbot distance is at $1/6\, d_T = 1613$ mm. This exceeds the limitations of the setup. Additionally, this would require a large coherence of the beam. As a result, the TAI cannot be placed at an optimal distance from the detector, which deteriorates the visibility.
As an alternative to using TAIs, other wavefront markers can be considered. Wang et al. [Wan+19] suggested using absorptive structures, such as steel wool. With this, they were able to obtain a visibility of up to 0.14. As the beamline P07 is equipped with a 4 m in-vacuum undulator, the flux on the sample is significantly higher than at P05 (c.f. Sec. 4.1.2). This imposes strict requirements for the dose resistance of the samples, as even moist sand samples showed movement as a result of water reacting in the beam. During experiments, it was also noticed that some plastics react in the beam as well. This was observed for plastic straws and Viton sleeves.
In certain cases, it is possible to compensate for sample movements before phase-retrieval. This can be done easily if the sample itself is rigid and only displays lateral drifts. As the TAI is stepped in between multiple tomographic scans, the phase-steps at each projection angle are recorded with different sample positions. In a first approach, the drift of the sample can be determined and the images can be shifted back to the position of the first phase step. In detail, the correction used in this work uses a single-shot UMPA phase-retrieval with a large window size of $w = 41$ px of a central section for each phase-step. The images are then cross-correlated to the first phase-step to determine the shift in x- and y-direction and rolled back. While this ignores tilts or rotations of the sample, it successfully improved the image quality of the scan shown in the following section.

Scan Parameters						
Sample	Photon Energy	Angular Steps	Exposure Time	Propagation Distance	Grating Period	Phase Steps
Sandstone	57 keV	3501	200 ms	900 mm	10 µm	16

Table 5.2.4: Scan parameters of the sandstone sample with brine and n-decane. The scan was recorded at the beamline P07.

Scan of Sandstone

In order to illustrate the applications of phase-contrast scans at higher beam energies, a scan of a sandstone sample with two liquids is shown. The aim of this measurement was to differentiate the liquids in the reconstructed data. Up to now, the methods used to achieve this include adding stains to one of the liquids. This is unwanted, as staining agents can change the chemical and physical behavior of a liquid, and therefore possibly falsify the results of a measurement. Due to the high dynamic range, as well as the strong absorption of the stone, common phase-retrieval assumptions, homogeneous or weakly absorbing samples, fail as well, leaving the need for a quantitative imaging method.

Sample Preparation The sample was prepared by Shell Global Solutions International BV, Grasweg 31, 1031 HW Amsterdam, The Netherlands. It contained a porous sandstone, with the pores containing brine and n-decane. The sample was enclosed in a Viton sleeve and stored in n-decane for transport. As the Viton sleeve moved in the X-ray beam, the sandstone was cut from the sleeve and transferred to a small n-decane-filled centrifuge tube.

Scanning and Phase-Retrieval For the scan, a beam energy of 57 keV was chosen. The detailed parameters are listed in Tab. 5.2.4. The mean TAI visibility in the reference images was 0.085 using the standard deviation definition and at 0.233 using the min-max definition of visibility (c.f. Eq. 3.1.5 and Eq. 3.1.4).
Prior to phase-retrieval, the previously described drift compensation was applied, as some water contents formed gas bubbles and moved the stone. This improved the image quality significantly, which was especially observable at the edges of the stone grains.
An UMPA window size of 3 px was used for phase-retrieval and the scan was reconstructed with a Shepp-Logan filter.

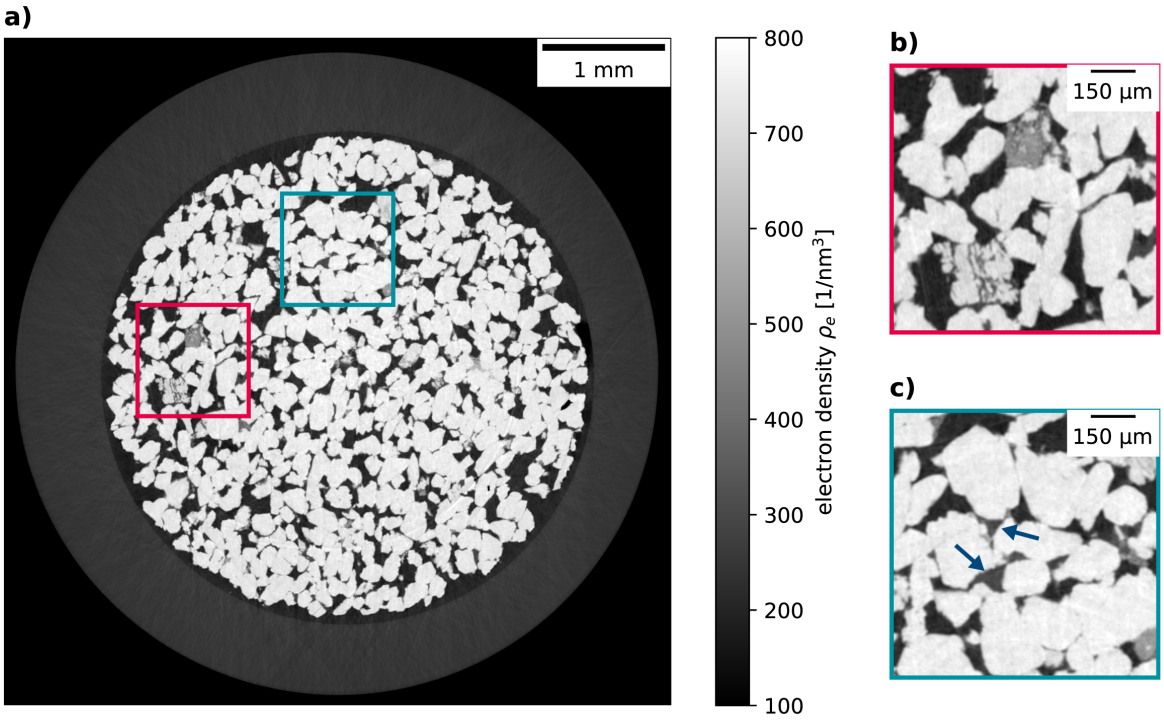

Figure 5.2.7: Scan of a sandstone sample with brine and n-decane in its pores. The scan was recorded at a photon energy of 57 keV at the beamline P07. More details about the scan parameters can be found in Tab. 5.2.4. The sample shows a high dynamic range, with the sandstone at around $\rho_e \approx 750\,1/\mathrm{nm}^3$. In **b)** and **c)** zoom-ins, indicated by the colored squares, are shown. Pores filled with brine are indicated by arrows. The zoom-in in **c)** is further analyzed in Fig. 5.2.8.

Scan Analysis A reconstructed slice of the sample can be seen in Fig. 5.2.7. The sandstone displays a high electron density of around $\rho_e \approx 750\,1/\mathrm{nm}^3$. In Fig. 5.2.7 **b)** and **c)** more details can be seen, while small arrows in **c)** mark pores filled with a different material than the rest.

As the sample liquid composition is known, the expected electron density values can be determined. Neglecting the salt content in the brine, it can be treated as water with an expected electron density of $\rho_{e,w} = 334.7\,1/\mathrm{nm}^3$. The n-decane can be calculated at $\rho_{e,d} = 253.5\,1/\mathrm{nm}^3$. With this difference, the indicated pores in **c)** can be identified as filled with brine.

Further analysis of the image in **c)** is carried out in Fig. 5.2.8. In **a)** the section is shown in a more narrow window and colored, to highlight the differences in the liquids. The brine-filled pores appear in a green/yellow tone, compared to the blue of the n-decane. The sandstone is outside the boundaries of the window.

In Fig. 5.2.8 **b)**, the histogram of **a)** is calculated, using a bin width of $\rho_e = 0.5\,1/\mathrm{nm}^3$. For better comparability, the colormap of **a)** was applied. Assuming the pores can only be filled with n-decane or brine, the histogram was fitted using the sum of two Gaussian peaks. The resulting fit is plotted as a blue curve. With this, the measured electron density of both materials can be determined from the position of the peaks. For n-decane, the value was determined at $\rho_e = (226.9 \pm 0.1)\,1/\mathrm{nm}^3$. The uncertainty was determined from the covariance matrix of the fit. The peak of the brine was much broader, at $\rho_e = (311.0 \pm 1.9)\,1/\mathrm{nm}^3$ with higher uncertainty.

Discussion By using a quantitative phase-contrast imaging method, it was possible to visualize samples with a high dynamic range reliably, even at high photon energies. It was possible to distinguish both liquid phases inside the sandstone.

The histogram analysis can only give a rough estimate of the materials, as mixtures of both liquids are neglected. In addition, the edges of each sandstone particle are blurred, as an effect of the limited spatial resolution. When a pore is filled with n-decane, the blurred edge between sandstone and n-decane will show values similar to brine, independent of whether there is actually a brine layer or not. This affects the fitted peak of the brine, broadening it.

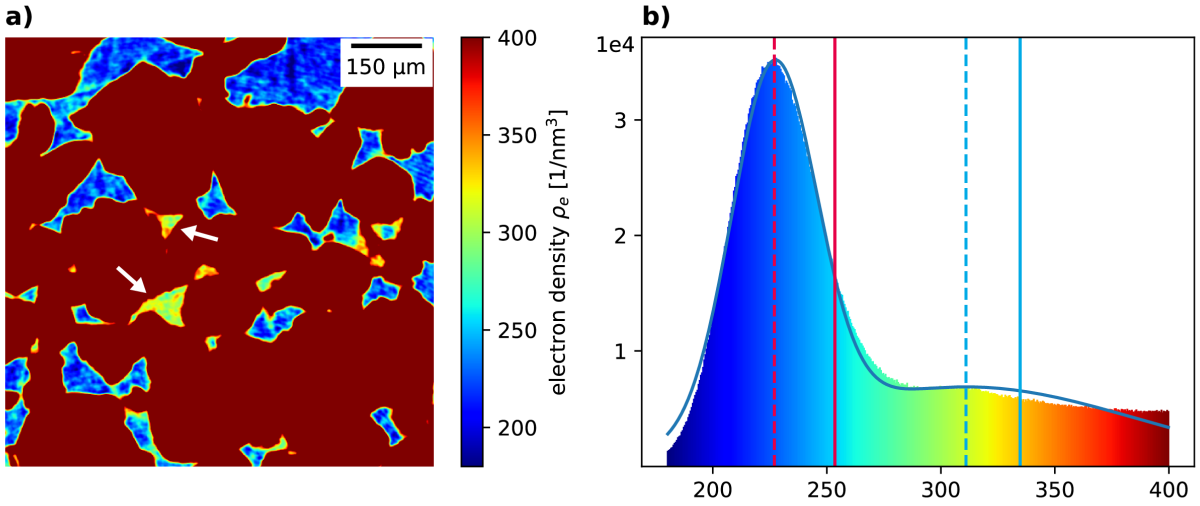

Figure 5.2.8: Analysis of the materials in the sandstone sample. In **a)** the zoom-in of Fig. 5.2.7 **c)** is shown in a different window and colored to highlight the fluids. Assuming the pores can only be filled with n-decane or brine (or mixtures), the histogram of a small volume around the image in **b)** is analyzed. The calculated values of n-decane at $\rho_{e,d} = 253.5\,1/\text{nm}^3$ and water at $\rho_{e,w} = 334.7\,1/\text{nm}^3$ are shown as solid vertical lines. The histogram is fitted using the sum of two Gaussian peaks and the expected value of both peaks are shown as dashed lines at $\rho_e = (226.9 \pm 0.1)\,1/\text{nm}^3$ and $\rho_e = (311.0 \pm 1.9)\,1/\text{nm}^3$. If the systematic underestimation of the electron density is taken into account, both materials can be identified.

5.2.4 Mouse Lymph Nodes

Most third-generation synchrotron sources are so-called user facilities. In the case of PETRA III, DESY, this means that around 80 % of the available beamtime is provided to external users. Research groups can apply with their project for beamtime. The beamline operators, in the case of the beamlines P05 and P07 the Helmholtz-Zentrum Hereon, provide support for the experiments. The offered measurement methods, therefore, have to be running stable and with a high degree of automation to minimize the need for manual interference.
In this last presented application of the setup, a series of scans of mouse lymph nodes was carried out. This project was a collaboration with INI-Research, Group for Interdisciplinary Neurobiology and Immunology from the University of Hamburg. They were the first external users to apply the setup to their samples, so this marks the transition of the setup into user operation.
The aim of the project was to visualize the vascular system in and around the lymph nodes. Parts of the results of this section have been presented at the SPIE Optics and Photonics 2022 in San Diego, and published in Riedel et al. [Rie+22].

Sample Preparation The samples were prepared by the group of INI-Reserach. Animal housing of the C57BL/6 mice and dissection of organs was done at the neurophysiology section of the biological department, University of Hamburg and in accordance with European Union's and local welfare guidelines (Behörde für Gesundheit und Verbraucherschutz, Hamburg, Germany; GZ G21305/591-00.33).
The inguinal lymph nodes were taken out with a block of tissue around them, to ensure all vascular structure inside was undamaged. The samples were fixated in 4 % paraformaldehyde in PBS for one hour before dehydration in 70 % ethanol and a subsequent series in 2-propanol.
As the measurements were split across multiple beamtimes, different embedding methods could be used, as a reaction to problems encountered in the first measurements. For scanning, the first samples were transferred into liquid 70 % ethanol. As the results using this embedding method were unstable (see the section on scanning), the preparation method was changed for the second series of measurements, where a rigid embedding was used. Four samples were embedded under vacuum in Hard Plus 812 resin (EMS Diasum, Cat. Nr. 14115).
During the time of sample preparation, the exact measurement method was not decided yet. In order to enhance the contrast, especially for absorption scans, some of the samples

Scan Parameters						
Sample	Photon Energy	Angular Steps	Exposure Time	Propagation Distance	Grating Period	Phase Steps
Liquid, stained	33 keV	3001	180 ms	300 mm	10 µm	16
Hard resin, unstained	20 keV	3001	120 ms	200 mm	10 µm	16
Hard resin, stained	20 keV	1501	120 ms	200 mm	10 µm	16
Hard resin, stained, 10x	20 keV	4500	400 ms	200 mm	7 µm	16

Table 5.2.5: Scan parameters of mouse lymph nodes.

were stained, using a hematein-lead complex [Mül+18]. The embedding in hard resin was preferred over other possibilities, such as paraffin, as the stain can increase the absorption to a level, where paraffin is not stable anymore.

Scanning and Data Processing The parameters for the scans are listed in Tab. 5.2.5. In addition to the first three scans, which used the standard five-fold magnification and at an effective pixel size of 0.92 µm, a fourth scan was measured, with ten-fold magnification and an effective pixel size of 0.46 µm. This was done, to test whether an increased spatial resolution was necessary to visualize the features. The sample was mounted 3000 px off-axis and stitched after phase-retrieval.
UMPA phase retrieval used a 3 pix window. To ensure comparability between the hard resin embedded samples at five-fold magnification, the unstained sample was reconstructed using only every second angular step, to match the stained sample.

Scan Analysis In Fig. 5.2.9 a reconstructed slice of the stained lymph node in liquid ethanol is shown. In **a)** the different features of the sample can be seen. The lymph node itself is marked as **A** and shows a significantly higher electron density than the surrounding. Inside the node, the brighter areas at the edges can be identified as the follicles, marked as **B**. The surrounding tissue is mainly consisting of adipocytes **C**, which are filled with lipids. Subplot **b)** is showing details inside the node and follicles. Small vessels appear as dark spots, with a few microns in diameter. In **c)** a larger blood vessel in the surrounding tissue can be seen. The image was sharpened using an unsharp masking filter for visual

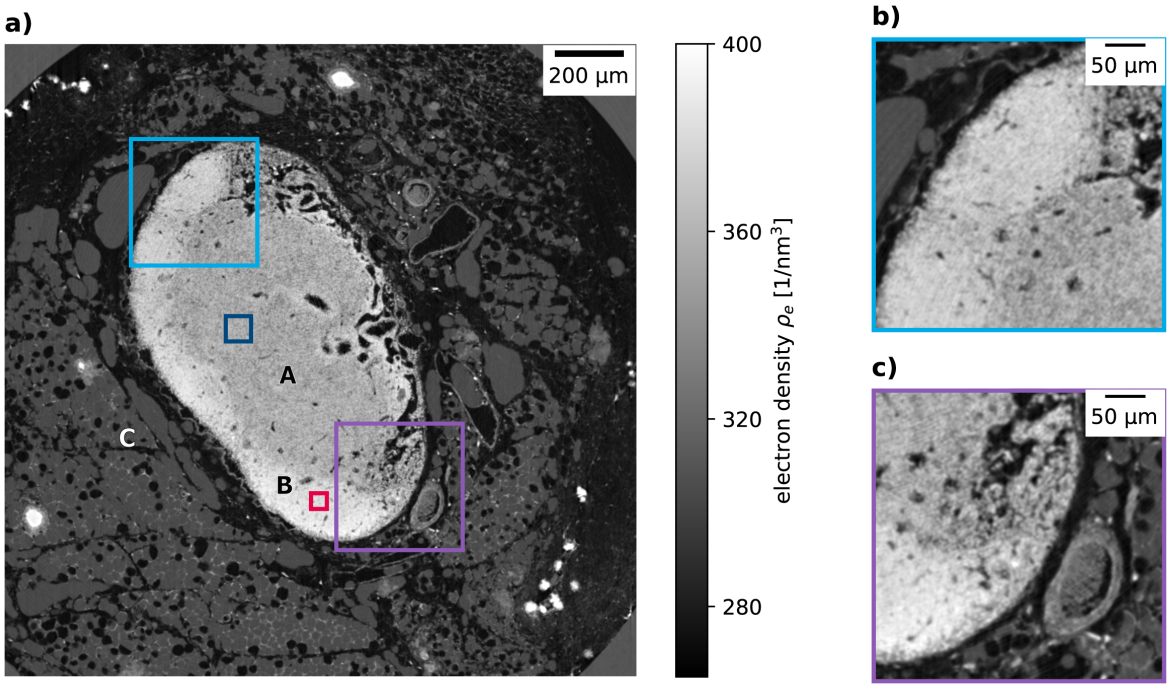

Figure 5.2.9: Scan of a stained lymph node in liquid ethanol. The image has been sharpened for an improved visual impression using an unsharp masking filter. In **a)** the full node is shown, zoom-ins in **b)** and **c)**. The lymph node is marked as **A**, and the follicles as **B**. The surrounding tissue, mainly consisting of filled adipocytes, is marked as **C**. The fine vessels inside the node, exemplary marked in zoom-in **b** by arrows, show strong contrast. The red and blue colored squares mark the areas used for determining the CNR, in blue the lymph node, and in red the follicles. The background area for the CNR is not shown. Figure modified from [Rie+22].

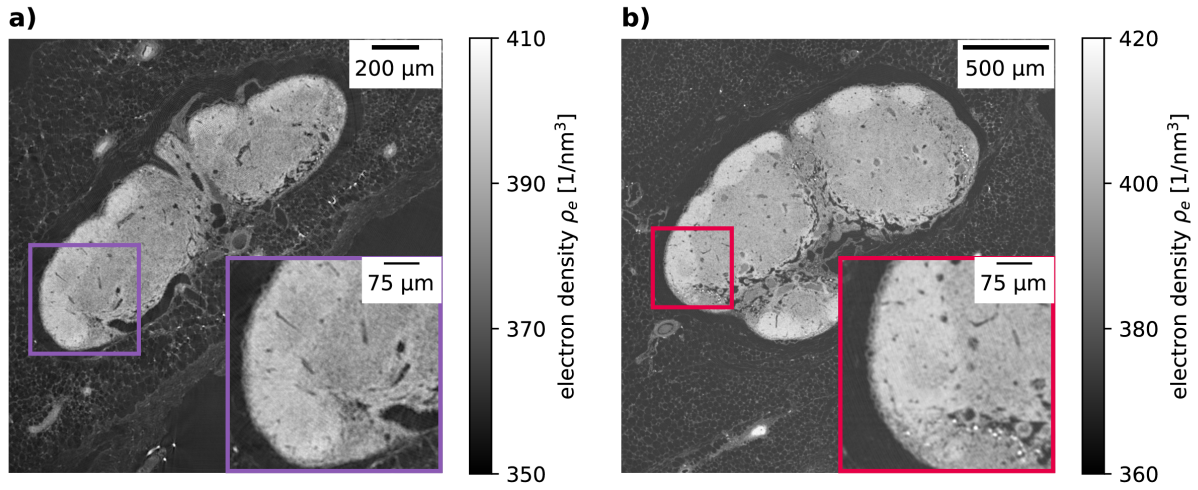

Figure 5.2.10: Comparison of the level of detail between two stained lymph nodes. The scan on the left in **a)** was recorded using a ten-fold magnification with an effective pixel size of 0.46 µm. On the right in **b)** a five-fold magnification objective was used, with an effective pixel size of 0.92 µm. Even when zooming in, the level of detail is similar.

enhancement.

The electron density in the node in liquid was at (356.2 ± 4.8) electrons/nm^3 and in the follicle at (380.2 ± 4.5) electrons/nm^3 (dark blue and red squares). The resolution of the scan was determined, using Fourier ring correlation. The full-bit resolution was at 4.69 µm, the half-bit resolution at 4.17 µm. When comparing the ten-fold magnification scan in Fig. 5.2.10 **a)** to the five-fold magnification in **b)**, no significant difference in the level of details can be seen. Even when zooming in, the structures remain comparable. Consequently, the following scans were using the five-fold magnification.

In Fig. 5.2.11 images of unstained and stained lymph nodes are shown in **a)** and **b)**. The stained sample shows a strong increase in electron density for the lymph node compared to the unstained one. The contrast to the surrounding embedding material is lower in both images, due to the higher electron density of hard resin compared to ethanol. The adipocytes are empty in the hard resin embedded samples due to the preparation process.

Comparing the effects of the stain in detail, the electron density of the unstained node was at (377.2 ± 1.8) electrons/nm^3, of the follicle at (378.5 ± 1.7) electrons/nm^3, whereas the stained node shows (401.6 ± 2.0) electrons/nm^3 in the node and (409.1 ± 1.8) electrons/nm^3 in the follicle. The corresponding CNR values are listed in Tab. 5.2.6. The spatial resolution of the unstained node, determined using FRC, was at 4.68 µm full-bit and 4.14 µm half-bit

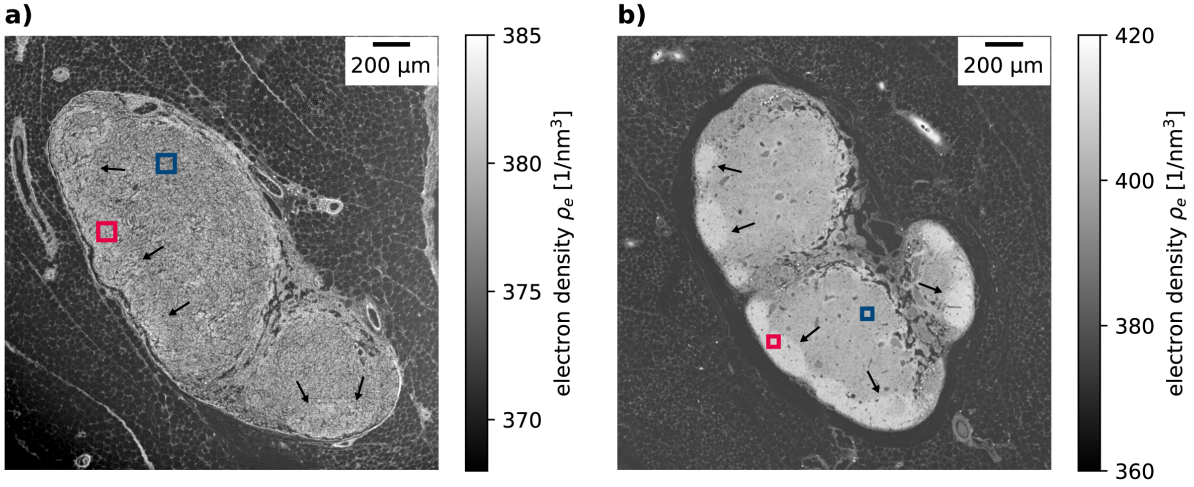

Figure 5.2.11: Comparison of an unstained mouse lymph node in **a)**, and a stained one in **b)**. The locations of the follicles are indicated by the black arrows. Due to the sample preparation, the surrounding fat cells are empty. The electron density of the stained lymph node is lower and closer to the surrounding tissue than of the stained one. The follicles are better visible if stained. The colored squares mark the areas used for determining the CNR, as in Fig. 5.2.9.

resolution. The stained node showed a resolution of 4.70 µm full-bit and 4.13 µm half-bit.

Discussion Liquid sample fixation is a fast and simple preparation method. In the given settings, it was offering the highest CNR (cf. Tab. 5.2.6), of all features. If the sample is stable, the spatial resolution is well below 5 µm. However, as the mechanical stability in the container can be low, this preparation method was prone to sample movements.

In order to prohibit sample movement, hard resin embedding offers an alternative. The preparation is more time-consuming and more elaborate, but the chance of failed scans is much lower.

Higher magnification and spatial resolution of the scans yielded no visual difference in the level of detail in a sample. Several influences might play a role in this. With 2250 angular projections, the high magnification scan is undersampled for a stitched detector width of more than 10 000 px. This was accepted, as the node itself was in the center of the sample, where possible artifacts are not dominant. In addition, the scan time needed for a sufficient sampled scan would be impractical high. Other factors contributing are the stability of the setup and especially the sample. If the sample moves even slightly (a few micrometers) during the scan, the projections get blurred and the advantage over the low magnification

CNR Analysis			
Sample	CNR_{N-BG}	CNR_{F-BG}	CNR_{F-N}
Liquid, stained	87.04	112.35	3.62
Hard resin, unstained	8.66	12.02	0.52
Hard resin, stained Stained	41.42	52.61	2.77

Table 5.2.6: CNR comparison of the hard resin embedded stained and unstained node, as well as for the stained lymph node in liquid ethanol. CNR_{N-BG} denotes the CNR of the node to the embedding material background, CNR_{F-BG} of the follicle to the background, and CNR_{F-N} of the follicle to the node. The scans of the stained and unstained nodes in hard resin were measured at a photon energy of 20 keV, the scan in ethanol at an energy of 33 keV.

is lost.

Analyzing the CNR of the images, the hard resin embedded samples had a lower CNR compared to liquid fixation. For stained samples, all regions can be identified. In contrast, for unstained samples, the follicles are almost not visible with a CNR below one and can only be identified by structural features.

The stain induces a difference in overall electron density between stained and unstained remains at 25 electrons/nm^3 for the node and 31 electrons/nm^3 for the follicles. This shows a tendency of the stain to aggregate in the follicles.

The spatial resolution is at the same level for the hard resin embedding, as for the liquid fixation. Sample details with less than 5 µm can be identified.

Summary and Outlook 6

In this chapter, the main findings of this thesis are summarized shortly. In detail, the setup design, and the applications are considered. In addition, an outlook for future possibilities and developments regarding this setup and method is given.

In this work, the design and application of a quantitative phase-contrast imaging setup at the microtomography beamlines at PETRA III, DESY, was presented. The newly constructed setup on the base of TAIs as wavefront marker and in combination with SBI techniques for phase-retrieval.

6.1 Setup Design

The setup was constructed as an addition to the existing micro CT setups at the beamlines P05 and P07, at PETRA III, DESY. As the wavefront marker, novel designed phase-gratings, so-called Talbot Array Illuminator (TAI) were used. In combination with a 2D piezo stepper motor and continuous rotation scans, fast measurements are realized.
The post-processing chain was newly designed and implemented in a Python virtual environment. To compensate for the large computational requirements of SBI phase-retrieval methods, the processing was designed using multiprocessing and multiple compute nodes of the DESY Maxwell cluster. To account for setup drifts, an extended reference image processing is introduced, which improves the position accuracy of the TAI for phase retrieval and therefore the sensitivity in the phase-retrieved images. For phase-retrieval, the Unified Modulated Pattern Analysis (UMPA) is used. The differential phase images are integrated with Fourier integration approaches and can be reconstructed using Filtered Backprojection (FBP).
The performance of the setup was characterized concerning multiple aspects: An analysis of the gratings found them to produce a high visibility pattern with a small structure size, outperforming the state-of-the-art sandpaper in SBI setups. An investigation of the spatial

resolution showed a value of 4 µm for a standard configuration and the possibility to reach down to 2 µm if the detector is adapted. The angular sensitivity reaches values better than 250 nrad, typical for the class of setups. Studies of a phantom with known material properties showed good quantitative compliance of calculated and measured data with a low systematic underestimation of the phase around 5 %.

6.2 Applications and Measurements

The setup was designed with the goal to go into user operation. The scans measured in this thesis were used to characterize the setup, but also to identify key points relevant for future users. One of the main findings was the importance of dose-resistant samples. The preferred embedding methods were rigid embedding in paraffin wax or hard resin. A liquid fixation in absolute ethanol was also possible.
Scans of stained samples demonstrated the advantage of a quantitative method over single distance PBI with a homogeneous sample assumption. An investigation of samples from COVID-19 fatalities showed a good structural visualization with high contrast, close to the level of histology. A comparison of the TAI setup with PBI phase-retrieval on a human COVID-19 lung sample resulted in a similar level of spatial resolution.
The applications with higher beam energies required adaptions on the wavefront marker but showed successful measurements of higher absorbing materials science samples. Inside porous sandstone, two liquids, brine, and n-decane could be identified and distinguished.
The final transition into user operation was made in collaboration with an external user group. The team of INI-Research applied the setup to scanning mouse lymph nodes. They investigated the vascular structure of the blood system and the entry points into the node.

6.3 Future Setup Applications

By identifying suitable samples and preparation methods, the user operation of the setup will be expanded in the near future. In order to find new use cases and to make the setup known among existing users, currently a block allocation group (BAG) proposal is running. In this, multiple user groups apply and test the setup on different classes of their samples. During the BAG beamtime in November 2022, the list of scanned sample classes was

increased. The samples included mouse embryos, where different development stages of regular and knock-out mice were visualized with high resolution. These samples were a project from the Deutsches Zentrum für Neurodegenerative Erkrankungen (DZNE). Other mouse samples from the TUM focused on investigating X-ray stains. A group of the University of Hannover scanned soil samples, where the aim was to visualize the organic components like root structures, in the soil. This project was also continued at the beamline P07 at higher energies. Also in this beamtime, a group of the University of Kassel scanned critical-point-dried and ethanol fixated insects, including Onychophra, also known as velvet worms. As these samples where several centimeter long, the volumes of up to six height-steps were stitched. The samples profited from the quantitative nature of the scans, as the insects show high density variations between the shell and the inner organs.

6.4 Future Setup Development

The hardware setup offers further possibilities of optimization. The speed of a measurement can be increased, with changing the acquisition scheme. With a fast wavefront-marker stepper, interlaced phase-retrieval schemes might become possible. Other factors, such as the dose dependent behavior of the setup should be explored further. As fast beam shutters are expected to go into operation soon, especially the low dose limits of SBI will become of interest for sensitive samples.

For samples larger than the FOV, currently only off-axis scans and stitching height-steps are available options. For even larger samples, other scan protocols have to be developed. As this will include measurements, where no background is available for the current wavefront marker drift correction, the stability of the setup will become even more important. Other drift correction methods, which do not require an empty background area can be useful. In order to increase the measurement speed, sample stepping acquisition schemes and helical scans should be investigated.

From a phase-retrieval perspective, an addition of directional dark-field has already been demonstrated [Smi+22]. It allows to extract anisotropies in the scattering signal and to gather information about the orientation of sub resolution sized structures. One of the largest challenge remains the absorption signal. Current models for explicit speckle tracking fail to include second order phase effects. At high coherent sources, they are visible and existing explicit SBI phase-retrieval approaches attribute them in the transmission channels. An

alternative to SBI phase-retrieval might be iterative methods, with more elaborate foreword models such as Fresnel propagation [Sto+13] or complete new approaches e.g. based on the X-ray Fokker-Planck equation [PM19]. With further increase of computation power, completely different approaches can also become available. First suggestions to use neural networks have been published [Qia+22]. While all these approaches lack the direct inversion of their model, they might be able to improve the absorption signal, enabling multimodal quantitative imaging.

Appendix

Using the Phase-Retrieval on the DESY Maxwell Cluster

The processing scripts used during this work are available as virtual Mamba environment on the DESY Maxwell cluster. The environment is located at:

`/asap3/petra3/gpfs/common/p05/micro_phase/phase/`.

To activate it, mamba has to be loaded and initialized:

```
module load maxwell mamba gcc/8.2
. mamba-init
mamba activate /asap3/petra3/gpfs/common/p05/micro_phase/phase/
```

Listing 1: Activating the mamba environment

The configuration of the processing and the submission via SLURM to the maxwell cluster is implemented as a Jupyter Notebook. A copy of it can be retrieved from `/asap3/petra3/gpfs/common/p05/micro_phase/phase/Scripts/ConfigPhaseRetrieval.ipynb`. The notebook includes explanations of what to fill in the cells, as well as previews of the selected areas. The settings are stored in a file using pickle given a timestamp when they were created.
For submitting to SLURM, a host and username have to be picked. After logging into the SLURM host, and including the timestamp to the batch script, the phase-retrieval can be submitted.
In the following pages, a preview of the Jupyter Notebook is shown.

Settings for the UMPA phase-retrieval scripts

Adapt the settings for your scan and use the last part to submit to the Maxwell cluster

In [1]:
```
#imports for this settings script, for preview and slice objects
import numpy as np
import matplotlib.pyplot as plt
import sys
sys.path.append('/asap3/petra3/gpfs/common/p05/micro_phase/phase/Scripts/lib/')
from FlyFunctions import *
```

Start with path and name definitions:

Basis **path** for the whole beamtime

In [2]:
```
beamtime_path = '/asap3/petra3/gpfs/p05/2022/data/11015594/' #BAG
```

Now, a **list of scan names** to be processed with the same settings. This can also be just one list element.

In [3]:
```
tomo_name_list=['043_tum_588_3_grating/']
```

It can sometimes happen, that one of the nexus files is broken. You can see this either, that the file size is too small, or that the log files (if you try to process the scan) contain an error message.

In this case, the file can be faked, using a diderent one. Give a **list of tupels** which file should be faked with which one. E.g. file 12 is broken and replaced by 13: [(12,13)]

In [4]:
```
nexus_defects = None #e.g. [(3,4), (7,8), (16,17)]
```

Select a **ROI** for the scan images. Try to avoid areas with no intensity

In [5]:
```
clipper = np.s_[:,:]
```

Let's do a quick preview of the ROI\ The function loads every 10th reference,and loads every step-th image. The images are corrected by an averaged reference.\ The preview uses the minimum of all loaded images, assuming the transmission is stable in the background.

In [6]:
```
prev = load_preview(beamtime_path, tomo_name_list[0], step=100, phasestep=0)
```

In [7]:
```
plt.imshow(prev.min(0)[clipper], vmin=0.3, vmax=1)
```

Out[7]:
```
<matplotlib.image.AxesImage at 0x2ac5af2d0a90>
```

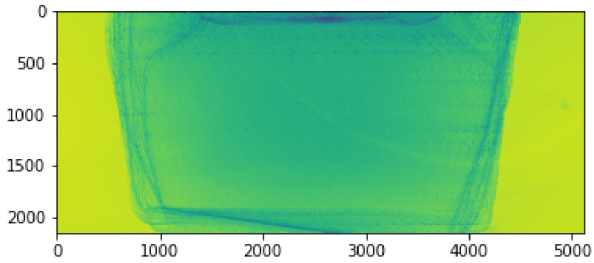

Now the settings for UMPA phase-retrieval:

There is an option to enable automatic segmentation of the sample background (intensity based). This can work well for homogeneous backgrounds and absorbing samples. If it works, the processing is a bit slower, but the results are better (less gradients). To see if it works, you unfortunately have to look at the retrieved projections.

If set to True, the next parameter 'area' is ignored

In [8]:
```
masking=True
```

If no masking can be used, provide empty areas of **all** projections. \ This can be left and right, or just left (for off-axis scans).\ Provide a **slice object**, for the last two axis. \ E.g. area=np.s_[..., 100:-100, np.concatenate([np.arange(10,200), np.arange(4800,5000)])]\ Avoid to include areas with no intensity.

Notes: the Ximea Camera has a width of 7920 px, the KIT of 5120. However, UMPA is clipping the images, and the area is used more than once in the processing. So make sure, a savety distance of 8px + 2*width is maintained (the last value must be smaller than camera minus safety)

In [9]:
```
area=np.s_[..., 100:-100, np.concatenate([np.arange(10,200), np.arange(4800,5000)])]
```

Preview of the selected area\ Keep in mind, the area has to be empty in **all** projections\ If you are not certian, looking at the scan in ImageJ/Fiji is a good help

In [10]:
```
prev_area = prev.min(0)[clipper]
prev_area[area]=0

plt.imshow(prev_area[clipper], vmin=0, vmax=1.1, cmap='jet')
```

Out[10]:
```
<matplotlib.image.AxesImage at 0x2ac5af38dc50>
```

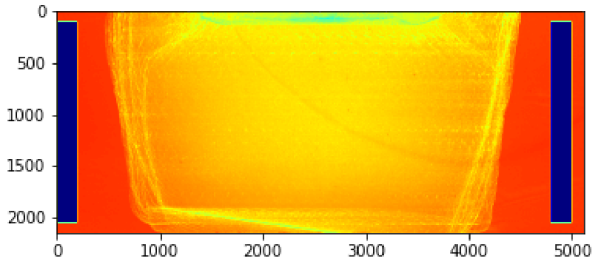

There is an option to do an off-axis scan and stitch the projections. Determine the pixel shift parameter using the separate script. Give an integer.

In [11]:
```
stitch = False
stitch_shift = 314
```

Now the window size of the UMPA processing, **list** of parameters. Multiple possible, if not clear which is suited If everything worked typicall parameters are 0, 1 or 2. For a window size of 0, the darkfield is turned off.

In [12]:
```
width=[1,2]
```

Bool to use the UMPA darkfield model

In [13]:
```
df_mode=True
```

Settings for the phase integration:

Bool to do the phase-integration. For historic reasons mainly.

In [14]:
```
integrate = True
```

Again we need empty **slices**. As they can be different due to stitching, give them for the left and the right side independently. Used for ramp and bg correction of integrated phase

In [15]:
```
area_left = np.s_[...,100:-100,10:200]
area_right = np.s_[...,100:-100,-200:-10]
```

Again a short preview\ Keep in mind, the area has to be empty in **all** projections

In [16]:
```
prev_integ = prev.min(0)[clipper]
prev_integ[area_left] = 0
prev_integ[area_right] = 0

plt.imshow(prev_integ, vmin=0, vmax=1.1, cmap='jet')
```

Out[16]:
```
<matplotlib.image.AxesImage at 0x2ac5afe82da0>
```

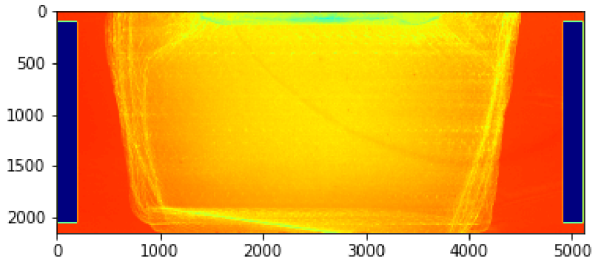

There is a rather experimental option to perform a Richardson Lucy Deconvolution. Look at it, before you enable it.

In [17]:
```
deconvolve=False
deco_sigma=2.2
deco_iter=12
```

Now some more experimental stuff:

Usually this has not to be modified.\ If a rigid sample shows a drift, one can try to shift the projections back, using a single shot phase retrieval of a smaller area.

In [18]:
```
driftcor=False
cor_area = np.s_[...,100:-100, 2000:3000]
```

The number of Components to use for PCA was usually always fixed to 15. One can also try fewer or more, use a scree plot to determine this.\ Don't do ROI scans with this script! This option is depricated and partially removed.\ Turm intermediate on, if you want to write to scratch.\ In rare cases, use mean flat images, rather than the PCA and Eigenflats.

In [19]:
```
ncomp = 15
ROIscan = False
intermediate=False
use_EFs = True
```

If your nexus files contain wrong values, you can overwrite them here, using alternative parameters

In [20]:
```
use_alt_para = False
alt_para = {'alt_energy':36860, 'alt_dist':0.4, 'alt_eps':908E-9}
```

Recomended: saving intermediate images as tif files.\ Also, if you want to skip certain phase-steps, e.g. because of a beam dump, give a slice for the nexus list.\ For P07: assume a certain broken percentage of the detector for a dead pixel correction

In [21]:
```
saveas='tif'
skip_nexus = np.s_[:]
dead_pix_thl = 0
```

Submitting this as SLURM JOB:

Wrap everythin together in a dictionary and save it using pickle

In [22]:
```
import pickle
import time
settings = {
    'beamtime_path':beamtime_path, 'tomo_name_list':tomo_name_list,
    'nexus_defects':nexus_defects, 'clipper':clipper, 'area':area,
    'stitch':stitch, 'stitch_shift':stitch_shift, 'width':width,
    'df_mode':df_mode,'bias_cor':True, 'shift_mode':True,
    'integrate':integrate, 'quick_integration':False,
    'area_left':area_left, 'area_right':area_right, 'driftcor':driftcor,
    'cor_area':cor_area, 'step':1, 'fthl':1E6, 'ncomp':ncomp,
    'ROIscan':ROIscan, 'masking':masking, 'intermediate':intermediate,
    'use_EFs':use_EFs, 'use_alt_para':use_alt_para, 'alt_para':alt_para,
    'deconvolve':deconvolve, 'deco_sigma':deco_sigma,
    'deco_iter':deco_iter, 'dead_pix_thl':dead_pix_thl, 'saveas':saveas,
    'skip_nexus':skip_nexus}


timestamp = int(time.time())

savepath = '/asap3/petra3/gpfs/common/p05/micro_phase/phase/Scripts/Submissions/'
with open(savepath+'%i.p'%timestamp, 'wb') as fp:
    pickle.dump(settings, fp, protocol=pickle.HIGHEST_PROTOCOL)
```

Modify the SLURM host and your username

Hosts can be: max-display001-006, max-nova001-002, max-hzgg001-002, ...

In [23]:
```
%load_ext ipyslurm
%slogin max-hzgg002 --username riedelmi
```

Out[23]:
```
Logging in to riedelmi@max-hzgg002
Logged in to max-hzgg002
```

Submit the batch job to SLURM \ Standard partitions are allcpu and hzg. You might be able to add ps or psx.\ In rare cases for a large number of phase-steps it might be necessary to increase the memory per node to 500 GB

In [24]:
```
print(timestamp)
```

```
1675421040
```

Enter the timestamp manually!

In [25]:
```
%%sbatch
#!/bin/bash
#SBATCH --time    0-05:00:00
#SBATCH --nodes            1
#SBATCH --partition allcpu,hzg
#SBATCH --mem 250GB
#SBATCH --array 1-80
#SBATCH --job-name DPCTomo
```

```
source /etc/profile.d/modules.sh
echo "SLURM_JOB_ID           $SLURM_JOB_ID"
echo "SLURM_ARRAY_TASK_ID    $SLURM_ARRAY_TASK_ID"

module load maxwell mamba gcc/8.2
. mamba-init

mamba activate /asap3/petra3/gpfs/common/p05/micro_phase/phase/

python /asap3/petra3/gpfs/common/p05/micro_phase/phase/Scripts/scripts/PhaseRetrieva

exit
```

```
Submitted batch job 370521
```

You have done it!

The job is now running. The time to complete it will depend on the workload in the cluster.

You can use squeue to look at your running jobs.\ However, your scan can already be finished even tough some workers are still running

In [26]:
```
%%sbash
squeue -u $USER
```

```
             JOBID PARTITION     NAME     USER ST       TIME  NODES NODELIST(REASON)
         370519_1    allcpu  DPCTomo riedelmi  R       0:01      1 max-wn018
         370519_2    allcpu  DPCTomo riedelmi  R       0:01      1 max-wn084
           279171       hzg interact riedelmi  R 3-22:47:19      1 max-hzgg006
     370521_[1-80] hzg,allcp  DPCTomo riedelmi PD       0:00      1 (None)
```

Check if the phase integration of the last scan in the list is finished.

In [27]:
```
print(check_processing_finished(beamtime_path, tomo_name_list, intermediate, width))
```

```
True
```

If the processing is finished, use the reonstruction script to do the tomographic reco

---

Use the script /asap3/petra3/gpfs/common/p05/micro_phase/phase/Scripts/XAid_reco_DPC.py

The reco uses X-Aid, licenses are available on the hzgg002 and hzgg006.

Load the virtual environment with:

module load maxwell mamba gcc/8.2\ . mamba-init\ mamba activate /asap3/petra3/gpfs/common/p05/micro_phase/phase/

Start ipython with pyQt5

ipython --pylab=qt5

modify the script and run it

X-Aid Reconstruction on the Cluster

For the tomographic reconstruction, a script for X-Aid, Mitos, is existing at `/asap3/petra3/gpfs/common/p05/micro_phase/phase/Scripts/XAid_reco_dpc.py`.

X-Aid is installed with one license each on two nodes: max-hzgg002 and max-hzgg006.

As before, the beamtime_path and scan names have to be defined:

```
beamtime_path = '/asap3/petra3/gpfs/p07/2022/data/11015570/'
tomo_name, nexus_defects, cs, stitched ='01_naive_m1/', None, 0, False  #
```

Listing 2: Defining the scan name for the reconstruction

For convenience reasons, the fixed parameters of a scan are put together inn a line:

- tomo_name : string, name of the scan as used in the config file
- nexus_defects : list of tupels, for broken nexus logs, as used in the config file
- cs : float, rotation axis offset, if not determined yet, set to 0
- stitched : bool, indicates an off-axis scan

Further reconstruction parameters can be selected:

- w : int, total size of the UMPA window, corresponds to 2N+1 from the config settings
- channel : sting, channel for reconstruction, c.f. Sec. 4.3 for available channels
- binning : int, binning of images while loading
- load_clipper : slice_object, ROI for reconstruction

Optional settings for ring-filters, PBI phase-retrieval and conversion of the data are available and described in the script.
For searching the rotation center an interactive search is implemented. The resulting reconstruction is saved as 32-bit float TIFF files. The relevant settings are written as text file.

List of Abbreviations

CT Computed Tomography

CNR Contrast-to-Noise Ratio

DCM Double Crystal Monochromator

DMM Double Mulitlayer Monochromator

DPC Differential Phase-Contrast

FBP Filtered Backprojection

FOV Field of View

FRC Fourier Ring Correlation

FWHM full width at half maximum

GBI Grating-Based Imaging

OTF Optical Transfer Function

PCA Principal Component Analysis

PBI Propagation-Based Imaging

UMPA Unified Modulated Pattern Analysis

ROI Region of Interest

SBI Speckle-Based Imaging

TAI Talbot Array Illuminator

TIE Transport of Intensity Equation

Bibliography

[ABa] Nobel Prize Outreach AB. *The Nobel Prize in Physics 1901*. URL: https://www.nobelprize.org/prizes/physics/1901/summary/ (visited on 11/13/2022) (cit. on p. 5).

[ABb] Nobel Prize Outreach AB. *The Nobel Prize in Physics 1953*. URL: https://www.nobelprize.org/prizes/physics/1953/summary/ (visited on 09/26/2022) (cit. on p. 21).

[ABc] Nobel Prize Outreach AB. *The Nobel Prize in Physiology or Medicine 1979*. URL: https://www.nobelprize.org/prizes/medicine/1979/summary/ (visited on 09/22/2022) (cit. on p. 16).

[AM11] J. Als-Nielsen and D. McMorrow. *Elements of modern X-ray physics*. John Wiley & Sons, 2011. DOI: 10.1002/9781119998365 (cit. on pp. 5, 15).

[And+12] P. C. Andrews et al. "Sulfonato-encapsulated bismuth(iii) oxido-clusters from Bi2O3 in water under mild conditions". In: *Chem. Commun.* 48 (61 2012), pp. 7583–7585. DOI: 10.1039/C2CC33495J (cit. on p. 67).

[Bar+08] M. Barthelmess et al. "Status of the PETRA III Insertion devices". In: (2008) (cit. on p. 36).

[BCS12] A. Bravin, P. Coan, and P. Suortti. "X-ray phase-contrast imaging: from pre-clinical applications towards clinics". In: *Physics in Medicine and Biology* 58.1 (Dec. 2012), R1. DOI: 10.1088/0031-9155/58/1/R1 (cit. on p. 2).

[Bec98] F. Beckmann. "Entwicklung, Aufbau und Anwendung eines Verfahrens der Phasenkontrast-Mikrotomographie mit Röntgen-Synchrotronstrahlung". PhD thesis. Universit¨at Dortmund, 1998 (cit. on p. 21).

[Bér+12a] S. Bérujon et al. "Shearing interferometer spatial resolution for at-wavelength hard X-ray metrology". In: *AIP Conference Proceedings*. AIP, 2012. DOI: 10.1063/1.4742295 (cit. on p. 31).

[Bér+12b] S. Bérujon et al. “Two-Dimensional X-Ray Beam Phase Sensing”. In: *Phys. Rev. Lett.* 108 (15 Apr. 2012), p. 158102. DOI: 10.1103/PhysRevLett.108.158102 (cit. on pp. 2, 21, 24).

[BH65] U. Bonse and M. Hart. “Principles and design of Laue-case X-ray interferometers”. In: *Zeitschrift für Physik* 188.2 (1965), pp. 154–164. DOI: 10.1007/BF01339402 (cit. on p. 21).

[BMW12] P. Bon, S. Monneret, and B. Wattellier. “Noniterative boundary-artifact-free wavefront reconstruction from its derivatives”. In: *Applied Optics* 51.23 (2012). DOI: 10.1364/AO.51.005698 (cit. on p. 47).

[Bro99] A. V. Bronnikov. “Reconstruction formulas in phase-contrast tomography”. In: *Optics Communications* 171.4 (1999), pp. 239–244. DOI: https://doi.org/10.1016/S0030-4018(99)00575-1 (cit. on p. 22).

[Bus+18] M. Busse et al. “Three-dimensional virtual histology enabled through cytoplasm-specific X-ray stain for microscopic and nanoscopic computed tomography”. In: *Proceedings of the National Academy of Sciences* 115.10 (2018), pp. 2293–2298. DOI: 10.1073/pnas.1720862115 (cit. on p. 72).

[Buz11] T. M. Buzug. *Computed Tomography*. Springer Berlin Heidelberg, 2011. DOI: 10.1007/978-3-540-74658-4_16 (cit. on pp. 16, 31).

[BWS12] S. Bérujon, H. Wang, and K. Sawhney. “X-ray multimodal imaging using a random-phase object”. In: *Phys. Rev. A* 86 (6 Dec. 2012), p. 063813. DOI: 10.1103/PhysRevA.86.063813 (cit. on pp. 2, 21, 24, 25).

[BZ15] S. Bérujon and E. Ziegler. “Near-field speckle-scanning-based x-ray imaging”. In: *Phys. Rev. A* 92 (1 July 2015), p. 013837. DOI: 10.1103/PhysRevA.92.013837 (cit. on p. 26).

[BZ16] S. Bérujon and E. Ziegler. “X-ray Multimodal Tomography Using Speckle-Vector Tracking”. In: *Phys. Rev. Appl.* 5 (4 Apr. 2016), p. 044014. DOI: 10.1103/PhysRevApplied.5.044014 (cit. on p. 26).

[BZ17] S. Bérujon and E. Ziegler. “Near-field speckle-scanning-based x-ray tomography”. In: *Phys. Rev. A* 95 (6 June 2017), p. 063822. DOI: 10.1103/PhysRevA.95.063822 (cit. on p. 26).

[Clo+96] P. Cloetens et al. “Phase objects in synchrotron radiation hard x-ray imaging”. In: *Journal of Physics D: Applied Physics* 29.1 (Jan. 1996), pp. 133–146. DOI: 10.1088/0022-3727/29/1/023 (cit. on p. 21).

[Clo+99] P. Cloetens et al. “Holotomography: Quantitative phase tomography with micrometer resolution using hard synchrotron radiation x rays”. In: *Applied Physics Letters* 75.19 (1999), pp. 2912–2914. DOI: 10.1063/1.125225 (cit. on pp. 2, 22).

[Dav+02] C. David et al. “Differential x-ray phase contrast imaging using a shearing interferometer”. In: *Applied Physics Letters* 81.17 (2002), pp. 3287–3289. DOI: 10.1063/1.1516611 (cit. on pp. 2, 21).

[Dav+95] T. J. Davis et al. “Phase-contrast imaging of weakly absorbing materials using hard X-rays”. In: *Nature* 373.6515 (1995), pp. 595–598. DOI: 10.1038/373595a0 (cit. on pp. 15, 21).

[De +22] F. De Marco et al. *UMPA C++*. Accessed: 31.01.2023, 10:29. 2022. DOI: 10.5281/zenodo.6984740. URL: https://zenodo.org/record/6984740#.Y9jjUHbMIYo (cit. on p. 45).

[DESa] DESY. *How does a synchrotron radiation source work?* URL: https://photon-science.desy.de/research/students__teaching/primers/synchrotron_radiation/index_eng.html (visited on 09/25/2022) (cit. on p. 8).

[DESb] DESY. *PETRA III*. URL: https://photon-science.desy.de/facilities/petra_iii/index_eng.html (visited on 09/10/2022) (cit. on p. 35).

[DESc] DESY. *Storage Rings as Synchrotron Radiation Sources*. URL: https://photon-science.desy.de/research/students__teaching/primers/storage_rings__beamlines/index_eng.html (visited on 09/25/2022) (cit. on p. 8).

[Don07] T. Donath. “Quantitative X-ray microtomography with synchrotron radiation”. PhD thesis. GKSS-Forschungszentrum Geesthacht GmbH (Germany), 2007 (cit. on p. 22).

[Eck+20] M. Eckermann et al. “3D virtual pathohistology of lung tissue from Covid-19 patients based on phase contrast X-ray tomography”. In: *eLife* 9 (Aug. 2020), e60408. DOI: 10.7554/eLife.60408 (cit. on p. 2).

[End18] M. Endrizzi. “X-ray phase-contrast imaging”. In: *Nuclear Instruments and Methods in Physics Research Section A: Accelerators, Spectrometers, Detectors and Associated Equipment* 878 (2018), pp. 88–98. DOI: https://doi.org/10.1016/j.nima.2017.07.036 (cit. on p. 2).

[Fit00] R. Fitzgerald. “Phase-Sensitive X-Ray Imaging”. In: *Physics Today* 53.7 (2000), pp. 23–26. DOI: 10.1063/1.1292471 (cit. on pp. 2, 22).

[Gre+14] I. Greving et al. “P05 imaging beamline at PETRA III: first results”. In: *Developments in X-ray Tomography IX*. Vol. 9212. SPIE. 2014, pp. 166–173. DOI: 10.1117/12.2061768 (cit. on p. 36).

[Gus+21] A. Gustschin et al. “High-resolution and sensitivity bi-directional x-ray phase contrast imaging using 2D Talbot array illuminators”. In: *Optica* 8.12 (Dec. 2021), pp. 1588–1595. DOI: 10.1364/OPTICA.441004 (cit. on pp. 40, 41, 51, 55).

[Hai+10] A. Haibel et al. “Micro-and nano-tomography at the GKSS Imaging Beamline at PETRA III”. In: *Developments in X-Ray Tomography VII*. Vol. 7804. SPIE. 2010, pp. 98–105. DOI: 10.1117/12.860852 (cit. on p. 36).

[Her10] J. Herzen. “A grating interferometer for materials science imaging at a second-generation synchrotron radiation source”. PhD thesis. Staats-und Universitätsbibliothek Hamburg Carl von Ossietzky, 2010 (cit. on p. 22).

[HGD93] B.L. Henke, E.M. Gullikson, and J.C. Davis. “X-Ray Interactions: Photoabsorption, Scattering, Transmission, and Reflection at E = 50-30,000 eV, Z = 1-92”. In: *Atomic Data and Nuclear Data Tables* 54.2 (1993), pp. 181–342. DOI: https://doi.org/10.1006/adnd.1993.1013 (cit. on p. 62).

[Hip18] A. Hipp. “High-resolution grating-based phase-contrast imaging for synchrotron radiation sources”. PhD thesis. Staats-und Universitätsbibliothek Hamburg Carl von Ossietzky, 2018 (cit. on pp. 3, 39, 51).

[HJ80] D. J. Hawkes and D. F. Jackson. “An accurate parametrisation of the X-ray attenuation coefficient”. In: *Physics in Medicine and Biology* 25.6 (Nov. 1980), pp. 1167–1171. DOI: 10.1088/0031-9155/25/6/014 (cit. on p. 12).

[IB95] V. N. Ingal and E. A. Beliaevskaya. “X-ray plane-wave topography observation of the phase contrast from a non-crystalline object”. In: *Journal of Physics D: Applied Physics* 28.11 (1995), pp. 2314–2317. DOI: 10.1088/0022-3727/28/11/012 (cit. on p. 21).

[KN29] O. Klein and Y. Nishina. In: *Zeitschrift für Physik* 52.11 (1929), pp. 853–868. DOI: 10.1007/BF01366453 (cit. on p. 12).

[Kot+07] C. Kottler et al. “A two-directional approach for grating based differential phase contrast imaging using hard x-rays”. In: *Optics express* 15.3 (2007), pp. 1175–1181. DOI: 10.1364/oe.15.001175 (cit. on p. 47).

[KS01] A. C Kak and M. Slaney. *Principles of computerized tomographic imaging*. SIAM, 2001. DOI: 10.1137/1.9780898719277 (cit. on p. 16).

[Lan+14] S. Lang et al. “Experimental comparison of grating- and propagation-based hard X-ray phase tomography of soft tissue”. In: *Journal of Applied Physics* 116.15 (2014), p. 154903. DOI: 10.1063/1.4897225 (cit. on p. 22).

[MB92] G. R. Morrison and M. T. Browne. “Dark-field imaging with the scanning transmission x-ray microscope”. In: *Review of Scientific Instruments* 63.1 (1992), pp. 611–614. DOI: 10.1063/1.1143820 (cit. on p. 24).

[MG78] R. Magnusson and T. K. Gaylord. “Diffraction efficiencies of thin phase gratings with arbitrary grating shape”. In: *J. Opt. Soc. Am.* 68.6 (1978), pp. 806–809. DOI: 10.1364/JOSA.68.000806 (cit. on p. 31).

[Mod+07] P. Modregger et al. “Spatial resolution in Bragg-magnified X-ray images as determined by Fourier analysis”. In: *physica status solidi (a)* 204.8 (2007), pp. 2746–2752. DOI: 10.1002/pssa.200675685 (cit. on p. 33).

[Mom+03] A. Momose et al. “Demonstration of X-Ray Talbot Interferometry”. In: *Japanese Journal of Applied Physics* 42.Part 2, No. 7B (2003), pp. L866–L868. DOI: 10.1143/jjap.42.l866 (cit. on pp. 2, 21).

[Mom05] A. Momose. “Recent Advances in X-ray Phase Imaging”. In: *Japanese Journal of Applied Physics* 44.9R (Sept. 2005), p. 6355. DOI: 10.1143/JJAP.44.6355 (cit. on p. 2).

[Mor+20] A. J. Morgan et al. “Ptychographic X-ray speckle tracking”. In: *Journal of Applied Crystallography* 53.3 (June 2020), pp. 760–780. DOI: 10.1107/S1600576720005567 (cit. on p. 26).

[MPS12] K. S. Morgan, D. M. Paganin, and K. Siu. “X-ray phase imaging with a paper analyzer”. In: *Applied Physics Letters* 100.12 (2012), p. 124102. DOI: 10.1063/1.3694918. eprint: https://doi.org/10.1063/1.3694918 (cit. on pp. 2, 21, 24).

[Mül+18] M. Müller et al. “Nucleus-specific X-ray stain for 3D virtual histology”. In: *Scientific reports* 8.1 (2018), pp. 1–10. DOI: 10.1038/s41598-018-36067-y (cit. on pp. 72, 83).

[Oli21] A. Olivo. "Edge-illumination x-ray phase-contrast imaging". In: *Journal of Physics: Condensed Matter* 33.36 (2021), p. 363002. DOI: 10.1088/1361-648X/ac0e6e (cit. on p. 2).

[OS07] A. Olivo and R. Speller. "A coded-aperture technique allowing x-ray phase contrast imaging with conventional sources". In: *Applied Physics Letters* 91.7 (2007), p. 074106. DOI: 10.1063/1.2772193 (cit. on p. 21).

[Pag+02] D. Paganin et al. "Simultaneous phase and amplitude extraction from a single defocused image of a homogeneous object". In: *Journal of Microscopy* 206.1 (2002), pp. 33–40. DOI: 10.1046/j.1365-2818.2002.01010.x (cit. on pp. 2, 21, 22).

[Pag+06] D. Paganin et al. *Coherent X-ray optics*. 6. Oxford University Press on Demand, 2006. DOI: 10.1093/acprof:oso/9780198567288.001.0001 (cit. on pp. 5, 27).

[Pag+18] D. M. Paganin et al. "Single-image geometric-flow x-ray speckle tracking". In: *Phys. Rev. A* 98 (5 Nov. 2018), p. 053813. DOI: 10.1103/PhysRevA.98.053813 (cit. on p. 25).

[Pav+20a] K. M. Pavlov et al. "Single-Shot X-Ray Speckle-Based Imaging of a Single-Material Object". In: *Physical Review Applied* 13.5 (2020). DOI: 10.1103/physrevapplied.13.054023 (cit. on p. 25).

[Pav+20b] K. M. Pavlov et al. "X-ray multi-modal intrinsic-speckle-tracking". In: *Journal of Optics* 22.12 (2020), pp. 3–6. DOI: 10.1088/2040-8986/abc313 (cit. on p. 25).

[Pfe+06] F. Pfeiffer et al. "Phase retrieval and differential phase-contrast imaging with low-brilliance X-ray sources". In: *Nature Physics* 2.4 (2006), pp. 258–261. DOI: 10.1038/nphys265 (cit. on p. 21).

[Pfe+08] F. Pfeiffer et al. "Hard-X-ray dark-field imaging using a grating interferometer". In: *Nature Materials* 7.2 (2008), pp. 134–137. DOI: 10.1038/nmat2096 (cit. on p. 24).

[Pic+18] J. Pichat et al. "A Survey of Methods for 3D Histology Reconstruction". In: *Medical Image Analysis* 46 (2018), pp. 73–105. DOI: https://doi.org/10.1016/j.media.2018.02.004 (cit. on p. 1).

[PM19] D. M. Paganin and Kaye S. Morgan. "X-ray Fokker–Planck equation for paraxial imaging". In: *Scientific Reports* 9.1 (2019). DOI: 10.1038/s41598-019-52284-5 (cit. on pp. 25, 92).

[Qc23] QuantStack and mamba contributors. *mamba*. Accessed: 13.01.2022, 11:29. 2023. URL: https://github.com/mamba-org/mamba (cit. on p. 49).

[Qia+22] Z. Qiao et al. "Real-time X-ray phase-contrast imaging using SPINNet—a speckle-based phase-contrast imaging neural network". In: *Optica* 9.4 (Apr. 2022), pp. 391–398. DOI: 10.1364/OPTICA.453748 (cit. on p. 92).

[Rad86] J. Radon. "On the determination of functions from their integral values along certain manifolds". In: *IEEE Transactions on Medical Imaging* 5.4 (1986), pp. 170–176. DOI: 10.1109/TMI.1986.4307775 (cit. on p. 16).

[Rie+21] M. Riedel et al. "High-resolution quantitative phase-contrast x-ray imaging for biomedical samples at PETRA III". In: *Developments in X-Ray Tomography XIII*. Vol. 11840. SPIE. 2021, pp. 123–131. DOI: 10.1117/12.2594506 (cit. on pp. 51, 67, 69).

[Rie+22] M. Riedel et al. "Quantitative phase-contrast x-ray micro CT for visualization of mouse lymph nodes". In: *Developments in X-Ray Tomography XIV*. Vol. 12242. SPIE. 2022. DOI: 10.1117/12.2631184 (cit. on pp. 82, 84).

[Rie+23] M. Riedel et al. "Comparing x-ray phase-contrast imaging using a Talbot array illuminator to propagation-based imaging for non-homogeneous biomedical samples". In: *Scientific Reports* 13.1 (2023), p. 6996. DOI: 10.1038/s41598-023-33788-7 (cit. on pp. 67, 70–72, 74, 76).

[RL71] G. N. Ramachandran and A. V. Lakshminarayanan. "Three-dimensional Reconstruction from Radiographs and Electron Micrographs: Application of Convolutions instead of Fourier Transforms". In: *Proceedings of the National Academy of Sciences* 68.9 (1971), pp. 2236–2240. DOI: 10.1073/pnas.68.9.2236 (cit. on p. 18).

[Rön98] W. C. Röntgen. "Ueber eine neue Art von Strahlen". In: *Annalen der Physik* 300.1 (1898), pp. 12–17. DOI: https://doi.org/10.1002/andp.18983000103. eprint: https://onlinelibrary.wiley.com/doi/pdf/10.1002/andp.18983000103 (cit. on p. 5).

[Rui+16] M. Ruiz-Yaniz et al. "Hard X-ray phase-contrast tomography of non-homogeneous specimens: grating interferometry versus propagation-based imaging". In: *J Synchrotron Radiat* 23.Pt 5 (2016), pp. 1202–9. DOI: 10.1107/S1600577516009164 (cit. on p. 22).

[Sal+09] T. Salditt et al. “Projection phase contrast microscopy with a hard x-ray nanofocused beam: Defocus and contrast transfer”. In: *Phys. Rev. B* 79 (18 May 2009), p. 184112. DOI: 10.1103/PhysRevB.79.184112 (cit. on p. 2).

[Sch] N. Schell. *P07 Unified Data Sheet*. URL: https://photon-science.desy.de/facilities/petra_iii/beamlines/p07_high_energy_materials_science/unified_data_sheet_p07/index_eng.html (visited on 09/10/2022) (cit. on p. 38).

[Sch+10] G. Schulz et al. “High-resolution tomographic imaging of a human cerebellum: comparison of absorption and grating-based phase contrast”. In: *Journal of The Royal Society Interface* 7.53 (2010), pp. 1665–1676. DOI: https://doi.org/10.1098/rsif.2010.0281 (cit. on p. 2).

[Smi+22] R. Smith et al. “X-ray directional dark-field imaging using Unified Modulated Pattern Analysis”. In: *PLOS ONE* 17.8 (Aug. 2022), pp. 1–12. DOI: 10.1371/journal.pone.0273315 (cit. on p. 91).

[Sni+95] A. Snigirev et al. “On the possibilities of x-ray phase contrast microimaging by coherent high-energy synchrotron radiation”. In: *Review of Scientific Instruments* 66.12 (1995), pp. 5486–5492. DOI: 10.1063/1.1146073 (cit. on pp. 2, 21).

[Sto+13] M. Stockmar et al. “Near-field ptychography: phase retrieval for inline holography using a structured illumination”. In: *Scientific reports* 3.1 (2013), pp. 1–6. DOI: 10.1038/srep01927 (cit. on p. 92).

[Sul97] T.J. Suleski. “Generation of Lohmann images from binary-phase Talbot array illuminators”. In: *Appl. Opt.* 36.20 (July 1997), pp. 4686–4691. DOI: 10.1364/AO.36.004686 (cit. on p. 40).

[Tal36] H.F. Talbot. “LXXVI. Facts relating to optical science. No. IV”. In: *The London, Edinburgh, and Dublin Philosophical Magazine and Journal of Science* 9.56 (1836), pp. 401–407. DOI: 10.1080/14786443608649032. eprint: https://doi.org/10.1080/14786443608649032 (cit. on p. 23).

[Tea83] M. R. Teague. “Deterministic phase retrieval: a Green’s function solution”. In: *Journal of the Optical Society of America* 73.11 (1983), pp. 1434–1441. DOI: 10.1364/JOSA.73.001434 (cit. on p. 22).

[Ush21] L. Ushakov. “Data Analysis for High-Resolution Quantitative Phase-Contrast Imaging at Highly Brilliant Sources”. MA thesis. Technical University of Munich, 2021 (cit. on p. 65).

[Van+15] V. Van Nieuwenhove et al. “Dynamic intensity normalization using eigen flat fields in X-ray imaging”. In: *Optics Express* 23.21 (2015), pp. 27975–89. DOI: 10.1364/OE.23.027975 (cit. on p. 29).

[Van+82] M. Van Heel et al. “The structure and function of invertebrate respiratory proteins”. In: *EMBO workshop*. 1982, pp. 69–73 (cit. on p. 33).

[VS05] M. Van Heel and M. Schatz. “Fourier shell correlation threshold criteria”. In: *Journal of Structural Biology* 151.3 (2005), pp. 250–262. DOI: https://doi.org/10.1016/j.jsb.2005.05.009 (cit. on p. 33).

[Wan+19] H. Wang et al. “High-energy, high-resolution, fly-scan X-ray phase tomography”. In: *Scientific Reports* 9.1 (2019), pp. 1–11. DOI: 10.1038/s41598-019-45561-w (cit. on p. 77).

[Wei+05a] T. Weitkamp et al. “X-ray phase imaging with a grating interferometer”. In: *Optics Express* 13.16 (2005), p. 6296. DOI: 10.1364/opex.13.006296 (cit. on p. 21).

[Wei+05b] T. Weitkamp et al. “X-ray phase imaging with a grating interferometer”. In: *Optics Express* 13.16 (2005), p. 6296. DOI: 10.1364/opex.13.006296 (cit. on p. 31).

[Wei+10] T. Weitkamp et al. “Parallel-beam imaging at the ESRF beamline ID19: current status and plans for the future”. In: *AIP Conference Proceedings* 1234.1 (June 2010), pp. 83–86. DOI: 10.1063/1.3463345 (cit. on p. 2).

[Whi77] D. R. White. “An analysis of the Z-dependence of photon and electron interactions”. In: *Physics in Medicine and Biology* 22.2 (Mar. 1977), pp. 219–228. DOI: 10.1088/0031-9155/22/2/003 (cit. on p. 12).

[Wil] F. Wilde. *P05 Unified Data Sheet*. URL: https://photon-science.desy.de/facilities/petra_iii/beamlines/p05_imaging_beamline/unified_data_sheet_p05/index_eng.html (visited on 09/10/2022) (cit. on p. 37).

[Wil+16] F. Wilde et al. “Micro-CT at the imaging beamline P05 at PETRA III”. In: *AIP conference Proceedings*. Vol. 1741. 1. AIP Publishing LLC. 2016, p. 030035. DOI: 10.1063/1.4952858 (cit. on p. 36).

[Wil19] P. Willmott. *An introduction to synchrotron radiation: techniques and applications*. John Wiley & Sons, 2019. DOI: 10.1002/9781119970958 (cit. on p. 5).

[YR97] M. J. Yaffe and J. A. Rowlands. "X-ray detectors for digital radiography". In: *Physics in Medicine and Biology* 42.1 (Jan. 1997), pp. 1–39. DOI: 10.1088/0031-9155/42/1/001 (cit. on p. 16).

[Zan+13a] I. Zanette et al. "Holotomography versus X-ray grating interferometry: A comparative study". In: *Applied Physics Letters* 103.24 (2013), p. 244105. DOI: 10.1063/1.4848595 (cit. on pp. 3, 22).

[Zan+13b] I. Zanette et al. "X-ray grating-based phase tomography for 3D histology". In: *RSC Adv.* 3 (43 2013), pp. 19816–19819. DOI: 10.1039/C3RA41372A (cit. on p. 2).

[Zan+14] I. Zanette et al. "Speckle-Based X-Ray Phase-Contrast and Dark-Field Imaging with a Laboratory Source". In: *Phys. Rev. Lett.* 112 (25 June 2014), p. 253903. DOI: 10.1103/PhysRevLett.112.253903 (cit. on p. 27).

[Zdo+17] M. C. Zdora et al. "X-ray Phase-Contrast Imaging and Metrology through Unified Modulated Pattern Analysis". In: *Phys Rev Lett* 118.20 (2017), p. 203903. DOI: 10.1103/PhysRevLett.118.203903 (cit. on p. 26).

[Zdo+20a] M. C. Zdora et al. "X-ray phase tomography with near-field speckles for three-dimensional virtual histology". In: *Optica* 7.9 (2020), p. 1221. DOI: 10.1364/optica.399421 (cit. on pp. 22, 26, 58).

[Zdo+20b] M.-C. Zdora et al. "X-ray phase imaging with the unified modulated pattern analysis of near-field speckles at a laboratory source". In: *Appl. Opt.* 59.8 (Mar. 2020), pp. 2270–2275. DOI: 10.1364/AO.384531 (cit. on p. 58).

[Zdo18] M. C. Zdora. "State of the Art of X-ray Speckle-Based Phase-Contrast and Dark-Field Imaging". In: *Journal of Imaging* 4.5 (2018). DOI: 10.3390/jimaging4050060 (cit. on pp. 25, 26).

List of Figures

List of Tables

Acknowledgments

This thesis was written in the time from January 2020 to March 2023 in the Research Group Biomedical Imaging Physics at the Technical University of Munich and in the Institute of Materials Physics at the Helmholtz-Zentrum Hereon.

First of all, I want to thank my supervisor Julia Herzen for having me in her group both as Master student and PhD student. Thank you for all the discussions and meetings, etc. I learned a lot and had a very good time in your group.

Next, another large thanks to Felix Beckmann, who mentored me at Hereon. Thank you for helping me with the experiments, conferences and administrative stuff.

Another thanks to Christina Krywka and Martin Müller, for supporting me at Hereon and the institute of materials physics.

Thank you Jörg Hammel, for helping countless times during beamtimes, with writing and helping me to keep my sanity during this work.

The whole team of the imaging beamlines, it was great fun to work with you. Fabian Wilde, Julian Moosmann, Imke Greving and Silja Flenner.

Another thank to my office colleagues, Silja Flenner and Sami Wirtensohn. Without them, work would have been much more boring.

Thank you Kirsten Taphorn, for helping with publications and whenever I had questions on university related stuff.

Thank you Madleen Busse, for preparing numerous samples for my beamtimes. Without you, the images in this thesis would be far more boring.

Thanks to all the technical staff of WP, Jens Brehling, Hilmar Burmester and Ursula Tietze.

I want to thank Pierre Thibault and his group, especially Fabio De Marco and Sara Savatović, for providing us with the C++ implementation of the UMPA package and the fruitful discussions about this.

Thanks to the whole chair of E17. Even though I just visited you a few times, I always felt welcome. Unfortunately you missed quite a few cakes, which I brought to the office in Hamburg...

Another thanks goes to the group of INI-Research, with Stephan Henne, Florian Schwarzenberg and Paul Schütz, who were the first brave enough to use the setup as external users. It was great fun to work with you.

Thank you Sami, Felix, Joerg and Silja for proofreading this thesis.

Finally, a large thanks to my family. You know what you mean to me.